

# **Stony Brook University**



OFFICIAL COPY

**The official electronic file of this thesis or dissertation is maintained by the University Libraries on behalf of The Graduate School at Stony Brook University.**

**© All Rights Reserved by Author.**

**The study of nonequilibrium dissipative quantum  
dynamics and applications to energy transport  
and quantum information processes**

A Dissertation presented

by

**Zhedong Zhang**

to

The Graduate School

in Partial Fulfillment of the

Requirements

for the Degree of

**Doctor of Philosophy**

in

**Physics**

Stony Brook University

**August 2016**

**Stony Brook University**

The Graduate School

Zhedong Zhang

We, the dissertation committee for the above candidate for the

Doctor of Philosophy degree, hereby recommend

acceptance of this dissertation

**Jin Wang - Dissertation Advisor**  
**Professor, Department of Chemistry**  
**Department of Physics and Astronomy**

**Thomas Weinacht - Chairperson of Defense**  
**Professor, Department of Physics and Astronomy**

**Christopher Herzog - Committee Member**  
**Associate Professor, Department of Physics and Astronomy**

**Xiaolin Li - Committee Member**  
**Professor, Department of Applied Mathematics and Statistics**

This dissertation is accepted by the Graduate School

Charles Taber  
Dean of the Graduate School

Abstract of the Dissertation

**The study of nonequilibrium dissipative quantum  
dynamics and applications to energy transport  
and quantum information processes**

by

**Zhedong Zhang**

**Doctor of Philosophy**

in

**Physics**

Stony Brook University

**2016**

Nonequilibrium quantum physics is of fundamental importance and interest. It is still an extremely hard issue even in today's theoretical physics because of the lack of the knowledge on the basic theories, like the nonequilibrium quantum statistical mechanics. The recent advances on theory and experiments reveal the essentiality of nonequilibrium quantum dynamics on explaining as well as understanding many interesting phenomenon, i.e., the ultrafast energy transfer & long-survived quantum coherence in organic molecules, quantum phase transition and the novel transport properties of superfluid gas at low temperature. Here we will focus on the nonequilibrium quantum dynamics relaxing towards the steady state breaking the detailed balance, since this still remains elusive especially at far-from-equilibrium regime.

Firstly we establish a theoretical framework in terms of curl quantum flux to uncover and profoundly understand the intrinsic relation between quantum coherence in systems and nonequilibriumness. This provides the microscopic explanation for the enhancement of coherence in molecular junctions at far-from-equilibrium. Secondly we explore the dynamical relaxation process

towards the nonequilibrium steady state and study the important contribution of coherence to the dephasing time scale as well as dynamical energy transport. Moreover we also uncover the mechanism to explain long-lived coherence by effective field theory: the discrete molecular vibrations effectively weaken the exciton-environment interaction, due to the polaron effect. This subsequently demonstrates the role of vibrational coherence which greatly contributes to long-lived feature of the excitonic coherence observed in femtosecond experiments.

As inspired by the quantum information process, we finally study the dynamics of spin arrays coupled to nuclear spin environments via the hyperfine interaction. This uncovers the rapid coherent oscillations of coherence and entanglement under detailed-balance-breaking, which has never been observed before, i.e., Overhauser noise.

*To my parents*

# Table of Contents

<b>1</b>	<b>Introduction</b>	<b>1</b>
<b>2</b>	<b>Curl flux, coherence and population landscape of nonequilibrium quantum dynamics</b>	<b>4</b>
2.1	General framework of nonequilibrium classical dynamics . . .	4
2.2	General framework for nonequilibrium quantum dynamics . .	8
2.3	Energy and charge transport in molecular system . . . . .	11
2.3.1	Hamiltonian and quantum master equation . . . . .	11
2.3.2	Curl decomposition and nonequilibrium quantum flux .	16
2.3.3	Comparison with classical description . . . . .	23
2.3.4	Quantum transport and non-equilibrium thermodynamics . . . . .	25
2.3.5	Conclusion and remarks . . . . .	32
2.4	Curl quantum flux in continuous space and vibrational energy transport . . . . .	33
2.4.1	Model and Hamiltonian . . . . .	33
2.4.2	Quantum Master Equation in coherent space . . . . .	35
2.4.3	Shape and orientation of the curl flux and vibration correlations in non-equilibrium quantum systems . . .	37
2.4.4	Heat transport intermediated by molecular vibrations .	43
2.4.5	Coherence effect on curl flux and heat transport . . . .	48
2.4.6	Conclusion and remarks . . . . .	52
<b>3</b>	<b>Energy transport and coherence dynamics: relaxation process I</b>	<b>54</b>
3.1	Vibration and coherence dynamics in molecules . . . . .	54
3.1.1	Vibrational energy transfer in molecules . . . . .	55
3.1.2	Quantum Master Equation . . . . .	57

3.1.3	Coherence and population dynamics . . . . .	59
3.1.4	Quantification of coherence effect . . . . .	64
3.1.5	Heat current . . . . .	67
3.1.6	Conclusion and remarks . . . . .	68
3.2	Origin of long-lived quantum coherence and excitation dynamics in pigment-protein complexes . . . . .	69
3.2.1	Breakdown of adiabatic approximation and electron-phonon interaction . . . . .	69
3.2.2	Organization of the section . . . . .	71
3.2.3	Model and Hamiltonian . . . . .	72
3.2.4	General mechanism for long-lived quantum coherence . . . . .	74
3.2.5	Pigment-protein Complex . . . . .	75
3.2.6	Coherence dynamics and excitation energy transfer . . . . .	77
3.2.7	Nonequilibriumness, steady-state coherence and energy transfer . . . . .	82
3.2.8	Effect of multiple vibrational modes . . . . .	84
3.2.9	Discussion and conclusion . . . . .	85
<b>4</b>	<b>Quantum dynamics in ultracold gas and quantum information: relaxation process II</b>	<b>86</b>
4.1	Breakdown of scale invariance in the vicinity of the Tonks-Girardeau limit . . . . .	86
4.1.1	Lieb-Liniger model . . . . .	86
4.1.2	Scale invariance . . . . .	87
4.1.3	Lieb-Liniger gas in a trapping potential . . . . .	88
4.1.4	Bose-Fermi duality . . . . .	89
4.1.5	Monopole excitaiton of a microscopically small amplitude . . . . .	90
4.1.6	Comparison to the other few-body results . . . . .	93
4.1.7	Large- $N$ asymptotics and a comparison with the sum-rule predictions . . . . .	94
4.1.8	Comparison to the frequencies of the excitations of a microscopically large but macroscopically small amplitude . . . . .	97
4.1.9	Conclusion and outlook . . . . .	98
4.2	Nonequilibrium-induced enhancement of dynamical quantum coherence of spin arrays . . . . .	100
4.2.1	Spin-chain model . . . . .	101

4.2.2	Model of spin arrays in random magnetic field from nuclear spins . . . . .	102
4.2.3	Time evolution . . . . .	104
4.2.4	Dynamics of spin qubits . . . . .	105
4.2.5	Non-Markovian and nonequilibrium effects . . . . .	107
4.2.6	Proposed experiment for realizing the dynamics of spin qubits . . . . .	112
4.2.7	Conclusion . . . . .	114
<b>5</b>	<b>Summary and conclusion</b>	<b>116</b>

# List of Figures

2.1	Potential energy landscape . . . . .	6
2.2	Schematic illustration of the Energy Transport in Single Molecules and Chemical Reaction $AB \leftrightarrow C$ . . . . .	13
2.3	Comparison between analytical and numerical results for quantum flux . . . . .	18
2.4	Quantum flux varies with voltage and tunneling strength . . .	20
2.5	Quantum flux varies as a function of coherence and voltage $v$ .	21
2.6	ETE for bosons and CRE(CTE) for fermions vary with coherence, by fixing the voltage . . . . .	26
2.7	ETE and CRE vary with tunneling strength and voltage . . .	27
2.8	EPR and heat current vary as functions of temperature difference; Energy dissipation and electric current vary as functions of chemical voltage . . . . .	29
2.9	EPR and chemical (electric) current vary as functions of coherence . . . . .	31
2.10	Schematic of vibrational energy transport and rotation of ellipse	33
2.11	Rotation angle, eccentricity, density-density correlation $C_4$ and Wilson loop of curl flux . . . . .	40
2.12	2D Illustration of curl quantum flux . . . . .	42
2.13	Energy pumping into molecules, heat current flowing through the molecules and working efficiency vary . . . . .	46
2.14	Time evolution of the smooth part of current-current correlation function . . . . .	48
2.15	Contribution of coherence to heat transport . . . . .	50
3.1	Time evolution of coherence and magnetization (population imbalance) . . . . .	61

3.2	Orientation (coherence) dynamics for the OH-stretching mode of HDO dissolved in D <sub>2</sub> O and 2D plot of $\frac{3-F _{\epsilon=0}}{3-F _{\epsilon=1}}$ . . . . .	63
3.3	Parameter $3 - F$ and energy consumption as a functions of $\epsilon$ . . . . .	65
3.4	Schematic of the deviation of equilibrium of energy surface of excitons . . . . .	70
3.5	Schematic of exciton-environment interaction . . . . .	74
3.6	Schematic of a dimer in pigment-protein complex . . . . .	76
3.7	Time evolution of electronic, excitonic and excited-state vibrational coherence . . . . .	79
3.8	Dynamics of population on pigment $B$ for including and NOT including the incoherent radiation environment . . . . .	81
3.9	Time evolution of electronic coherence when including two vibrational modes . . . . .	83
4.1	Frequency of a small amplitude monopole excitation for $N = 3$ one-dimensional bosons in a harmonic trap, as a function of the inverse of the effective Lieb-Liniger parameter $\gamma_0$ . . . . .	94
4.2	Magnitude of the dominant correction in a power-series expansion in $1/\gamma_0$ , to the result $\Omega_M = 2\omega$ predicted by the scale invariance . . . . .	95
4.3	Frequency of both the microscopically small and microscopically large but macroscopically small monopole excitations in the limit of $N \gg 1$ . . . . .	96
4.4	Dynamics of fidelity of quantum state and real part of coherence	108
4.5	Oscillation period and frequency with respect to effective voltage $V$ . . . . .	110
4.6	Schematics of proposed experiment and stimulated two-photon Raman transition; Simulation of coherence dynamics for 16 ions	113

# Acknowledgements

First and foremost, it is with immense gratitude that I acknowledge the support and supervise of my advisor Prof. Jin Wang. My doctoral endeavor would not have been possible without his constant help and guidance. It has been an edifying experience which I cherish forever to work with Prof. Jin Wang. When working with him, I learned the courage to be independent to propose the projects. His conceptual clarity, creative imagination and physical intuition influence me much on my methodology and taste on scientific research. I am very glad to have been given the opportunity to work on a series of related research projects in a systematic way.

It gives me great pleasure to acknowledge Prof. Maxim Olshanii, a brilliant theoretical physicist in atomic and mathematical physics. I have earned much knowledge from him on theoretical atomic physics which is shown to provide new insight for the projects with Prof. Jin Wang. Besides, these experiences also provided me a good training on how to effectively connect the theoretical work to the experiments.

I would like to thank Prof. Thomas Bergeman, who have given me the guidance at the beginning of my scientific career. Several discussion with him earned me a lot on AMO physics close to the experiments. I gradually made myself clear in mind on the ideas by experimental physicists on analyzing problems, which is significant for working in theoretical physics.

I am thankful to my friends and the members in our research group, who have provided me the instructive discussion and a stimulating research environment. They include Abhishodh Prakash, Zaijong Hwang, Xinyu Zhang, You-Quan Chong, Yutong Pang, Xuan-Hua Wang, Wei Wu, Cong Chen, Yuan Yao, Chunhe Li, Zaizhi Lai, Zhiqiang Yan and Haidong Feng.

I am also deeply indebted to my family for their unconditional support.

# Related Publications

The contents of this dissertation are actually contained in the following publications

1. Zhedong Zhang, Hong-Chen Fu and Jin Wang, “Nonequilibrium-induced enhancement of dynamical quantum coherence of spin arrays in the presence of noisy environments”, submitted to Nat. Commun.
2. Zhedong Zhang and Jin Wang, “Origin of long-lived coherence and excitation dynamics in pigment-protein complexes”, under review by Sci. Rep.
3. Zhedong Zhang, Wei Wu and Jin Wang, “Fluctuation-dissipation theorem of nonequilibrium quantum systems”, accepted by Europhys. Lett.
4. Zhedong Zhang, Vanja Dunjko and Maxim Olshanii, “Atom transistor from the point of view of quantum nonequilibrium dynamics”, New J. Phys. **17**, 125008-125016 (2015)
5. Zhedong Zhang and Jin Wang, “Shape, orientation and magnitude of the curl quantum flux, the coherence and the statistical correlations in energy transport at nonequilibrium steady state”, New J. Phys. **17**, 093021-093034 (2015)
6. Zhedong Zhang and Jin Wang, “Vibrational and coherence dynamics of molecules”, Phys. Chem. Chem. Phys. **17**, 23754-23760 (2015)
7. Steven Choi, Vanja Dunjko, Zhedong Zhang and Maxim Olshanii, “Monopole Excitations of a Harmonically Trapped One-Dimensional Bose Gas from the Ideal Gas to the Tonks-Girardeau Regime”, Phys. Rev. Lett. **115**, 115302-115306 (2015)

8. Zhedong Zhang and Jin Wang, “Assistance of Molecular Vibrations on Coherent Energy Transfer in Photosynthesis from the View of a Quantum Heat Engine”, *J. Phys. Chem. B* **119**, 4662-4667 (2015)
9. Zhedong Zhang and Jin Wang, “Landscape, kinetics, paths and statistics of curl flux, coherence, entanglement and energy transfer in non-equilibrium quantum systems”, *New J. Phys.* **17**, 043053-043072 (2015), *Selected as IOPselect*
10. Zhedong Zhang and Jin Wang, “Curl flux, coherence, and population landscape of molecular systems: Nonequilibrium quantum steady state, energy (charge) transport, and thermodynamics”, *J. Chem. Phys.* **140**, 245101-245114 (2014)
11. Zhedong Zhang, Gregory E. Astrakharchik, David C. Aveline, Steven Choi, Helene Perrin, Thomas H. Bergeman and Maxim Olshanii, “Breakdown of scale invariance in the vicinity of the Tonks-Girardeau limit”, *Phys. Rev. A* **89**, 063616-063622 (2014)
12. Zhedong Zhang and Hong-Chen Fu, “Complete controllability of finite quantum systems with twofold energy level degeneracy”, *J. Phys. A: Math. Theor.* **43**, 215301-215315 (2010)

# Chapter 1

## Introduction

Nonequilibrium quantum physics is of fundamental importance and interest [2, 3, 4, 5, 6]. It is still an extremely hard issue even in today's theoretical physics because of the lack of the knowledge on the basic theories, like the nonequilibrium quantum statistical mechanics. The recent advances on both theory and experiments reveal the fact that the nonequilibrium quantum dynamics plays an essential role on explaining as well as understanding many interesting phenomenons, i.e., the ultrafast energy transfer [7, 8, 9, 10] & long-survived quantum coherence in organic molecules [11, 12, 13, 14, 15], quantum phase transition [16, 17, 18, 19, 20] and the novel transport properties of superfluid gas at low temperature. On the other hand, the nonequilibrium quantum dynamics with detailed-balance-breaking at steady state still remains elusive due to the relationship between the far-from-equilibrium and quantum nature, i.e., coherence and entanglement. Recently it has been shown that in molecular junctions the charge transport can be promoted by steady-state coherence as the system deviates from equilibrium. As is known, the environmental fluctuations always cause the dissipation and loss of coherence in quantum systems [21, 22], which has been widely reflected in spin-qubit dynamics in the study of quantum information. This motivates the exploration of the nonequilibriumness generated by multiple environments in mitigating or eliminating the decoherence.

The role of coherence in nonequilibrium quantum dynamics is inherently significant and has non-trivial physical features. For example, the solar cells and photosynthetic process have shown the evidence of quantum coherence which strongly correlates to the energy conversion and transfer [12, 13, 14, 15, 23]. The remarkably efficient energy transfer accompanied by

the long-lived coherence was observed in two-dimensional femtosecond electronic spectroscopy [23, 24, 25]. This motivates the further investigations of the quantum nature in the molecular aggregates with detailed-balance-breaking. As we discuss in more details in the following chapters, the long-surviving time scale of coherence is related to some discrete intramolecular vibrations [26, 27, 28]. This subsequently results in the breakdown of Born-Oppenheimer adiabatic approximation [29, 30] and the conventional approaches to the problems may need to be abandoned or generalized.

In Chapter 2, we establish a theoretical framework in terms of curl flux for the nonequilibrium quantum dynamical systems at steady state [31, 32, 33]. The nonequilibriumness is realized by connecting the system to two environments with temperature or chemical potential gradient. We find that the coherence can be dramatically enhanced by nonequilibriumness quantified by the curl flux. This provides the microscopic explanation for the enhancement of coherence in molecular junctions at far-from-equilibrium. In addition to the steady-state behavior with detailed-balance-breaking, the relaxation process towards the nonequilibrium steady-state recently attracted much attention, which is studied in Chapter 3 [34, 35]. We demonstrate the *non-trivial* contribution of coherence to the dephasing timescale and dynamical energy transport, by showing the failure of secular approximation introduced before. Contrary to the previous work [36, 37], a coherent process with  $t_1 < t_2$  is exactly elucidated, where  $t_1$  and  $t_2$  are the relaxation timescales of population and coherence dynamics, respectively.

Another important issue in the dynamical relaxation of open quantum systems is the long-lived coherence in some molecular aggregates, recently observed in two-dimensional femtosecond spectroscopy [23, 24, 25]. Despite of the numerical simulations which can recover such phenomenon by including the molecular vibrations [27], we further uncover the mechanism in a general scenario to explain the phenomenon based on effective field theory: the discrete molecular vibrations effectively weaken the exciton-environment interaction, due to the polarons formed by exciton-vibration interaction. This subsequently demonstrates that the vibrational coherence cannot be ignored for understanding the long-lived feature of excitonic coherence, which was debated for a long period before.

As inspired by the recent progress of quantum information sciences [38, 39, 40, 41], we also study in the chapter 4 the dynamical relaxation of spin arrays immersed in the noise produced by nuclear spins. We uncover a novel rapid oscillation of the coherence, fidelity of the collective quantum states of

spin qubits and quantum entanglement, along with large gradient of chemical potential in nuclear spins. This is lacking to be predicted previously and originates intrinsically from the nonequilibrium-induced net current, which quantifies the degree of deviation from equilibrium [31, 33]. Such nonequilibrium-induced coherent oscillation can be feasible in the experiments, by means of the cold-ion-based quantum simulations as eventually pointed out in chapter 4.

# Chapter 2

## Curl flux, coherence and population landscape of nonequilibrium quantum dynamics

The contents in this chapter are based on Ref.[1, 31, 33].

### 2.1 General framework of nonequilibrium classical dynamics

Nonequilibrium dynamics with detailed-balance-breaking plays an important role in many processes including the energy dissipation by environments, e.g., charge transport in molecular junction, ultracold gas flowing between two atomic reservoirs and even the energy transport in biological systems. Classically, a wide range of systems can be dynamically governed by Fokker-Planck equation [42]. In three-dimensional space, it is of the form

$$\frac{\partial}{\partial t}P(\mathbf{r}, t) = -\nabla \cdot (\mathbf{F}P(\mathbf{r}, t)) + \nabla \cdot \nabla \cdot (\mathbf{D}P(\mathbf{r}, t)) \quad (2.1.0.1)$$

where  $P(\mathbf{r}, t)$  is the spacial probability density satisfying the normalization condition  $\int P(\mathbf{r}, t)d^3\mathbf{r} = 1$ .  $\mathbf{F}$  is the drift force produced by random collision with environments and  $\mathbf{D}$  is the diffusion tensor describing the fluctuations during the diffusion. To further elucidate the configuration described by the

Fokker-Planck equation, it is convenient to work in terms of Langevin equation, corresponding to the probability description by Fokker-Planck equation above

$$\dot{\mathbf{r}} = \mathbf{F}(\mathbf{r}) + \mathbf{f}(t) \quad (2.1.0.2)$$

where  $\mathbf{f}(t)$  is the so-called *stochastic force*, which quantifies the random system-environment collisions and subsequently leads to the random trajectories. Usually only the statistical properties of this stochastic force can be obtained:  $\langle \mathbf{f}(t) \rangle = 0$ ,  $\langle \mathbf{f}(t)\mathbf{f}(t') \rangle = 2\mathbf{D}\delta(t-t')$  under the white noise assumption. This reveals that the diffusion matrix  $\mathbf{D}$  describes the random effect of stochastic force on the system, including the magnitude and orientation. It can be precisely shown that the two descriptions by probability and stochastic trajectories are equivalent on predicting the statistical behaviors of the system, under the approximation of weak noise [42]. For our purpose of obtaining the general theoretical framework, we will focus on the probability description here and after.

In most circumstance, the steady state behaviors are what people are mostly interested, namely, the case  $\partial_t P = 0$ . For this case one has  $\nabla \cdot \mathbf{J}(\mathbf{r}, t) = 0$  where

$$\mathbf{J}(\mathbf{r}, t) = \mathbf{F}P_{ss}(\mathbf{r}, t) - \nabla \cdot (\mathbf{D}P_{ss}(\mathbf{r}, t)) \quad (2.1.0.3)$$

by writing the Fokker-Planck equation in the form of continuity equation  $\partial_t P + \nabla \cdot \mathbf{J} = 0$  and  $\mathbf{J}$  is the curl flux of probability. This indicates two different processes: (1)  $\mathbf{J} = 0$  and (2)  $\mathbf{J} = \nabla \times \mathbf{A}$  where  $\mathbf{A}$  is another vector field. As we know, (1) means the protection of detailed balance, indicating the equilibrium processes while (2) results in the detailed-balance-breaking, leading to the nonequilibrium feature. The latter one is recently shown to be the origin of many important phenomenons, such as the robust limit cycle oscillation [43, 44, 45, 1, 46]. In terms of the curl flux  $\mathbf{J}$ , the driving force can be written as [1]

$$\tilde{\mathbf{F}} = -\mathbf{D} \cdot \nabla U_{ss} + \frac{\mathbf{J}_{ss}}{P_{ss}} \quad (2.1.0.4)$$

where the effective driving force is  $\tilde{\mathbf{F}} = \mathbf{F} - \nabla \cdot \mathbf{D}$ . For the constant diffusion  $\tilde{\mathbf{F}} = \mathbf{F}$ .  $U_{ss} = -\ln P_{ss}$  is defined as potential landscape. The force decomposition in Eq.(2.1.0.4) shows that the driving force acting on the system is contributed by two parts: the gradient of landscape and the curl flux. For

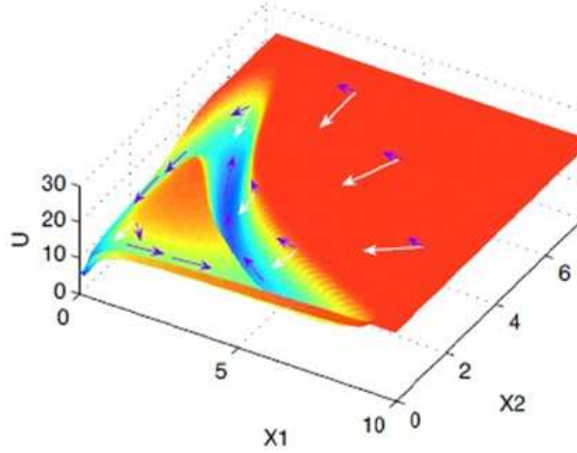


Figure 2.1: (Color online) Potential energy landscape with Mexican hat like closed ring valley shape [1]. The blue arrows represent the flux, and the white arrows represent the force from negative gradient of the energy landscape.

the equilibrium processes (reversal) the force is only determined by landscape  $\tilde{\mathbf{F}} = -\mathbf{D} \cdot \nabla U_{ss}$ , which reflects that the potential landscape completely governs the dynamics of the system. This is in analogy to the Hamilton dynamics [47] in conserved force field. When it comes to the irreversible processes with detailed-balance-breaking, the full dynamics of system can not only be governed by potential landscape, but indeed is also determined by the curl flux breaking the detailed balance. Such residue part of the force, for example, leads to the robust limit cycle oscillation in many chemical systems with the Mexican-hat-like landscape, which cannot be predicted by considering the landscape only. As shown in Fig.2.1, the landscape attracts the system heading to the local minimums of the landscape surface while the curl flux drives the unidirectional motion of the system in the valley of the landscape. In contrast, the system will reside at the valley of landscape in the equilibrium case without the additional driving force.

Besides the Fokker-Planck equation in continuous space, it is also significant to study the dynamics in discrete space, which is alternatively governed by Master Equation

$$\dot{P}_m = - \sum_{n \neq m} M_{nm} P_m + \sum_{n \neq m} M_{mn} P_n \quad (2.1.0.5)$$

where the matrix element  $M_{mn}$  describes the transition probability from state

$n$  to state  $m$  and it satisfies  $\sum_n M_{nm} = 0$  due to the probability conservation. This  $M$  matrix is determined by the intrinsic information of the interactions of system with environments. As similar as the continuous case, the steady state leads to (under Markovian approximation)

$$\sum_{n \neq m} M_{mn} P_n - \sum_{n \neq m} M_{nm} P_m = 0 \quad (2.1.0.6)$$

which indicates two processes as well: (1)  $M_{mn} P_n = M_{nm} P_m$  and (2)  $M_{mn} P_n - M_{nm} P_m \neq 0$ . The former recovers the standard detailed-balance condition in statistical mechanics and the latter results in the nonequilibrium processes with detailed-balance-breaking which goes beyond the framework of conventional statistical mechanics. It is straightforward to show that (1) is definitely satisfied at thermal equilibrium. In general it is proper to introduce the net-flux matrix

$$C_{mn} = M_{nm} P_m^{ss} - {}_{\alpha} M_{nm} P_m^{ss} \quad (2.1.0.7)$$

where  ${}_{\alpha} M_{nm} P_m^{ss} = \min(M_{nm} P_m^{ss}, M_{mn} P_n^{ss})$ .  $C_{mn}$  is called *net flux* from state  $m$  to state  $n$  and obviously  $C_{mn}$  vanishes at equilibrium. For the nonequilibrium case,  $C_{mn} \neq 0$  also quantifies the degree of the deviation from equilibrium at microscopic level [31, 48]. Mathematically the net flux can be decomposed into the superposition of various closed loops if the following theorem is satisfied [48]:

**Theorem 1** *The net flux matrix  $C$  can be decomposed into  $C = \sum_{v=1}^Q R^{(v)}$  where  $R^{(v)}$  is the  $v$ -th closed curl matrix (circular and divergent free), if the following conditions are satisfied*

- (1).  $C_{mn} \geq 0$  for  $m \neq n$  and  $C_{nn} = 0$ ;
- (2).  $C_{mn} C_{nm} = 0$  for  $m \neq n$ ;
- (3).  $\sum_m C_{mn} = \sum_n C_{mn}$

This theorem can be understood as follow: The condition (2) in theorem actually means the unidirection of the flux (e.g.,  $C_{12} C_{21} = 0$  indicates only one direction of the flow can survive!), based on the requirement in condition (1); condition (3) is equivalent to the stationary distribution of population at steady state and the conservation of total population as well. The above

flux-decomposition theorem was mathematically proven at classical level [48]. It is, however, also applicable for the quantum processes at steady state, as what will be elucidated later.

So far, we obtained the theoretical framework for describing in a general scenario the nonequilibrium classical dynamics with detailed-balance-breaking, in both continuous and discrete spaces. The curl flux (continuous) and net flux (discrete) play an important role on governing the full dynamics. As we will see later, these two types of descriptions can be generalized to quantum systems to describe the irreversible dynamics in microscopic world. The flux deviating from equilibrium will be shown to strongly correlate to the quantum coherence and entanglement.

## 2.2 General framework for nonequilibrium quantum dynamics

Here we will establish a general framework and formal description on the quantum non-equilibrium steady state, the curl flux for quantifying the degree of nonequilibriumness as well as the quantum transport. In the forthcoming section more details of such theoretical framework will be illustrated by investigating the energy (charge) transport and thermodynamics of molecular systems. The general Hamiltonian of a quantum system interacting with  $M$  environments is of the form

$$H_0 = \sum_{n,m} h_{nm} |\psi_n\rangle\langle\psi_m| + \sum_{i=1}^M \sum_{\mathbf{k},\sigma} \hbar\omega_{\mathbf{k}\sigma}^{(i),\dagger} a_{\mathbf{k}\sigma}^{(i)} \quad (2.2.0.1)$$

$$H_{int} = \sum_{i,\langle n,m \rangle} \sum_{\mathbf{k},\sigma} g_{\mathbf{k}\sigma}^{(i),nm} \left( |\psi_n\rangle\langle\psi_m| a_{\mathbf{k}\sigma}^{(i),\dagger} + |\psi_m\rangle\langle\psi_n| a_{\mathbf{k}\sigma}^{(i)} \right) \quad (2.2.0.2)$$

where  $\langle n, m \rangle$  indicates that only the pairs of states  $n, m$  with energies  $E_n < E_m$  are considered.  $H_0$  represents the free Hamiltonian of the entire system (system + environments) and  $H_{int}$  represents the couplings or interactions between the system and environments. Here only the single-quanta process is included owing to the low probability of higher order processes. Under the assumption that the environments are of much larger size than the system, the environments can be approximately treated as the static ensemble at thermal equilibrium and we can then study the dynamics of the

system by tracing out the environments (or reservoirs), which leads to the master equation of the reduced density matrix:

$$\frac{d\rho}{dt} = \frac{i}{\hbar}[\rho, H_S] - \frac{1}{2\hbar^2} \sum_{\omega_\mu} \sum_{\omega_\nu} \gamma_{\mu\nu}(\omega_\mu) \left( A^\dagger(\omega_\mu) A(\omega_\nu) \rho \right. \quad (2.2.0.3)$$

$$\left. - A(\omega_\nu) \rho A^\dagger(\omega_\mu) \right) + \text{h.c.} + \mathcal{O}(g^2) \quad (2.2.0.4)$$

where the density matrix can be expanded in terms of the coupling strength between system and environments:  $\rho_t(t) = \rho(t) \otimes \rho_R(0) + \rho_c(t)$ . In the regime of weak coupling, the Markovian approximation where the environments relax in very fast timescale compared to system so that system is memoryless is valid and the operator master equation above can be properly truncated up to the 2nd order of system-environment coupling. It is usually convenient to write the quantum master equation (QME) into Liouville space in which the matrix forms a vector and subsequently the QME reads  $|\dot{\rho}\rangle = \hat{\mathcal{M}}|\rho\rangle$ . In such superspace the inner product of two matrices (vectors) is defined as  $\langle A|B\rangle = \text{Tr}(A^\dagger B)$ . For simplicity, we write the the matrix  $\hat{\mathcal{M}}$  as block form, by separating the population (diagonal elements) and coherence terms (off-diagonal elements) of density matrix

$$\frac{\partial}{\partial t} \begin{pmatrix} \rho_p \\ \rho_c \end{pmatrix} = \begin{pmatrix} \mathcal{M}_p & \mathcal{M}_{pc} \\ \mathcal{M}_{cp} & \mathcal{M}_c \end{pmatrix} \begin{pmatrix} \rho_p \\ \rho_c \end{pmatrix} \quad (2.2.0.5)$$

Here,  $\mathcal{M}_p$  represents the transition matrix in population space.  $\mathcal{M}_c$  represents entanglement between coherence dynamics.  $\mathcal{M}_{pc}$  and  $\mathcal{M}_{cp}$  describe the entanglement between population and coherence dynamics, which in some circumstance, has *non-trivial* effect to the population dynamics.

To study the population dynamics we apply the Laplace transform to the coherence components

$$\varrho_c(s) = (s - \mathcal{M}_c)^{-1} \mathcal{M}_{cp} \varrho_p(s) + (s - \mathcal{M}_c)^{-1} \mathcal{M}_c \varrho_c(0) \quad (2.2.0.6)$$

and the inverse Laplace transform to which gives

$$\rho_c(t) = \int_0^t e^{\mathcal{M}_c(t-\tau)} \mathcal{M}_{cp} \rho_p(\tau) d\tau + e^{\mathcal{M}_c t} \rho_c(0) \quad (2.2.0.7)$$

By substituting Eq.(2.2.0.7) into the dynamical equation for population part in Eq.(2.2.0.5) we obtain the reduced QME in population space

$$\frac{\partial \rho_p}{\partial t} = \mathcal{M}_p \rho_p + \int_0^t [\mathcal{M}_{pc} e^{\mathcal{M}_c(t-\tau)} \mathcal{M}_{cp}] \rho_p(\tau) d\tau + \mathcal{M}_{pc} e^{\mathcal{M}_c t} \rho_c(0) \quad (2.2.0.8)$$

which indicates that the quantum dynamics results in a memory effect other than the random collisions. Thus the dynamical equations of quantum systems in population space follow integral-differential equations. This significantly increases the complexity for solving them, even on the numerical level. For the quantum steady state at long times, however, a simple form of these equations can be derived, by exactly evaluating the integrals in time domain

$$\lim_{t \rightarrow \infty} \int_0^t e^{\mathcal{M}_c(t-\tau)} d\tau = -\mathcal{M}_c^{-1} \quad (2.2.0.9)$$

which leads to the reduced QME at steady state

$$(\mathcal{M}_p - \mathcal{M}_{pc} \mathcal{M}_c^{-1} \mathcal{M}_{cp}) \rho_p^{ss} = 0 \quad (2.2.0.10)$$

Notice that the condition of negativity of the eigenvalues of matrix  $\mathcal{M}_c$  is essential, in order to ensure the convergence of the limit in Eq.(2.2.0.9). Therefore we can define the transfer matrix as  $T_{mn} = \mathcal{A}_{nn,mm}^p \rho_{mm}^p$  for  $m \neq n$  where  $\mathcal{A}^p = \mathcal{M}_p - \mathcal{M}_{pc} \mathcal{M}_c^{-1} \mathcal{M}_{cp}$  and  $T_{mn} = 0$  for  $m = n$ . The transfer matrix can then be decomposed into symmetric and asymmetric parts  $T_{mn} = T_{mn}^s + T_{mn}^{as}$  where  $T_{mn}^s = \alpha \mathcal{A}_{nm}^p \rho_m^p = \min(\mathcal{A}_{nm}^p \rho_m^p, \mathcal{A}_{mn}^p \rho_n^p)$  and  $T_{mn}^{as} = \mathcal{A}_{nm}^p \rho_m^p - \alpha \mathcal{A}_{nm}^p \rho_m^p$ . We can see immediately that the symmetric transfer matrix  $T^s$  preserves the detailed balance and then governs the equilibrium part of full dynamics. On the other hand, it can be also seen that the asymmetric transfer matrix  $T^{as}$  leads to the breakdown of detailed balance, giving the time-irreversibility and nonvanishing net quantum flux at steady state. Since the transfer matrix in some sense controls the dynamics of the quantum system, it is shown that the full quantum dynamics can be decomposed into the contributions by two driving forces. One from  $T^s$  preserves the detailed balance governing the equilibrium part of dynamics while the other from  $T^{as}$  causes the detailed-balance-breaking, giving the flux contribution to driving force and governing the nonequilibrium part of dynamics. This is in similar spirit as the classical case [1, 48] discussed before. Moreover, the driving force obeying detailed balance largely depends on the steady-state populations while

the other one is mainly determined by the population imbalance reflected by  $T^{as}$ . We will further investigate the properties of nonvanishing flux produced by anti-symmetric transfer matrix  $T^{as}$ , as a character of nonequilibriumness.

Alternatively, the asymmetric transfer matrix gives rise to the net quantum flux between different pairs of states

$$\mathcal{J}_{mn} = \mathcal{A}_{nm}^p \rho_m^p - {}_{\alpha} \mathcal{A}_{nm}^p \rho_m^p \quad (2.2.0.11)$$

which obviously satisfies the condition in the Theorem mentioned before. Hence it can be decomposed into superposition of closed loop fluxes. Furthermore we should notice that although the Markov chain looks similar as the classical case, the coefficient  $\mathcal{A}_{nn,mm}^p$  and populations  $\rho_m^p$  are significantly affected by quantum coherence lacking in classical systems. This is because of the existence of  $\mathcal{M}_{pc}$  and  $\mathcal{M}_{cp}$  in the form of  $\mathcal{A}^p$ . We will focus our attention in the following study on the relation between net quantum flux and quantum coherence.

## 2.3 Energy and charge transport in molecular system

We will illustrate our ideas presented above by the energy (charge) transport process in single molecules. The contents in this section are based on Ref.[31].

### 2.3.1 Hamiltonian and quantum master equation

#### Coupled to heat (bosonic) reservoirs

Energy transfer in molecules happens between donor and acceptor sites, after being excited from ground state. To be simple, we assume the excitation energies of these two sites are of a small difference, namely,  $|\varepsilon_1 - \varepsilon_2| \ll \min(\varepsilon_1, \varepsilon_2)$ . In the language of excitons, this system can be modeled as asymmetric double wells, as shown schematically in Fig. 1. Since we would discuss the transport between different sites in molecules, it is clearer to describe the system in local representation. The subspace relevant to our discussion is spanned by the ground state and two additional excitations

$$|\Omega\rangle = B_g^\dagger |0\rangle, \quad |1\rangle = B_1^\dagger B_g |\Omega\rangle, \quad |2\rangle = B_2^\dagger B_g |\Omega\rangle \quad (2.3.1.1)$$

where  $|0\rangle$  stands for the vacuum,  $B_i$  and  $B_j^\dagger$  are the annihilation and creation operators for electrons in molecules. The transport in molecules can be modeled by the system interacting with two identical reservoirs with different temperatures. The free and interaction Hamiltonian then read

$$H_S = E_g|\Omega\rangle\langle\Omega| + \varepsilon_1\eta_1^\dagger\eta_1 + \varepsilon_2\eta_2^\dagger\eta_2 + \Delta(\eta_1^\dagger\eta_2 + \eta_2^\dagger\eta_1) \quad (2.3.1.2)$$

$$H_R = \sum_{\mathbf{k},\sigma} \hbar\omega_{\mathbf{k}\sigma} a_{\mathbf{k}\sigma}^\dagger a_{\mathbf{k}\sigma} + \sum_{\mathbf{q},s} \hbar\omega_{\mathbf{q}s} a_{\mathbf{q}s}^\dagger a_{\mathbf{q}s} \quad (2.3.1.3)$$

$$H_{int} = \sum_{\mathbf{k},\sigma} \lambda_{\mathbf{k}\sigma} (\eta_2^\dagger a_{\mathbf{k}\sigma} + \eta_1 a_{\mathbf{k}\sigma}^\dagger) + \sum_{\mathbf{q},s} \lambda_{\mathbf{q}s} (\eta_1^\dagger b_{\mathbf{q}s} + \eta_2 b_{\mathbf{q}s}^\dagger) \quad (2.3.1.4)$$

where  $\eta$  and  $\eta^\dagger$  are the annihilation and creation operators for excitons which obey the Fermi-Dirac statistics  $\{\eta_a, \eta_b^\dagger\} = \delta_{ab}$ ,  $\{\eta_a, \eta_b\} = 0$ . The scattering between excitons is neglected here. The annihilation and creation operators for the environments (reservoirs) satisfy Bose-Einstein relations:  $[a_{\mathbf{k}\sigma}, a_{\mathbf{k}'\sigma'}^\dagger] = \delta_{\mathbf{k},\mathbf{k}'}\delta_{\sigma\sigma'}$ ,  $[a_{\mathbf{k}\sigma}, a_{\mathbf{k}'\sigma'}] = 0$ .  $\Delta$  represents the electronic coupling (tunneling strength) between the two sites. Here we do not include the vibrational degree of freedoms of the nuclei, due to their fast relaxation within  $\sim 1$ ps, which is much shorter than the time scale of electronic excitation. However, the electric dephasing occurs on a comparable timescale to vibrational relaxation in the light-harvesting and Fenna-Matthews-Olson complexes, therefore we will include this effect in our future work, since this effect goes beyond the scope of current paper.  $p$  and  $s$  denote the polarizations of the boson (either radiation or phonon) field. In Eq.(2.2.0.6) the rotating-wave approximation [49] was applied to exciton-photon interaction term due to the dominant contribution by real absorption and emission. Only the single-exciton process is important to energy transport and then in the single-exciton manifold the Hamiltonians (2.2.0.4) and (2.2.0.6) are taken the forms of  $H_S = E_g|\Omega\rangle\langle\Omega| + \varepsilon_1|1\rangle\langle 1| + \varepsilon_2|2\rangle\langle 2| + \Delta(|1\rangle\langle 2| + |2\rangle\langle 1|)$  and

$$H_{int} = \sum_{\mathbf{k},p} \lambda_{\mathbf{k}p} (\sigma_{2g}^+ a_{\mathbf{k}p} + \sigma_{2g}^- a_{\mathbf{k}p}^\dagger) + \sum_{\mathbf{q},s} \lambda_{\mathbf{q}s} (\sigma_{1g}^+ b_{\mathbf{q}s} + \sigma_{1g}^- b_{\mathbf{q}s}^\dagger) \quad (2.3.1.5)$$

where the creation and annihilation of excitons were replaced by transition, namely,  $\eta_i^\dagger \rightarrow \sigma_{ig}^+ \equiv |i\rangle\langle\Omega|$  and  $\eta_i \rightarrow \sigma_{ig}^- \equiv |\Omega\rangle\langle i|$  ( $i = 1, 2$ ), in the single-exciton manifold. The quantum mechanical tunneling between different sites delocalizes the wave function over the diameter of molecule, which provides

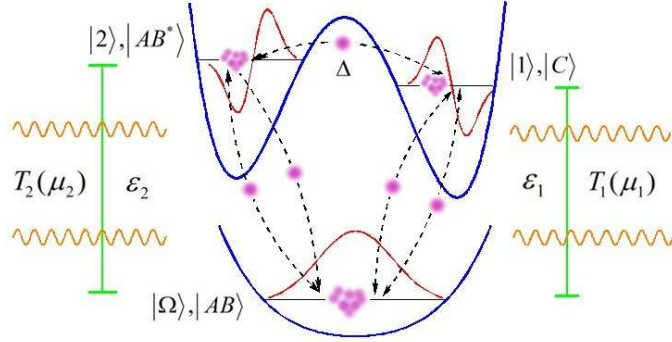


Figure 2.2: (Color online) *Schematic illustration of the Energy Transport in Single Molecules and Chemical Reaction  $AB \leftrightarrow C$* , as discussed in details in our paper. The two reservoirs keep their own temperatures or chemical potentials, respectively. The energy or charge (chemical species) will flow from state  $|2\rangle$  (the intermediate  $|AB^*\rangle$ ) to state  $|1\rangle$  ( $|C\rangle$ )

an intuitive understanding at first step of effects of quantum coherence on transport. Using Bogoliubov transformation [50] the system Hamiltonian in Eq.(2.3.1.4) is diagonalized by switching into delocalized representation. Therefore it is convenient for us to do the further derivation for the quantum master equation with the help of the interaction picture [21, 22] (This is because only the interaction term will appear in the total Hamiltonian and the calculation can then be simplified).

Since we are interested in the evolution of the variables associated with the system only, the equation for the reduced density matrix in the subspace need to be obtained, by performing a partial trace over the reservoir freedoms. As the coupling strength in *Quantum Electrodynamics* is of the order of fine structure constant, the whole solution of density operator can be written as  $\rho_{SR}(t) = \rho_S(t) \otimes \rho_{R_1}(0) \otimes \rho_{R_2}(0) + \rho_c(t)$  with the traceless term in a higher order of coupling, and the system is assumed to be memoryless, which is so-called the Markovian approximation. This is valid when the correlation time scale of reservoirs is much shorter than the time scale for the dynamics of the system. In other words, the reservoirs have the white noise feature, which is applicable for the system maintaining in thermal equilibrium. Therefore the

master equation for reduced density matrix reads

$$\frac{d\rho_S}{dt} = \frac{i}{\hbar} [\rho_S, H_S] - \frac{1}{\hbar^2} e^{-iH_S t/\hbar} \text{Tr}_{R_1 R_2} \int_0^t ds \left[ \tilde{H}_{int}(s), \left[ \tilde{H}_{int}(t), \tilde{\rho}_S(t) \otimes \rho_R(0) \right] \right] e^{iH_S t/\hbar} \quad (2.3.1.6)$$

On inserting the energy in the interaction picture into the equation of motion Eq.(2.3.1.6), then tracing out the environments, the QME in our model is arrived, in the localized representation

$$\dot{\rho}_S = \frac{i}{\hbar} [\rho_S, H_S] - \frac{1}{2\hbar^2} \mathcal{D}(\rho_S) \quad (2.3.1.7)$$

where the form of superoperator  $\mathcal{D}$  will be given in detail in appendix A in Ref.[31].  $n_\omega = \left[ \exp\left(\frac{\hbar\omega}{k_B T}\right) - 1 \right]^{-1}$  is the Bose average occupation on frequency  $\omega$  at temperature  $T$ . The Weisskopf-Wigner approximation that the upper limit of integral over time can be extended to infinity due to the rapid oscillation of the integrand for  $s \ll t$  was used in deriving Eq.(2.3.1.7). Hence the decay rates induced by photon reservoirs are  $\Gamma_a/\hbar^2 = \frac{V}{4\pi^2\hbar^2} \int d^3\mathbf{k} \lambda_{\mathbf{k}}^2 \delta(\omega_{\mathbf{k}} - \omega'_{ag}) = \frac{4\pi^2\lambda}{\hbar} \frac{\omega'^3_{ag} r_m^3}{8\pi^3 c^3}$ ,  $a = 1, 2$  where  $r_m \sim 30\text{nm}$  is the separation between the complex molecules, such as mesobiliverdin (MBV) & dihydrobiliverdin (DBV) molecules in light harvesting complex [13]. The spectral density  $J(\omega) = 4\pi^2\hbar\lambda \frac{\omega^3 r_m^3}{8\pi^3 c^3}$  and  $\lambda$  is the reorganization energy. After some mathematical procedures, we can derive the compact form of QME in Liouville space:  $\partial_t |\rho\rangle = \mathcal{M}|\rho\rangle$ , by writing the density matrix as a super-vector:  $|\rho\rangle = (\rho_{gg}, \rho_{11}, \rho_{22}, \rho_{12}, \rho_{21})^T$  where  $\mathcal{M}_{22}^{11} = \mathcal{M}_{11}^{22} = 0$ ,  $\mathcal{M}_{21}^{12} = \mathcal{M}_{12}^{21} = 0$ . Matrix  $\mathcal{M}$  is determined by Eq.(3.1.2.10). The analytical expressions for the elements in  $\mathcal{M}$  will be given in Appendix A in Ref.[31]. It is easy to verify that  $\sum_{a=g}^2 \mathcal{M}_{kl}^{aa} = 0$  which reveals the charge conservation. Moreover, the coherence terms quantified by the non-zero off diagonal elements of the density matrix  $\rho_{g1}$  and  $\rho_{g2}$  as well as their complex conjugates are absent from QME in that they are only entangled to themselves in the equations of dynamical evolution. Therefore only the coherence between excitations ( $\rho_{12}$  and  $\rho_{21}$ ) contributes to our goal and the discussion can be restricted into the 5-dimensional space.

### Coupled to chemical (fermionic) reservoirs

To describe the transport of chemical recombination dissociation reaction  $AB \leftrightarrow C$  with the vibrationally excited intermediate  $AB^*$ , we model the quantum system interacting with two chemical reservoirs or leads with different chemical potentials which provide the effective chemical pumping for the system through collisions [51]. The three quantum states are denoted by  $|AB\rangle$ ,  $|AB^*\rangle$  and  $|C\rangle$  as schematically shown in Fig.4.3. The Hamiltonian is of the similar form as the one with bosonic reservoirs

$$\begin{aligned}
 H_S &= E_g|\Omega\rangle\langle\Omega| + \varepsilon_1 c_1^\dagger c_1 + \varepsilon_2 c_2^\dagger c_2 + \Delta(c_1^\dagger c_2 + c_2^\dagger c_1) \\
 H_R &= \sum_{\mathbf{k}} \hbar\nu_{\mathbf{k}} a_{\mathbf{k}}^\dagger a_{\mathbf{k}} + \sum_{\mathbf{q}} \hbar\nu_{\mathbf{q}} b_{\mathbf{q}}^\dagger b_{\mathbf{q}} \\
 H_{int} &= \sum_{\mathbf{k}} f_{\mathbf{k}} \left( c_2^\dagger a_{\mathbf{k}} + c_1 a_{\mathbf{k}}^\dagger \right) + \sum_{\mathbf{q}} f_{\mathbf{q}} \left( c_1^\dagger b_{\mathbf{q}} + c_2 b_{\mathbf{q}}^\dagger \right) \quad (2.3.1.8)
 \end{aligned}$$

where the operators for chemical reservoirs obey the Fermi-Dirac statistics:  $\{a_{\mathbf{k}}, a_{\mathbf{k}'}^\dagger\} = \delta_{\mathbf{k}\mathbf{k}'}$  and  $\{b_{\mathbf{q}}, b_{\mathbf{q}'}^\dagger\} = \delta_{\mathbf{q}\mathbf{q}'}$ .  $\Delta$  describes the conversion between states  $|AB^*\rangle$  and  $|C\rangle$  by the tunneling through the barrier. The rotating-wave approximation was applied as well and the occupation will be replaced by fermionic type:  $n_\omega^\mu = \left[ \exp\left(\frac{\hbar\omega - \mu}{k_B T}\right) + 1 \right]^{-1}$ . Instead of the linear dependence on wave vector in radiation fields, the dispersion relation in solvent or semiconductor lead can be approximated by a parabolic law, namely,  $\varepsilon_{\mathbf{k}} \simeq \frac{\hbar^2 k^2}{2m^*}$  where  $m^*$  is the effective mass. Therefore the decay rate reads  $\Gamma_a/\hbar^2 = \frac{1}{\hbar^2} \int d\nu D(\nu) f_\nu^2 \delta(\nu - \omega'_{ag})$  where  $D(\nu) \sim \sqrt{\nu}$  is the density of states, and the spectrum density is  $J(\nu) = D(\nu) f_\nu^2 = \frac{\hbar\lambda}{2\pi} \varphi(\nu)$ , where  $\varphi(\nu)$  is a smooth and dimensionless function, with the magnitude on the order of  $\sim 1$ . Hence the remaining procedures are the same as the bosonic reservoir case above and we will skip the details to avoid redundancy. Finally the reduced QME for fermionic baths can be derived:  $\partial_t |\rho\rangle = \mathcal{M} |\rho\rangle$  in Liouville space. Based on these preparations we are able to develop the quantum curl flux decomposition which will be shown in next section.

### 2.3.2 Curl decomposition and nonequilibrium quantum flux

After deriving the QME in detail in last section, we will, in this section, introduce the curl flux decomposition for quantum steady state which is crucial because it generates a novel quantum flux quantifying the quantum transport and the flux directly reflects the detailed balance breaking and time-irreversibility. The similar decomposition for classical open chemical system at steady state was discussed before [52, 53]. By eliminating the off-diagonal components in density matrix from the reduced QME through Laplace transform we can map the reduced QME into population space, i.e.,  $\partial_t |\rho\rangle = \mathcal{H}|\rho\rangle$  where  $\mathcal{H}$  is a matrix with integral kernel (shown in Appendix B in Ref.[31]) in Liouville space which is the extended Hilbert space and density matrix elements form a supervector. Consequently the quantum effects on transport is somewhat equivalent to the memory effect, which has nothing to do with the mechanisms of collision. This is absent in classical theory described by classical master equation (CME). In this study, we are interested in the quantum non-equilibrium steady state so that we evaluate the integrals by extending the upper limit to  $\infty$  to obtain the reduced QME at steady state

$$\begin{pmatrix} \mathcal{M}_{gg}^{gg} - 2\mathcal{C}_{gg}^{gg} & \mathcal{M}_{11}^{gg} - 2\mathcal{C}_{11}^{gg} & \mathcal{M}_{22}^{gg} - 2\mathcal{C}_{22}^{gg} \\ \mathcal{M}_{gg}^{11} - 2\mathcal{C}_{gg}^{11} & \mathcal{M}_{11}^{11} - 2\mathcal{C}_{11}^{11} & -2\mathcal{C}_{22}^{11} \\ \mathcal{M}_{gg}^{22} - 2\mathcal{C}_{gg}^{22} & -2\mathcal{C}_{11}^{22} & \mathcal{M}_{22}^{22} - 2\mathcal{C}_{22}^{22} \end{pmatrix} \begin{pmatrix} \rho_{gg} \\ \rho_{11} \\ \rho_{22} \end{pmatrix} = 0 \quad (2.3.2.1)$$

where  $\mathcal{C}_{kl}^{mn} \equiv \text{Re}(\mathcal{M}_{12}^{mn} \mathcal{M}_{kl}^{12} / \mathcal{M}_{12}^{12})$  and  $\mathcal{M}$  are defined before. As  $\mathcal{M}_{12}^{12}$  governs the decay rate in the integral kernel, such memorable effect is significant for large  $|\text{Re}(\mathcal{M}_{12}^{12})|$  while it becomes tiny for small  $|\text{Re}(\mathcal{M}_{12}^{12})|$ . The reduced QME in Eq.(2.3.2.1) is of the same form as the CME within Markovian approximation, but with a different explanation: *the quantum effect has already been contained and reflected through  $\mathcal{C}$ -matrix by the exact evaluation of the integral kernel for memory in our QME*, in contrast to previous work with the additional second Markovian approximation [54, 55]. In classical open systems the  $\mathcal{C}$ -matrix vanishes.

## Curl quantum flux determined by the non-equilibriumness and tunneling

Next we need to introduce the non-equilibrium quantum flux in order to investigate the quantum transport. First the transfer matrix has to be defined:  $T_{kl}^{mn} = \mathcal{A}_{mn}^{kl} \rho_{mn}$  with zero diagonal element. Then this  $T$ -matrix can be decomposed into the following form

$$T = \begin{pmatrix} 0 & \mathcal{A}_{gg}^{11} \rho_{gg} & \mathcal{A}_{22}^{gg} \rho_{22} \\ \mathcal{A}_{gg}^{11} \rho_{gg} & 0 & \mathcal{A}_{11}^{22} \rho_{11} \\ \mathcal{A}_{22}^{gg} \rho_{22} & \mathcal{A}_{11}^{22} \rho_{11} & 0 \end{pmatrix} + \begin{pmatrix} 0 & 0 & \mathcal{J}_q \\ \mathcal{J}_q & 0 & 0 \\ 0 & \mathcal{J}_q & 0 \end{pmatrix} \quad (2.3.2.2)$$

The reduced QME in population space directly gives the expression  $\mathcal{J}_q = \mathcal{A}_{22}^{11} \rho_{22} - \mathcal{A}_{11}^{22} \rho_{11}$ . In Eq.(2.3.2.2) the 1<sup>st</sup> term of the transfer matrix describes the equilibrium with detailed balance. The 2<sup>nd</sup> term is circular that we call “non-equilibrium quantum flux”, which plays a crucial role in determining the transport properties of open quantum systems, such as entropy production (EPR), dissipation and efficiency. Moreover, the curl flux matrix in Eq.(2.3.2.2) is closed at steady state, by the application of Theorem 1 before. By solving the QME at steady state under the further approximation  $|\Delta| \ll \min(\varepsilon_1, \varepsilon_2)$ ,  $n_\varepsilon \simeq \frac{1}{2}(n_{\omega'_{1g}} + n_{\omega'_{2g}})$  and  $\Gamma = \frac{1}{2}(\Gamma_1 + \Gamma_2)$ , we can obtain the expression for quantum flux in our model ( $\hbar\omega \equiv \varepsilon_2 - \varepsilon_1$ )

$$\mathcal{J}_q^b = \frac{2\Gamma}{\hbar^2} \frac{v^b \frac{\Delta^2}{\hbar^2 \omega^2}}{1 + 4u^b \frac{\Delta^2}{\hbar^2 \omega^2}}, \quad \mathcal{J}_q^f = \frac{2\Gamma}{\hbar^2} \frac{v^f \frac{\Delta^2}{\hbar^2 \omega^2}}{1 + 4u^f \frac{\Delta^2}{\hbar^2 \omega^2}} \quad (2.3.2.3)$$

and

$$\begin{aligned} v^b &= \frac{(n_\varepsilon^{T_2} - n_\varepsilon^{T_1})(\bar{n}_\varepsilon + 2)}{(1 + 2\bar{n}_\varepsilon + 3n_\varepsilon^{T_1} n_\varepsilon^{T_2}) \left[1 + \frac{\Gamma^2}{\hbar^4 \omega^2} (\bar{n}_\varepsilon + 2)^2\right]} \\ u^b &= \frac{(\bar{n}_\varepsilon + 2)(3\bar{n}_\varepsilon + 2)}{4(1 + 2\bar{n}_\varepsilon + 3n_\varepsilon^{T_1} n_\varepsilon^{T_2}) \left[1 + \frac{\Gamma^2}{\hbar^4 \omega^2} (\bar{n}_\varepsilon + 2)^2\right]} \\ v^f &= \frac{(n_\varepsilon^{\mu_2} - n_\varepsilon^{\mu_1})(2 - \bar{n}_\varepsilon)}{\left[1 + \frac{\Gamma^2}{\hbar^4 \omega^2} (2 - \bar{n}_\varepsilon)^2\right] (1 - n_\varepsilon^{\mu_1} n_\varepsilon^{\mu_2})} \\ u^f &= \frac{\left(1 - \frac{\bar{n}_\varepsilon^2}{4}\right)}{\left[1 + \frac{\Gamma^2}{\hbar^4 \omega^2} (2 - \bar{n}_\varepsilon)^2\right] (1 - n_\varepsilon^{\mu_1} n_\varepsilon^{\mu_2})} \end{aligned} \quad (2.3.2.4)$$

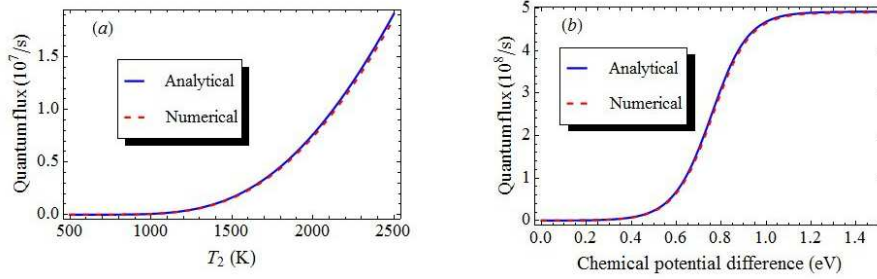


Figure 2.3: (Color online) Analytical and numerical results for quantum flux with (a) bosonic and (b) fermionic reservoirs as a function of bias voltage. Blue(solid) and red(dashed) lines are for analytical and numerical solutions, respectively. Standard parameters are  $\varepsilon_1 = 0.798\text{eV}$ ,  $\varepsilon_2 = 0.8\text{eV}$ ,  $\lambda = 21\text{cm}^{-1}$ ,  $\Delta = 2\text{meV}$  and (a)  $T_1 = 500\text{K}$ , (b)  $T = 700\text{K}$

where the function  $v$  provides a measure for the effective voltage and detailed balance breaking induced from environments. *The flux describes how much probability flows in a uni-direction from one site to another in unit time.* Therefore, the function  $v$  quantifies the degree of non-equilibriumness away from the equilibrium. Then from the expressions of quantum flux in Eq.(2.3.2.3), we can see the quantum transport quantified by the non-equilibrium quantum flux is determined by two factors: non-equilibriumness quantified by the effective voltage away from equilibrium and the quantum tunneling. When the effective voltage is zero, the system is at quantum equilibrium with no quantum flux or quantum transport. On the other hand, when the effective voltage increases, the quantum flux increases. The degree of non-equilibriumness drives the quantum transport. In this model, the quantum transport is realized by tunneling from one site to another. When  $\Delta = 0$ , the flux is zero and there is no quantum transport. The quantum flux increases as the tunneling increases until the tunneling becomes big and the quantum flux reaches a plateau. The quantum tunneling promotes the quantum transport at moderate regime, in that there is no effective barrier any more. The further increasing tunneling will not increase the quantum transport further at very large tunneling strength. See next section for further detailed explanations in a different angle.

Fig.2.3(a) and 2.3(b) give the comparison between our analytical formula for quantum flux Eq.(2.3.2.3) and the results from numerical simulation, as functions of bias (for bosonic bath it is temperature difference while for

fermionic bath it is chemical potential difference). Fig.4.2 shows the variations of quantum flux for bosonic and fermionic reservoirs with respect to voltage as well as tunneling strength. Qualitatively, it is known that the quantum tunneling gives rise to the so-called dark states which is the superposition of two excited states to make the transfer of energy or charge being enhanced, but such contribution will reach the saturation at large value of tunneling. On the other hand it is found that large bias leads to significant enhancement of flux, which indicates that far-from-equilibrium rather than near-to-equilibrium is crucial for the enhancement of quantum flux and the transport. Furthermore, compared to bosonic case, a sharp increase of flux occurs after a particular value of bias, which is about 0.8eV in our plot. This is because of the Fermi-Dirac distribution, where the density of excitations will be much suppressed as the energy becomes larger than Fermi energy. Another distinction is that for bosonic baths the increase of flux becomes sharper as the system deviates from equilibrium while for fermionic baths the flux reaches saturation as the system deviates very far from equilibrium. This is due to the Pauli exclusion principle that for fermions the occupation for each frequency is no more than one.

### **The nontrivial relationships among coherence, tunneling, non-equilibriumness and quantum flux**

Based on QME and the approximation above, we can obtain the quantum coherence. Furthermore the connection of quantum flux to coherence reads  $\mathcal{J}_q^{b(f)} = \frac{2\Delta}{\hbar} \times |\text{Im}\rho_{12}|$ . Notice that the environmental effect was included in the coherence. Right now we can conclude that coherence enhances the non-equilibrium flux through a linear law when fixing the tunneling strength, which reveals the important distinction of the properties of non-equilibrium quantum system from classical description. In order to see how environments and quantum coherence affect the flux as well as ETE (CRE), we can write the coherence in terms of the tunneling strength

$$|\text{Im}\rho_{12}| = \frac{\Gamma v}{\hbar^2 \omega} \frac{\frac{\Delta}{\hbar \omega}}{1 + 4u \frac{\Delta^2}{\hbar^2 \omega^2}} \quad (2.3.2.5)$$

As we can see the coherence has a non-trivial non-monotonic dependence on tunneling as shown in Fig.4.1(a) and moreover the quantum coherence is also promoted by voltage when fixing the tunneling. There is a peak of coherence at  $\Delta_c = \frac{\hbar \omega}{2\sqrt{u}}$ . Then for large  $\Delta$  (which indicates a large coupling

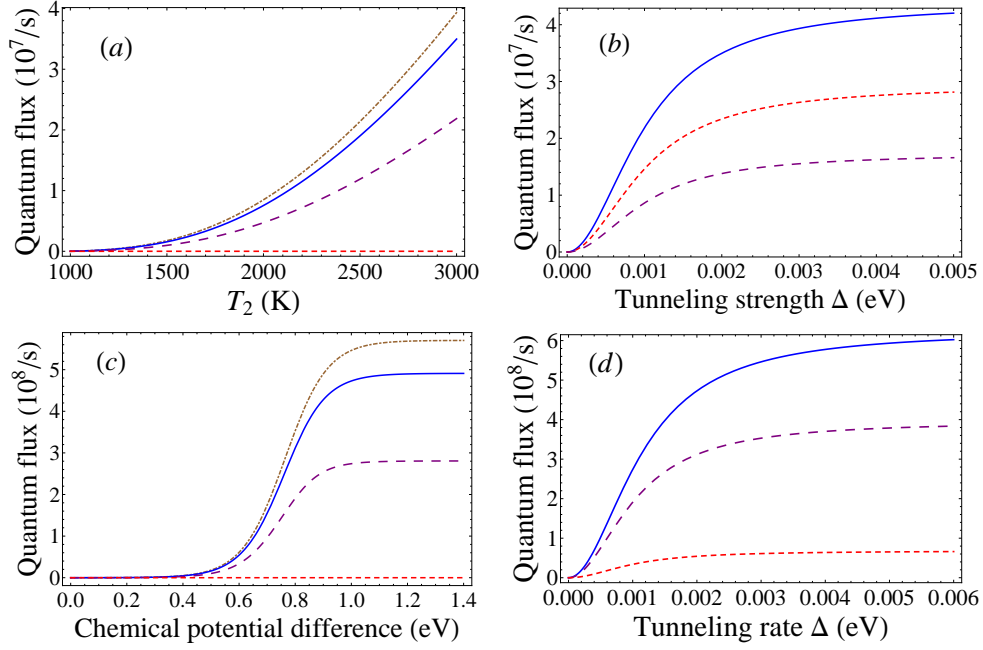


Figure 2.4: (Color online) Quantum flux varies for (a,b) bosonic and (c,d) fermionic reservoirs with (a,c) voltage and (b,d) tunneling strength. (a,c) Brown, blue, purple and red curves correspond to  $\Delta = 3\text{meV}$ ,  $2\text{meV}$ ,  $1\text{meV}$  and  $0$ , respectively; (b) Blue, red and purple curves correspond to  $T_2 = 3000\text{K}$ ,  $2650\text{K}$  and  $2300\text{K}$ , respectively; (d) Blue, purple and red curves correspond to  $\mu_2 = 1.0\text{eV}$ ,  $0.8\text{eV}$  and  $0.6\text{eV}$ , respectively. Standard parameters are  $\varepsilon_1 = 0.798\text{eV}$ ,  $\varepsilon_2 = 0.8\text{eV}$ ,  $\lambda = 21\text{cm}^{-1}$ , (a,b)  $T_1 = 1000\text{K}$  and (c,d)  $T = 900\text{K}$ ,  $\mu_1 = 0$

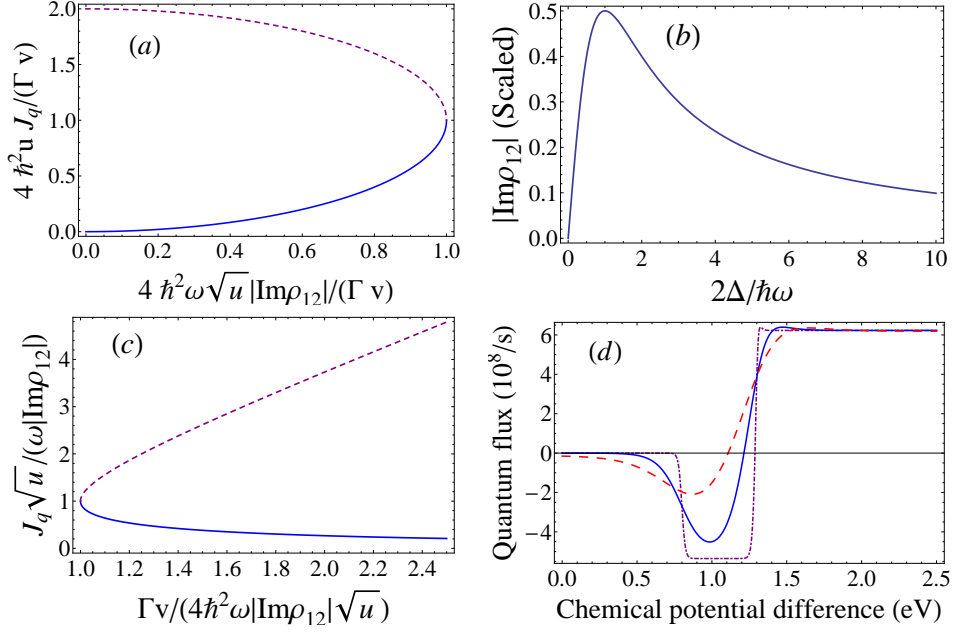


Figure 2.5: (Color online) Quantum flux varies as a function of (a) coherence and (c) voltage function  $v$  for both bosonic and fermionic cases. Flux and coherence are scaled by  $\frac{\Gamma v}{4\hbar^2 u}$  and  $\frac{\Gamma v}{4\hbar^2 \omega \sqrt{u}}$ , respectively. Blue and red curves correspond to  $\Delta < \frac{\hbar \omega}{2\sqrt{u}}$  and  $\Delta > \frac{\hbar \omega}{2\sqrt{u}}$ , respectively; (b) Imaginary part of quantum coherence as a function of tunneling, represented by  $\frac{2\Delta}{\hbar \omega}$ ; (d) Quantum flux varies as a function of chemical potential difference. Purple, blue and red lines are for  $T = 130\text{K}$ ,  $900\text{K}$  and  $1800\text{K}$ , respectively. Standard parameters are  $\varepsilon_1 = 0.9\text{eV}$ ,  $\varepsilon_2 = 1.2\text{eV}$ ,  $\Delta = 0.2\text{eV}$ ,  $\lambda = 21\text{cm}^{-1}$  and  $\mu_1 = 0$

and transport between the molecules) the height of barrier in the middle is effectively lowered. The state  $|2\rangle$  is switched to  $|2'\rangle$  with excitation energy  $\varepsilon'_2 \simeq \bar{\varepsilon} + \Delta$  where  $\bar{\varepsilon} \equiv \frac{1}{2}(\varepsilon_1 + \varepsilon_2)$  and further the distribution of bosons (fermions)  $\sim e^{-\beta\Delta}$ . From the quantum-classical correspondence we know that  $|2'\rangle$  is approaching the classical limit, which means the behavior of particles at this state is close to classical motion. Thus in fact  $|2'\rangle$  becomes a quasi-classical state, which leads to the reduction of coherence for large tunneling. On the other hand, there is an upper limit for tunneling, roughly  $\Delta \sim \bar{\varepsilon}$ , since the lowering of barrier gives rise to the shallowness of the first well, which as a result, leads to the vanishing of bound state if  $\Delta \gg \bar{\varepsilon}$ .

We next explore the relationship between coherence and quantum flux. By eliminating  $\Delta$  in Eq.(2.3.2.3) and (2.3.2.5) it leads to the alternative expression of flux

$$\mathcal{J}_q^{b(f)} = \frac{\Gamma v}{4\hbar^2 u} \left( 1 \pm \sqrt{1 - \frac{16\hbar^4 \omega^2 u |\text{Im}\rho_{12}|^2}{\Gamma^2 v^2}} \right) \quad (2.3.2.6)$$

where  $-$  and  $+$  correspond to  $0 < \Delta < \frac{\hbar\omega}{2\sqrt{u}}$  and  $\Delta > \frac{\hbar\omega}{2\sqrt{u}}$ , respectively. For the small tunneling the flux has the asymptotic form  $\mathcal{J} \simeq \frac{2\hbar^2 \omega^2}{\Gamma v} |\text{Im}\rho_{12}|^2$ . The behavior of flux with respect to coherence is plotted in Fig.4.1(b).

As is shown,  $\mathcal{J}$  first monotonically increases by the improvement of coherence, but then the reduction of the coherence gives rise to the enhancement of the flux. This is mainly because of the non-monotonic behavior of coherence as a function of quantum tunneling discussed above. In the second regime, the increasing tunneling still improves quantum transport but the quasi-classical limit reduces the coherence.

As shown in Eq.(2.3.2.6) and Fig.4.1(c), we see the non-monotonic behavior of the flux with respect to the non-equilibriumness characterized by the voltage at fixed coherence. Again, this non-trivial relationship of flux versus non-equilibriumness quantified by the effective voltage is from the non-trivial relationship between the tunneling and coherence discussed before. Physically Fig.4.1(c) can be explained as the consumption of the energy is used for keeping the coherence such that at small tunneling  $\Delta$  needs to reduce in order to balance out the improvement of coherence by voltage since  $\Delta$  enhances coherence. Hence equivalently much energy absorbed from environments is used to fix the coherence but less to improve flux. In contrast, at large tunneling  $\Delta$  needs to increase, in order to balance out the improvement

of coherence by voltage, therefore much more energy is used to enhance the flux instead of keeping coherence.

We should note that tunneling and voltage are easier to control in the experiment. Therefore, our predictions of dependence of the quantum transport quantified by the flux and tunneling as well as voltage can be tested in the experiment. By the interference techniques developed from quantum optics, researchers have begun to have the control of the coherence. Our predictions of nontrivial dependence of the tunneling and coherence at fixed voltage, the flux and effective voltage at fixed coherence, as well as flux and coherence at fixed voltage, should be tested in the upcoming experiments.

Before leaving this subsection, the non-equilibriumness of quantum systems with non-resonance (shown in Fig.2(d)) will be discussed in detail in appendix B. As the flux decomposition has been carried out at the classical level, we will discuss the comparison of our quantum results to the classical limit in following section.

*The Eq.(2.3.2.3)-(2.3.2.6) & discussion above and the comparison to classical description will be carried out in next section and Eq.(2.3.4.1). These, together with (2.3.4.5) and (2.3.4.8) on efficiency and non-equilibrium quantum thermodynamics, construct the main achievements (concepts) and theoretical framework put forward in this paper.*

### 2.3.3 Comparison with classical description

Here we will discuss the classical correspondence. The non-trivial classical limit in this model is that (a)  $\Omega \gg \omega$  and (b) *high temperature* where (a) keeps the non-vanishing transition rate and also effectively suppress the height of the barrier to ensure one energy level being closed to the top of barrier, (b) is somewhat equivalent to  $\hbar \rightarrow 0$ . Therefore the flux and coherence can be

expanded in terms of  $\omega/\Omega$  and  $\varepsilon/k_B T$  ( $\gamma \equiv \Gamma/\hbar^2$ ,  $\Delta \equiv \hbar\Omega$ )

$$\begin{aligned}
\mathcal{J}_q^b &= \frac{2\gamma T_2 - T_1}{3 T_1 + T_2} + \mathcal{O}\left(\frac{\varepsilon_1 + \varepsilon_2}{k_B T_1}, \frac{\varepsilon_1 + \varepsilon_2}{k_B T_2}, \frac{\omega}{\Omega}\right) \\
\mathcal{J}_q^f &= \frac{\gamma \mu_2 - \mu_1}{6 k_B T} + \mathcal{O}\left(\frac{\varepsilon_1 - \mu_1}{k_B T}, \frac{\varepsilon_2 - \mu_2}{k_B T}, \frac{\omega}{\Omega}\right) \\
|\text{Im}\rho_{12}^b| &= \frac{\gamma T_2 - T_1}{3\omega T_1 + T_2} \left(\frac{\omega}{\Omega}\right) + \mathcal{O}\left(\frac{\varepsilon_1 + \varepsilon_2}{k_B T_1}, \frac{\varepsilon_1 + \varepsilon_2}{k_B T_2}, \frac{\omega^2}{\Omega^2}\right) \\
|\text{Im}\rho_{12}^f| &= \frac{\gamma \mu_2 - \mu_1}{12\omega k_B T} \left(\frac{\omega}{\Omega}\right) + \mathcal{O}\left(\frac{\varepsilon_1 - \mu_1}{k_B T}, \frac{\varepsilon_2 - \mu_2}{k_B T}, \frac{\omega^2}{\Omega^2}\right) \quad (2.3.3.1)
\end{aligned}$$

The leading order term in flux is the classical correspondence where  $\hbar$  disappeared and it is also proportional to the voltage. Quantum effect is attributed to the *higher order terms*. On the other hand, we can also see that *coherence effect comes in since the order of  $\omega/\Omega$* .

On the other hand, by the measurement of coherence the quantum flux shows a non-monotonic behavior as a function of coherence, according to Eq.(2.3.2.6). This is due to the up-hill and down-hill behaviors of coherence as explained in detail in Fig.4.1(a) and 4.1(b) before. From this point, it should be noted that in open quantum systems the coherence does not always enhance the flux and transport, but sometimes it can inhibit them, due to the mixture of classical behavior of motion.

Furthermore, as we know that classical flux monotonically increases as external voltage, shown in Eq.(2.3.3.1). In quantum case, however, it can be clearly illustrated from Eq.(2.3.2.6) that external voltage leads to the decrease of the flux for small tunneling and increase of the flux for large tunneling, by fixing the value of coherence as shown in Fig.4.1(c). The explanations of the behavior is given already in the previous subsection. In next section we will discuss the macroscopic quantum transport relevant to experiments.

### 2.3.4 Quantum transport and non-equilibrium thermodynamics

#### Transfer Efficiency

From the definition of our quantum flux we know that it provides a measurement on how much energy (chemical species) is transported from one site to another. Therefore the energy transfer efficiency (ETE) and chemical reaction efficiency (or charge transfer efficiency) CRE can be introduced in terms of flux, so that  $\eta = \mathcal{J}_q / (\mathcal{J}_q + \mathcal{A}_{22}^{gg} \rho_{22})$ . After some mathematical steps we have

$$\begin{aligned}\eta^b &= \frac{(n_\varepsilon^{T_2} - n_\varepsilon^{T_1}) \frac{\Delta^2}{\hbar^2 \omega^2}}{n_\varepsilon^{T_2} \left[ B(T_1, T_2, \omega) + (\bar{n}_\varepsilon + 2) \frac{\Delta^2}{\hbar^2 \omega^2} \right]} \\ \eta^f &= \frac{(n_\varepsilon^{\mu_2} - n_\varepsilon^{\mu_1}) \frac{\Delta^2}{\hbar^2 \omega^2}}{n_\varepsilon^{\mu_2} \left[ F(\mu_1, \mu_2, T, \omega) + (2 - \bar{n}_\varepsilon) \frac{\Delta^2}{\hbar^2 \omega^2} \right]}\end{aligned}\quad (2.3.4.1)$$

where the two functions  $B$  and  $F$  are defined as

$$\begin{aligned}B(T_1, T_2, \omega) &= \frac{(n_\varepsilon^{T_1} + 1)(n_\varepsilon^{T_2} + 1) \left[ 1 + \frac{\Gamma^2}{\hbar^4 \omega^2} (\bar{n}_\varepsilon + 2)^2 \right]}{\bar{n}_\varepsilon + 2} \\ F(\mu_1, \mu_2, T, \omega) &= \frac{(1 - n_\varepsilon^{\mu_1})(1 - n_\varepsilon^{\mu_2}) \left[ 1 + \frac{\Gamma^2}{\hbar^4 \omega^2} (2 - \bar{n}_\varepsilon)^2 \right]}{2 - \bar{n}_\varepsilon}\end{aligned}\quad (2.3.4.2)$$

As shown in Fig.10 in Appendix in Ref.[31], there are two plateaus in CRE, in contrast to flux. The second one is easy to understand which is due to the Pauli exclusion principle as the same as in flux, the reason for the first plateau is that at the beginning there is an improvement of CRE due to the non-vanishing flux in the non-equilibrium regime. As voltage from environments is below the excitation energy gap  $\varepsilon_2$  the excitations absorbed by the molecular system is suppressed until reaching the gap, then it leads to an abrupt increase to another higher plateau. This is because of the significant improvement of excitations, based on Fermi-Dirac statistics.

In terms of the voltage (temperature difference for heat transport and chemical potential difference for chemical reactions) and quantum coherence, we can use Eq.(2.3.2.5) and (2.3.4.1) to eliminate the tunneling and then obtain the dependence of ETE and CRE (CTE) on voltage and coherence. In

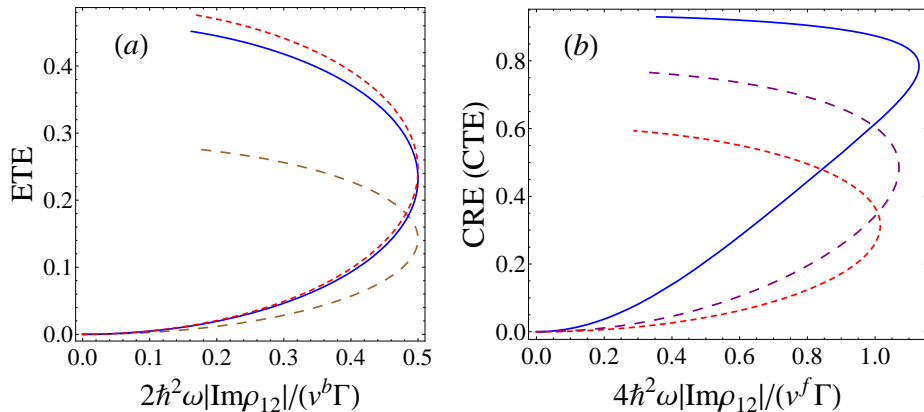


Figure 2.6: (Color online) ETE for bosons and CRE(CTE) for fermions vary with coherence, by fixing the voltage. (a) Brown, blue and red lines are for  $T_2 = 1100\text{K}$ ,  $1400\text{K}$  and  $1800\text{K}$ , respectively; (b) Red, purple and blue lines are for  $\mu_2 = 0.74\text{eV}$ ,  $0.87\text{eV}$  and  $1.0\text{eV}$ , respectively. Standard parameters are  $\varepsilon_1 = 0.798\text{eV}$ ,  $\varepsilon_2 = 0.8\text{eV}$ ,  $\lambda = 21\text{cm}^{-1}$ , (a)  $T_1 = 1000\text{K}$  and (b)  $T = 900\text{K}$ ,  $\mu_1 = 0$

principle, the effect of coherence can be observed from the interference experiments, such as Hamburg-Brown-Twist setup [21]. Fig.2.6(a) and 2.6(b) collect the behavior of the ETE as well as the CRE as functions of coherence at several fixed voltages. For energy transport process in molecules, we found that by fixing the voltage, the increase of the coherence leads to a significant improvement of ETE while in the large tunneling regime ETE is significantly promoted by the reduction of the coherence. For the chemical reaction process and the charge transport in molecules, the coherence plays a crucial role on enhancing the CRE or CTE, as shown in Fig.2.6(b). In the large tunneling regime the influence of coherence is weak, since it approaches the quasi-classical regime. Furthermore, for both bosonic and fermionic reservoirs the voltage from external environments leads to further improvement of transfer efficiency, in addition to coherence.

In order to see how the quantum tunneling and environments affect the ETE and CRE through the bridge of coherence, the ETE and CRE as functions of  $\Delta$  as well as voltage, for both bosonic and fermionic baths, are plotted in Fig.2.7. The tunneling strength and environments characterized by the effective non-equilibrium voltage are shown to have competition on improving the ETE(CRE) and they can compensate for each other. Namely,

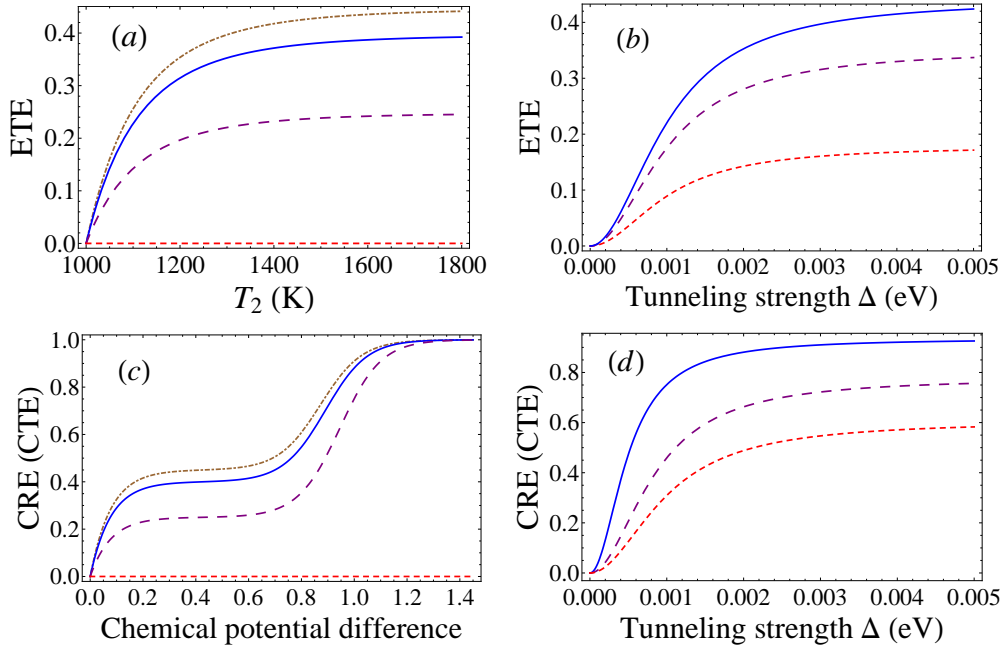


Figure 2.7: (Color online) (a,b)ETE and (c,d)CRE for bosonic and fermionic reservoirs, respectively, vary with tunneling strength and voltage. (a,c) Red, purple, blue and brown lines are for  $\Delta = 0\text{meV}$ ,  $1\text{meV}$ ,  $2\text{meV}$  and  $3\text{meV}$ , respectively; (b) Red, purple and blue lines are for  $T_2 = 1050\text{K}$ ,  $1150\text{K}$  and  $1300\text{K}$ , respectively; (d) Blue, purple and red lines are for  $\mu_2 = 1.00\text{eV}$ ,  $0.87\text{eV}$  and  $0.74\text{eV}$ , respectively. Standard parameters are  $\varepsilon_1 = 0.798\text{eV}$ ,  $\varepsilon_2 = 0.8\text{eV}$ ,  $\lambda = 21\text{cm}^{-1}$ , (a,b)  $T_1 = 1000\text{K}$  and (c,d)  $T = 900\text{K}$ ,  $\mu_1 = 0$

the environments can lead to further enhancement when the hopping leads to saturation, and vice versa. Obviously, the optimization of ETE(CRE) cannot be achieved if any of those two aspects contributes too weakly.

Moreover, we can also see that the transfer efficiency of quantum systems coupled to fermionic environments (CRE) is much better than that for being coupled to heat baths (ETE), since the optimization of CRE is almost a perfect value of 100% from Eq.(2.3.4.1) by  $\mu_2 \rightarrow \infty$ , while ETE's is only about 42% in our model. On the other hand, this indicates that there is little dissipation-decay present in the transport (decay back to ground state in molecule coupled to the bath with higher chemical potential) when the open quantum system is at far-from-equilibrium, in the chemical reaction

process. This kind of high efficiency of 70% was recently observed in the measurement of conductance of a ferrocene-based organometallic molecular wire [56]. In contrast, the heat dissipation is much larger in the quantum heat engine (QHE). This can be understood as follows: from the Fermi distribution we know each mode of the reservoirs with higher chemical potential is fully occupied, thus Pauli exclusion principle causes the emission of one quasi-electron from the molecule back to high-chemical potential reservoir to be forbidden, hence almost all of the excitations are transported to other states. But for bosonic baths, the dissipation is unavoidable since emission of particles is always allowed, without the restriction by Pauli principle.

Finally, as we can see from the discussion above, the large voltage is often necessary and reasonable for optimizing the transport properties, such as ETE and CRE. In particular, in the light-harvesting complex, the radiation bath from the Sun which serves as an energy source is at 5870K [57]. The cooler surrounding, which is originated from the vibrations of proteins in chlorophyll, is at around 200~300K [58]. Consequently the temperature gradient becomes larger than 1000K.

## Macroscopic Currents and Energy Dissipation

In the experiments, the observables provide direct measures of energy dissipation (heat current) and chemical current on the macroscopic level. Therefore we need to explore the connection of the quantum flux and voltage to these macroscopic quantities. First the total entropy production rate (EPR) is introduced  $\dot{S}_t = k_B \mathcal{J}_q \log \frac{A_{gg}^{22} A_{11}^{gg} A_{22}^{11}}{A_{11}^{22} A_{11}^{11} A_{gg}^{22}}$  where coherence effect has been already contained in matrix  $\mathcal{A}$ . Within the near-resonant approximation above, EPR reads

$$\begin{aligned} \dot{S}_t^b &= \frac{\varepsilon_1 + \varepsilon_2}{2} \left( \frac{1}{T_1} - \frac{1}{T_2} \right) \mathcal{J}_q^b \\ \dot{S}_t^f &= k_B \mathcal{J}_q^f \log \frac{n_\varepsilon^{\mu_2} (1 - n_\varepsilon^{\mu_1})}{n_\varepsilon^{\mu_1} \left( 1 - n_\varepsilon^{\mu_2} - \frac{\Delta^2 a_1 / \hbar^2 \omega^2}{\sqrt{1 + 4\Delta^2 / \hbar^2 \omega^2}} \right)} \end{aligned} \quad (2.3.4.3)$$

where  $a_1 \equiv n_{\varepsilon_2}^{\mu_2} - n_{\varepsilon_1}^{\mu_1} - (n_{\varepsilon_1}^{\mu_2} - n_{\varepsilon_2}^{\mu_1})$  and  $b, f$  correspond to bosonic and fermionic reservoirs, respectively. In heat transport, the 1<sup>st</sup> and 2<sup>nd</sup> laws in

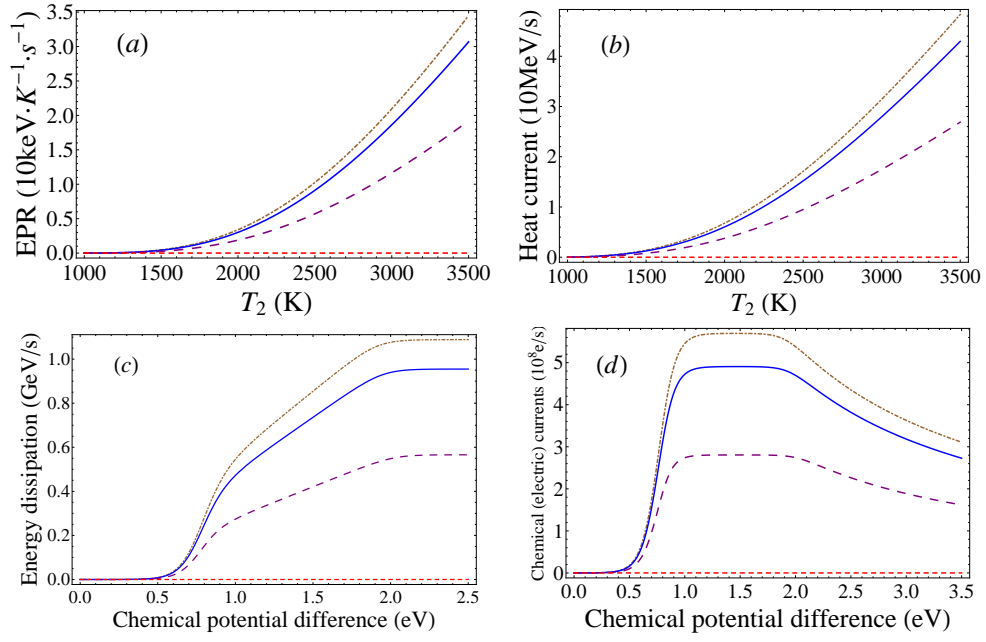


Figure 2.8: (Color online) (a) EPR and (b) heat current vary as functions of temperature difference; (c) Energy dissipation and (d) electric current vary as functions of chemical voltage. (a,b,c,d) Brown, blue, purple and red lines correspond to  $\Delta = 3 \text{ meV}$ ,  $2 \text{ meV}$ ,  $1 \text{ meV}$  and  $0$ , respectively. Standard parameters are  $\varepsilon_1 = 0.798 \text{ eV}$ ,  $\varepsilon_2 = 0.8 \text{ eV}$ ,  $\lambda = 21 \text{ cm}^{-1}$ ,  $T_1 = 1000 \text{ K}$ ,  $T = 900 \text{ K}$  and  $\mu_1 = 0$

thermodynamics give

$$\dot{Q}^b_2 - \dot{Q}^b_1 - \dot{E} = 0, \quad -\frac{\dot{Q}^b_2}{T_2} + \frac{\dot{Q}^b_1}{T_1} + \dot{S} = \dot{S}_t \quad (2.3.4.4)$$

Here 1 or 2 refers to the site 1 or 2 with each coupled with different bosonic bath respectively.  $Q$  denotes the magnitude of energy flowing into reservoir. Notice the entropy production rate  $\dot{S}$  of system vanishes at steady state so that we have the energy dissipation by using Eq.(2.3.4.3) and Eq.(2.3.4.4)

$$\dot{Q}^b_1 = \frac{\varepsilon_1 + \varepsilon_2}{2} \mathcal{J}_q^b \quad (2.3.4.5)$$

which gives  $\dot{Q}^b_1 = -\frac{2\varepsilon t}{\hbar} \text{Im}\rho_{12}$  in the limit  $\theta \rightarrow -\frac{\pi}{2}$ . This recovers the result in Ref.[59] so that our introduction of EPR for quantum steady state has its physical rational. In high temperature limit the asymptotic behaviors of EPR and energy dissipation are shown to be:  $\dot{S}_t^b \sim (T_2 - T_1)^2$  and  $\dot{Q}_1 \sim T_2 - T_1$ , which coincides with Fourier's law. For fermionic reservoirs, the chemical pumping is contributed by chemical flows, carried by the currents flowing into and out from the system

$$I_m^{(2)} - I_m^{(1)} = 0, \quad \frac{\mu_2 I_m^{(2)}}{T} - \frac{\mu_1 I_m^{(1)}}{T} + \dot{S} = \dot{S}_t^f \quad (2.3.4.6)$$

which leads to the chemical current at steady state

$$i_s = \frac{qk_B T}{\mu_2 - \mu_1} \mathcal{J}_q^f \log \frac{n_\varepsilon^{\mu_2} (1 - n_\varepsilon^{\mu_1})}{n_\varepsilon^{\mu_1} \left( 1 - n_\varepsilon^{\mu_2} - \frac{\Delta^2 a_1 / \hbar^2 \omega^2}{\sqrt{1 + 4\Delta^2 / \hbar^2 \omega^2}} \right)} \quad (2.3.4.7)$$

where  $i_s = qI_m^{(2)}$  and the energy dissipation reads

$$\begin{aligned} \dot{Q}_1^f &= \mu_2 I_m^{(2)} - \mu_1 I_m^{(1)} \\ &= k_B T \mathcal{J}_q^f \log \frac{n_\varepsilon^{\mu_2} (1 - n_\varepsilon^{\mu_1})}{n_\varepsilon^{\mu_1} \left( 1 - n_\varepsilon^{\mu_2} - \frac{\Delta^2 a_1 / \hbar^2 \omega^2}{\sqrt{1 + 4\Delta^2 / \hbar^2 \omega^2}} \right)} \end{aligned} \quad (2.3.4.8)$$

Notice that the mathematical forms and analysis for system coupled to fermionic reservoirs Eq.(2.3.2.3), (2.3.4.1), (2.3.4.6)-(2.3.4.8) can also be directly applied to charge transport in single molecules, i.e. electric current

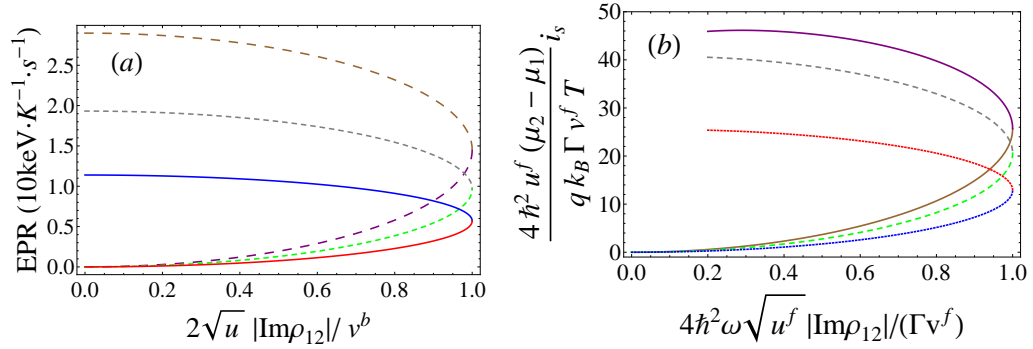


Figure 2.9: (Color online) (a) EPR for energy transport and (b) chemical (electric) current for chemical reaction (charge transport) vary as functions of coherence; (a) Large dashed, medium dashed and solid lines are for  $T_2 = 3200\text{K}$ ,  $2850\text{K}$  and  $2500\text{K}$ , respectively; (b) Tiny dashed, medium dashed and solid lines are for  $\mu_2 = 1.0\text{eV}$ ,  $1.6\text{eV}$  and  $2.2\text{eV}$ , respectively. Standard parameters are  $\varepsilon_1 = 0.798\text{eV}$ ,  $\varepsilon_2 = 0.8\text{eV}$ ,  $\lambda = 21\text{cm}^{-1}$ ,  $T_1 = 1000\text{K}$ ,  $T = 900\text{K}$  and  $\mu_1 = 0$

with  $I - V$  relationship, where  $i_e = eI_m$ , which will be addressed later on the correlation to the experiments. Eq.(2.3.4.3), (2.3.4.5), (2.3.4.7) and (2.3.4.8) show that the nonequilibrium quantum flux serves as a driving force for the macroscopic energy dissipation and chemical (electric) current directly measured in experiments. The physical currents are generated and detailed balance condition is broken when the energy pump emerges ( $T_1 \neq T_2$  or  $\mu_1 \neq \mu_2$ ). This furthermore reveals the robustness of the connection between non-equilibriumness and quantum transport and provides a measurement on how non-equilibriumness controls the transport properties.

Fig.2.8 collects the voltage dependence of transport coupled to both bosonic and fermionic environments. The heat current shows a monotonic increase with respect to temperature difference, which is reasonable due to the large energy pumping with increasing temperature and large dissipation at far-from-equilibrium. Due to the Pauli principle for fermions in recombination dissociation reactions in chemical process, there is an upper limit for the pumping work at steady state illustrated in Fig.2.8(c). Thus the chemical current will drop at high voltage (shown by large  $\mu_2$  limit in Eq.(2.3.4.7) and Fig.2.8(d)). This has been observed for electric current in the experiments on  $I - V$  curve of electron transfer in single molecules [60].

To see the coherence effect on the macroscopic EPR, heat current, chemical (electric) current and energy dissipation, we apply Eq.(2.3.2.3)-(2.3.2.6) to Eq.(2.3.4.3), (2.3.4.5), (2.3.4.7) and (2.3.4.8) by eliminating the tunneling  $\Delta$ , similar to the transfer efficiency studied in the previous subsection. These behaviors are shown in Fig.2.9(a) and 2.9(b) by fixing voltages, for energy transport and chemical reaction (charge transport), respectively. Due to the fixed voltage, those macroscopic observables are different from each other up to just a scaled factor, so that we only display the EPR and chemical (electric) current here. As shown in Fig.2.9(a) and 2.9(b), the non-monotonic behaviors of those macroscopic observables in terms of the coherence indicate that the coherence does not always promote the transport. In the large tunneling regime coherence inhibits the quantum transport. This is distinct from the behavior of these macroscopic observables with respect to tunneling which always enhances the quantum transport. The non-monotonic behaviors in Fig.2.9 are due to the non-monotonic dependence of the coherence with respect to the tunneling, as discussed in the flux section.

### 2.3.5 Conclusion and remarks

In this section, we systematically developed the concept and quantification of curl flux for non-equilibrium quantum processes at steady state. The curl quantum flux measures the degree of non-equilibriumness via detailed balance breaking and time-irreversibility. It also reflects the degree of quantum coherence. We further applied our theoretical framework to the quantum transport in energy (charge) transfer in single molecules and the chemical recombination dissociation reactions. More significantly, the quantum flux is also sensitively affected by coherence which could be observed by quantum interference experiments. The coherence leads to the non-monotonic behavior of the flux, depending on the magnitude of quantum mechanical tunneling. Furthermore we investigated quantum transport and thermodynamics of the system in terms of our quantum flux. We found that the non-equilibrium quantum flux serves as an intrinsic driving force for the macroscopic observables such as currents in quantum transport. *These are the main innovation and achievements in this paper, mathematically illustrated in Eq.(2.3.2.3)-(2.3.2.6), Eq. (2.3.4.1), Eq. (2.3.4.3), Eq.(2.3.4.5), Eq.(2.3.4.7) and Eq.(2.3.4.8).*

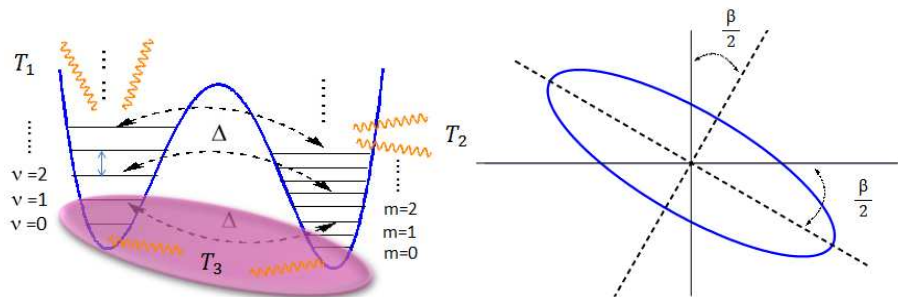


Figure 2.10: (Color online) (Left) Schematic of vibrational energy transport in molecular system. Multi-level in each potential well represents the eigenstates of harmonic oscillator; (Right) Rotation of the ellipse to its principal axis.

## 2.4 Curl quantum flux in continuous space and vibrational energy transport

We will alternatively develop the formalism for describing nonequilibrium behaviors of quantum system in continuous space, based on the investigation of coupled harmonic oscillators connecting to multiple energy sources. This model can be used to study the vibrational energy transport in molecules surrounded by solvent. The curl quantum flux breaking detailed balance will be explored in coherent representation, by taking advantage of the bosonic features of the considered system.

The contents in this section are based on Ref.[33].

### 2.4.1 Model and Hamiltonian

We consider the molecular vibrations (i.e., C=O stretching) described by two quantum-mechanically coupled oscillators with different frequency  $\omega_1$  and  $\omega_2$  which are immersed into the solvent environment at the interface. The free Hamiltonian for the system and solvent environment in terms of the

displacements of oscillations reads

$$H_{ssf} = \sum_{j=1}^2 \left( \frac{p_j^2}{2m_j} + \frac{1}{2}m_j\omega_j^2 x_j^2 \right) + \kappa \left( \sqrt{m_1 m_2} \omega_1 \omega_2 x_1 x_2 + \frac{1}{\sqrt{m_1 m_2}} p_1 p_2 \right) + \sum_{\mathbf{f}, \sigma} \left( \frac{\tilde{p}_{\mathbf{f}\sigma}^2}{2\tilde{m}_{\mathbf{f}}} + \frac{1}{2}\tilde{m}_{\mathbf{f}}\omega_{\mathbf{f}\sigma}^2 \tilde{x}_{\mathbf{f}\sigma}^2 \right) \quad (2.4.1.1)$$

where the low-energy fluctuation solvent environment is treated as a set of harmonic oscillators, neglecting the anharmonic effect hereafter. Actually this effect becomes important under some conditions which goes beyond the scope of this article and we would address this issue in the forthcoming studies.  $m_j$  and  $\tilde{m}_{\mathbf{k}}$  are the effective masses of the molecular-vibrations and environmental vibration mode  $\mathbf{k}$ , respectively;  $p_j$  and  $x_j$  are the canonical momentum and coordinate (describing the displacement of the oscillation), respectively.  $\kappa$  is dimensionless that characterizes the coupling strength between two oscillators. In Eq.(2.4.1.1) we only pick up the minimal coupling between oscillation modes, in order to elucidate our model. It is in general replaced by the dipole-dipole interaction in many chemical systems. The interaction between the system and solvent environment is in similar form as that between the vibrations

$$H_{int}^{ss} = \sum_{i=1}^2 \sum_{\mathbf{f}, \sigma} \lambda_{\mathbf{f}\sigma}^{ss} \left( \sqrt{m_i \tilde{m}_{\mathbf{f}}} \omega_i \omega_{\mathbf{f}\sigma} x_i \tilde{x}_{\mathbf{f}\sigma} + \frac{1}{\sqrt{m_i \tilde{m}_{\mathbf{f}}}} p_i \tilde{p}_{\mathbf{f}\sigma} \right) \quad (2.4.1.2)$$

Additionally one oscillator interacts with a heat source characterizing the energy pump from the chemical reactions, and the other one interacts with a cooler environment which harvests the energy transferred by molecular vibrations, as shown in Fig.2.10. The quantum-mechanically effective couplings of system to these reservoirs can be realized by exchanging the energy quanta. Generally the interaction between molecule stretching is mediated via the dipole-dipole coupling, therefore in the formalism of *Quantum Field Theory*, the free Hamiltonian of system+reservoirs+environment is

$$H_0 = \bar{\varepsilon}_1 a_1^\dagger a_1 + \bar{\varepsilon}_2 a_2^\dagger a_2 + \bar{\Delta} (a_1^\dagger a_2 + a_2^\dagger a_1) + \sum_{\nu=1}^3 \sum_{\mathbf{k}, \sigma} \hbar \omega_{\mathbf{k}\sigma} b_{\mathbf{k}\sigma}^{(\nu)\dagger} b_{\mathbf{k}\sigma}^{(\nu)} \quad (2.4.1.3)$$

and the interactions are

$$H_{int} = \sum_{i=1}^2 \sum_{\mathbf{k}, p} g_{\mathbf{k}p} \left( a_i^\dagger b_{\mathbf{k}p}^{(i)} + a_i b_{\mathbf{k}p}^{(i),\dagger} \right) + \sum_{\mathbf{q}, \sigma} g_{\mathbf{q}\sigma} \left( c^\dagger b_{\mathbf{q}\sigma}^{(3)} + c b_{\mathbf{q}\sigma}^{(3),\dagger} \right) \quad (2.4.1.4)$$

where  $c \equiv a_1 + a_2$  and  $b_{\mathbf{k}\sigma}^{(1)}$ ,  $b_{\mathbf{k}\sigma}^{(2)}$  and  $b_{\mathbf{k}\sigma}^{(3)}$  are the bosonic annihilation operators for heat source, cool reservoir and solvent environment, respectively.  $\sigma$  and  $p$  denote the polarizations of bosons in the reservoirs. The rotating-wave approximation (RWA) [21, 22] has been applied to the vibration-bath interactions, owing to the dominant contribution by real absorption and emission of quanta in long time limit. The effect of vibron-phonon interaction (VP) can be approximately described by the renormalized frequency gap  $\delta\bar{\varepsilon} = \bar{\varepsilon}_1 - \bar{\varepsilon}_2$  and coupling strength  $\bar{\Delta}$  of the molecular vibrations [61]. This in particular, indicates that the tuning between frequencies  $\delta\bar{\varepsilon} \ll \bar{\Delta}$  (strong VP) makes the wave packet of vibrations extended while the large detuning between frequencies  $\delta\bar{\varepsilon} \gg \bar{\Delta}$  (weak VP) makes the wave packet localized, as elaborately illustrated in Anderson localization mechanism [62, 63], in which the disorder (both diagonal and off-diagonal) is imaged to be connected with the presence of impurities, vacancies and dislocations in an ideal crystal lattice, or the random distributions of atoms and molecules [64].

## 2.4.2 Quantum Master Equation in coherent space

The dynamics of the system is governed by the reduced quantum master equation (RQME), which is obtained by tracing out the degree of freedoms (DOF) of the baths. As we pointed out above and also discussed in previous papers [12, 58, 61], the strong interactions between the system and some discrete vibrational modes (i.e., the hydrogen bond) owing to the quasi-resonance between frequencies, leads to the comparable time scales between the vibrational modes and system, which subsequently acquires us to include the dynamics of these discrete vibrational modes together with the system. In other words, these vibrational modes must be separated from the reservoirs. Thereby the remaining modes consisting of the low-energy fluctuations can be reasonably treated as the baths, which are effectively in weak coupling to the systems due to the mismatch of frequencies between these continuous modes and the system. On the basis of perturbation theory, the whole solution of the density operator can be written as  $\rho_{SR} = \rho_s(t) \otimes \rho_R(0) + \rho_\delta(t)$  with

the traceless term in higher orders of couplings between system and reservoirs. Because the time scale associated with the environmental correlations is much smaller than that of system over which the state varies appreciably, the RQME for the reduced density matrix of the systems in the interaction picture can be derived under the so-called Markoff approximation

$$\begin{aligned} \frac{d\rho_s}{dt} = & \frac{1}{2\hbar^2} \left\{ \sum_{\nu=1}^2 \sum_{p=1}^2 [\gamma_p^{T\nu,+} (a_p \rho_s a_\nu^\dagger - a_\nu^\dagger a_p \rho_s) + \gamma_p^{T\nu,-} (a_p^\dagger \rho_s a_\nu - a_\nu a_p^\dagger \rho_s)] \right. \\ & \left. + \sum_{j=1}^2 \sum_{p=1}^2 [\gamma_p^{T3,+} (a_p \rho_s a_j^\dagger - a_j^\dagger a_p \rho_s) + \gamma_p^{T3,-} (a_p^\dagger \rho_s a_j - a_j a_p^\dagger \rho_s)] \right\} + \text{h.c.} \end{aligned} \quad (2.4.2.1)$$

where the reservoirs and solvent environment are in thermal equilibrium. The dissipation rates  $\gamma_{\dots}$  are given in Appendix A in Ref.[33].  $n_\omega^T = [\exp(\hbar\omega/k_B T) - 1]^{-1}$  is the Bose occupation on frequency  $\omega$  at temperature  $T$ . The mixture angle reads

$$\cos 2\theta = \frac{\bar{\varepsilon}_2 - \bar{\varepsilon}_1}{\sqrt{(\bar{\varepsilon}_1 - \bar{\varepsilon}_2)^2 + 4\bar{\Delta}^2}}; \quad \sin 2\theta = -\frac{2\bar{\Delta}}{\sqrt{(\bar{\varepsilon}_1 - \bar{\varepsilon}_2)^2 + 4\bar{\Delta}^2}} \quad (2.4.2.2)$$

Conventionally the QME in Eq.(2.4.2.1) was solved in Liouville space [3, 65], by writing the density matrix as a supervector. This strategy however, seems to be unrealizable due to the infinite dimension of Fock space for bosons. Here we will solve the QME in the coherent representation, which was first developed by Glauber [66]. It is alternatively named as  $P$ -representation, according to the terminology in quantum optics [21, 22, 67]. As is known, the eigenstate of the annihilation operators is  $|\alpha_1, \alpha_2\rangle$  where the eigenequation  $a_j |\alpha_1, \alpha_2\rangle = \alpha_j |\alpha_1, \alpha_2\rangle$  is satisfied. In terms of these components, the density matrix can be expanded into the following form [21]

$$\rho_s(t) = \int P(\alpha_\beta, \alpha_\beta^*, t) |\alpha_1, \alpha_2\rangle \langle \alpha_1, \alpha_2| d^2\alpha_1 d^2\alpha_2 \quad (2.4.2.3)$$

where  $P(\alpha_\beta, \alpha_\beta^*, t)$  is called the quasi-probability, due to the overcompleteness of the coherent basis and the non-positive definition of  $P(\alpha_\beta, \alpha_\beta^*, t)$ . But this quasi-probability is always non-negative everywhere if the quantum system has classical analog [68]. Using Eq.(2.4.2.3) we can project the QME

into coherent space and then obtain the following dynamical equation for  $P(\alpha_\beta, \alpha_\beta^*, t)$

$$\begin{aligned} \frac{\partial}{\partial t} P(\alpha_\beta, \alpha_\beta^*) &= \gamma \left[ 2 \left( \frac{\partial}{\partial \alpha_1} \alpha_1 + \frac{\partial}{\partial \alpha_2} \alpha_2 \right) + \frac{\partial}{\partial \alpha_1} \alpha_2 + \frac{\partial}{\partial \alpha_2} \alpha_1 + \text{c.c.} \right] P(\alpha_\beta, \alpha_\beta^*) \\ &+ \gamma \left[ 2Y_1^1 \frac{\partial^2}{\partial \alpha_1^* \partial \alpha_1} + 2Y_2^2 \frac{\partial^2}{\partial \alpha_2^* \partial \alpha_2} + Y_{12}^{21} \left( \frac{\partial^2}{\partial \alpha_1^* \partial \alpha_2} + \frac{\partial^2}{\partial \alpha_1 \partial \alpha_2^*} \right) \right] P(\alpha_\beta, \alpha_\beta^*) \end{aligned} \quad (2.4.2.4)$$

where the coefficients  $Y_{..}$  are given in Appendix A in Ref.[33]. Eq.(2.4.2.4) is of the same formalism as the classical Fokker-Planck equation [42], apart from the complex variables. Moreover, this equation describes the Ornstein-Uhlenbeck process in the phase space, so that it is exactly solvable. Now we focus on the steady-state case with  $t \rightarrow \infty$ , and therefore the steady-state solution is of Gaussian type

$$P_{ss}(\alpha_\beta, \alpha_\beta^*) = \frac{1}{Z} e^{-[a|\alpha_1|^2 + b|\alpha_2|^2 + 2c\text{Re}(\alpha_1^* \alpha_2)]} \quad (2.4.2.5)$$

with the  $a$ ,  $b$  and  $c$  being

$$\begin{aligned} a &= \frac{4(Y_1^1 + 7Y_2^2 - 2Y_{12}^{21})}{(Y_1^1 + Y_2^2)^2 + 4[3Y_1^1 Y_2^2 - (Y_{12}^{21})^2]}, \quad b = \frac{4(7Y_1^1 + Y_2^2 - 2Y_{12}^{21})}{(Y_1^1 + Y_2^2)^2 + 4[3Y_1^1 Y_2^2 - (Y_{12}^{21})^2]} \\ c &= \frac{8(Y_1^1 + Y_2^2 - 2Y_{12}^{21})}{(Y_1^1 + Y_2^2)^2 + 4[3Y_1^1 Y_2^2 - (Y_{12}^{21})^2]}, \quad Z = \frac{\pi^2}{12} \left\{ (Y_1^1 + Y_2^2)^2 + 4[3Y_1^1 Y_2^2 - (Y_{12}^{21})^2] \right\} \end{aligned} \quad (2.4.2.6)$$

In the forthcoming sections, we will discuss the nonequilibrium behaviors and heat transport based on this steady-state solution of quasi-probability in Eq.(2.4.2.5) and (2.4.2.6).

### 2.4.3 Shape and orientation of the curl flux and vibration correlations in non-equilibrium quantum systems

#### Shape and orientation of curl flux

The quantitative description of nonequilibriumness, especially the far-from-equilibrium case in quantum systems was devoid, although it is known that

macroscopical current would be observed if the system deviates from equilibrium. Recently the curl flux in discrete space was developed to describe the nonequilibrium behaviors in quantum systems [31, 32]. Here we will alternatively develop a curl quantum flux in the continuous space, in analogous with the classical case [1]. We are able to write the probabilistic evolution of diffusion equation (2.2.0.9) covering the whole coherent space into the form of  $\partial_t P + \nabla_\alpha \cdot \mathbf{J} = 0$  which gives the steady-state case  $\nabla_\alpha \cdot \mathbf{J} = 0$ . For the nonequilibrium systems at steady state in general, this does not necessarily mean that the flux  $\mathbf{J}$  has to vanish, due to the detailed-balance-breaking. Instead, the divergence-free nature implies that the flux is a rotational curl field in coherent space. To further elucidate the nonequilibrium nature of the curl quantum flux, we will reduce our discussion into the space spanned by  $(x_1, x_2)$  where  $x_j = \text{Re}[\alpha_j]$ . On the other hand, the issue of even and odd variables then does not arise, because of the time-reversibility of  $x_j$ .

Assuming  $\alpha_j = x_j + ip_j$  where  $x_j = \sqrt{2m_j\omega_j/\hbar}\langle\alpha_1, \alpha_2|\hat{x}_j|\alpha_1, \alpha_2\rangle$  are the dimensionless means of the displacements of the oscillators in coherent space, the dynamical equation of probability in  $(x_1, x_2)$  space becomes

$$\begin{aligned} \frac{\partial}{\partial t}P(x_1, x_2) = & \gamma \left( 2\frac{\partial}{\partial x_1}x_1 + 2\frac{\partial}{\partial x_2}x_2 + \frac{\partial}{\partial x_1}x_2 + \frac{\partial}{\partial x_2}x_1 \right) P(x_1, x_2) \\ & + \frac{\gamma}{2} \left( Y_1^1 \frac{\partial^2}{\partial x_1^2} + Y_2^2 \frac{\partial^2}{\partial x_2^2} + Y_{12}^{21} \frac{\partial^2}{\partial x_1 \partial x_2} \right) P(x_1, x_2) \end{aligned} \quad (2.4.3.1)$$

the steady-state solution to which reads

$$P_{ss}(x_1, x_2) = \frac{\sqrt{ab - c^2}}{\pi} e^{-(ax_1^2 + bx_2^2 + 2cx_1x_2)} \quad (2.4.3.2)$$

Thus the curl quantum flux is of the form

$$\begin{aligned} \mathcal{J}_{x_1} = & \frac{\gamma(Y_1^1 - Y_2^2)P_{ss}}{(Y_1^1 + Y_2^2)^2 + 4[3Y_1^1Y_2^2 - (Y_{12}^{21})^2]} \\ & \times [2(Y_1^1 + Y_2^2 - 2Y_{12}^{21})x_1 + (7Y_1^1 + Y_2^2 - 2Y_{12}^{21})x_2] \end{aligned} \quad (2.4.3.3)$$

$$\mathcal{J}_{x_2} = -\frac{\gamma(Y_1^1 - Y_2^2)P_{ss}}{(Y_1^1 + Y_2^2)^2 + 4[3Y_1^1Y_2^2 - (Y_{12}^{21})^2]} \quad (2.4.3.4)$$

$$\times [(Y_1^1 + 7Y_2^2 - 2Y_{12}^{21})x_1 + 2(Y_1^1 + Y_2^2 - 2Y_{12}^{21})x_2] \quad (2.4.3.5)$$

The behaviors of curl quantum flux are illustrated in Fig.2.12, which provides a description of nonequilibriumness on microscopic level. It is straightforward to prove that the stream lines of the curl flux in 2D space in our case form a set of ellipses, with the major axis in the vicinity of the anti-diagonal line. Therefore the polarization of the curl flux can be quantified in terms of geometric language, namely the *eccentricity*  $\bar{e}$  and *rotation angle*  $\beta/2$

$$\bar{e} = \sqrt{\frac{2\sqrt{(a-b)^2 + 4c^2}}{a+b + \sqrt{(a-b)^2 + 4c^2}}}, \quad \sin\beta = -\frac{2c}{\sqrt{(a-b)^2 + 4c^2}} \quad (2.4.3.6)$$

In particular, based on Eq.(2.4.3.1) and (2.4.3.2) we know that the shape and orientation of curl flux is governed by the eccentricity  $\bar{e}$  and rotation angle  $\beta/2$  where the polarization is in slender-cigar shape along the vicinity of the line  $|x_1| = |x_2|$  as  $\bar{e}$  increases and  $\beta/2$  approaches  $\pi/4$ .

Fig.2.12(a) and 2.12(b) show the effect of vibron-phonon coupling (VP) on the curl flux with the eccentricities  $\bar{e} = 0.978$  and  $\bar{e} = 0.957$ , respectively. As we can see, the strong-VP-bond-contributed delocalization of the excited vibrational modes causes the flux to be more polarized in the vicinity of anti-diagonal than the weak-VP-bond-contributed localization does, which as explored later, means that the correlation between the molecular vibrations is much stronger as quasi-particles become delocalized, rather than the localization of quasi-particles. The quality of heat transport will be promoted as the correlation between vibrations becomes strong, as shown in the following discussion. Fig.2.12(c) and 2.12(d) show that the thermal fluctuations in heat source which in some sense dictates the effective thermal voltage, can definitely strengthen the molecular-vibration correlation, which will considerably raise the heat transport, as will be shown in Fig.2.13(c). Fig.2.12(e) and 2.12(f) illustrate the effect of solvent environment on the curl flux, which shows that the correlation between molecular vibrations is unavoidably suppressed by the thermal fluctuations induced by solvent environment.

### Measure of magnitude of curl flux

Due to the vector feature of the curl flux, here we will use the Wilson loop to quantify the value of the curl flux, based on the integral of curl flux along a specific closed path

$$W = \frac{1}{L} \int_{\Sigma} J_{x_1} dx_1 + J_{x_2} dx_2 \quad (2.4.3.7)$$

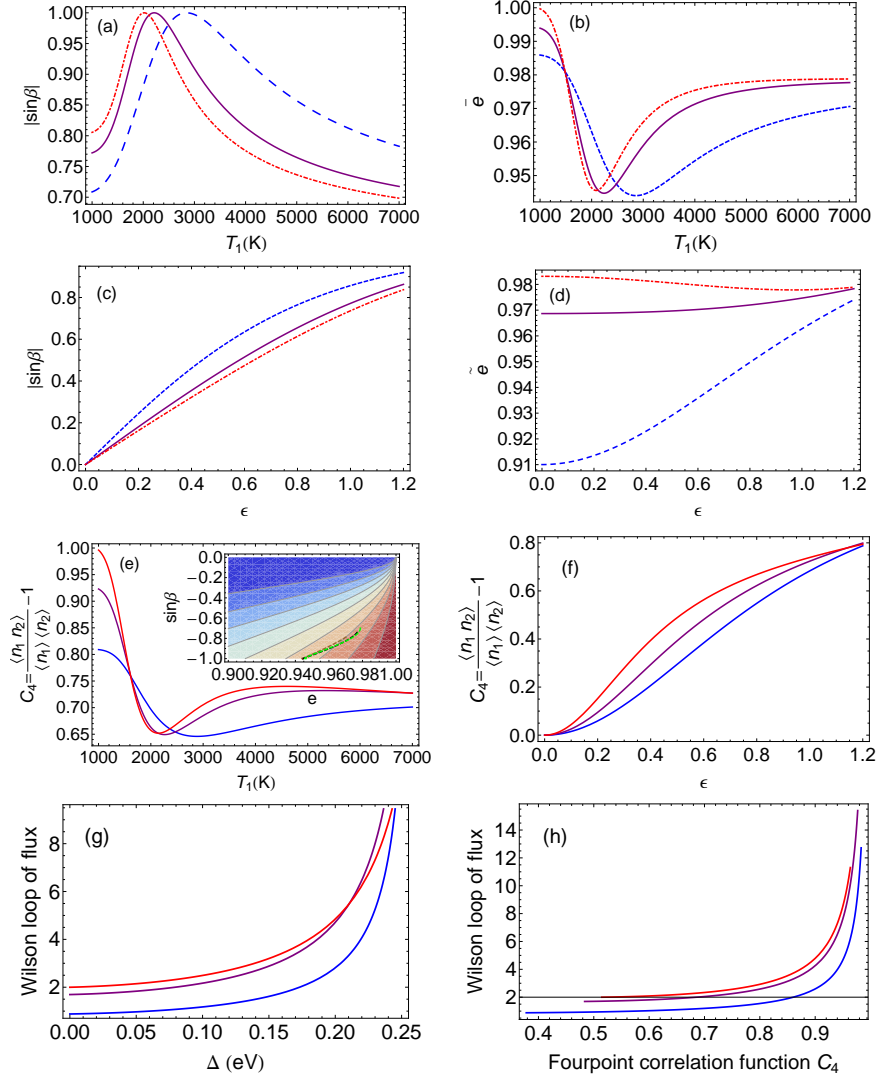


Figure 2.11: (Color online) (a) Rotation angle and (b) eccentricity as a function of  $T_1$ ; (c) Rotation angle and (d) eccentricity as a function of the coherence-population entanglement; (e) density-density correlation  $C_4$  (large) via  $T_1$  as well as 3D illustration of  $C_4$  via eccentricity and rotation angle (small) according to Eq.(2.4.3.9), (f) density-density correlation vary as a function of the coupling strength between coherence and population dynamics; (g) Wilson loop of curl flux as a function of  $\bar{\Delta}$ ; (h) Relationship between Wilson loop of curl flux and  $C_4$  by controlling  $\bar{\Delta}$ . The blue (dashed), purple (solid) and red (dotdashed) lines in correspond to  $\delta\bar{\epsilon} = 0.3, 0.1, 0.01\text{eV}$ , respectively; In (c,d,g,h)  $T_1 = 5000\text{K}$ . Other parameters are  $\bar{\Delta} = 0.1\text{eV}$ ,  $T_2 = 2000\text{K}$  and  $T_3 = 1000\text{K}$ .

where  $L$  represents the length of closed path  $\Sigma$ . Currently we choose the closed path as one of the stream lines of curl flux in 2D space, to maximize the quantity  $W$  in Eq.(2.4.3.7). After some manipulations the Wilson loop of curl flux reads

$$W = \frac{\gamma|Y_1^1 - Y_2^2|(a+b)}{16E(\frac{\pi}{2}|\bar{e}^2)\sqrt{\bar{e}}} \sqrt{\frac{ab - c^2}{a+b + \sqrt{(a-b)^2 + 4c^2}}} \quad (2.4.3.8)$$

Notice that  $e = 2.71828\dots$  is the Euler's number and  $E(\phi|k^2)$  is the elliptic integral of the second kind. As is shown in Fig.2.11(g), the detailed-balance is more broken as the two molecules approaches each other, governed by the increase of  $\frac{\bar{\Delta}}{\delta\bar{e}}$ . This can be understood by an extreme case that the two molecular vibrations will equilibrate individually with the environments as they becomes infinitely distanced with no correlation between each other ( $\bar{\Delta} = 0$ ).

### Relationship between curl flux and vibration correlation

The correlations between the molecular vibrations are measured by the correlation functions. In particular, we mainly focus on the four-point correlation function here, which corresponds to the density-density correlations

$$C_4 = \frac{\langle a_1^\dagger a_1 a_2^\dagger a_2 \rangle}{\langle a_1^\dagger a_1 \rangle \langle a_2^\dagger a_2 \rangle} - 1 = \frac{\bar{e}^4 \sin^2 \beta}{4(1 - \bar{e}^2) + \bar{e}^4 \sin^2 \beta} \quad (2.4.3.9)$$

where  $\bar{e}$  shares the same definition of the eccentricity as before, and  $\beta/2$  is the angle between the major axis of the ellipse and  $x$ -axis. Eq.(2.4.3.9) follows the definition of density-density correlation function in the site basis, as given in Ref.[21].  $C_4 = 0$  indicates that the occupations on the two vibrational modes are uncorrelated. Eq.(2.4.3.9) in fact uncovers the connection between the microscopic nonequilibriumness (flux) and the macroscopic observables in a geometric manner. Hence it is evident to say that *the correlations between molecular vibrations are characterized by the polarization of the curl flux in coherent space, where the slender-cigar type of polarization of flux along the anti-diagonal means the strong vibrational correlations while the cake type of polarization with tiny inhomogeneity or polarization along the axis means the weak vibrational correlations*. Possibly the microscopic curl quantum flux can be explored in experiments, by measuring these geometric parameters

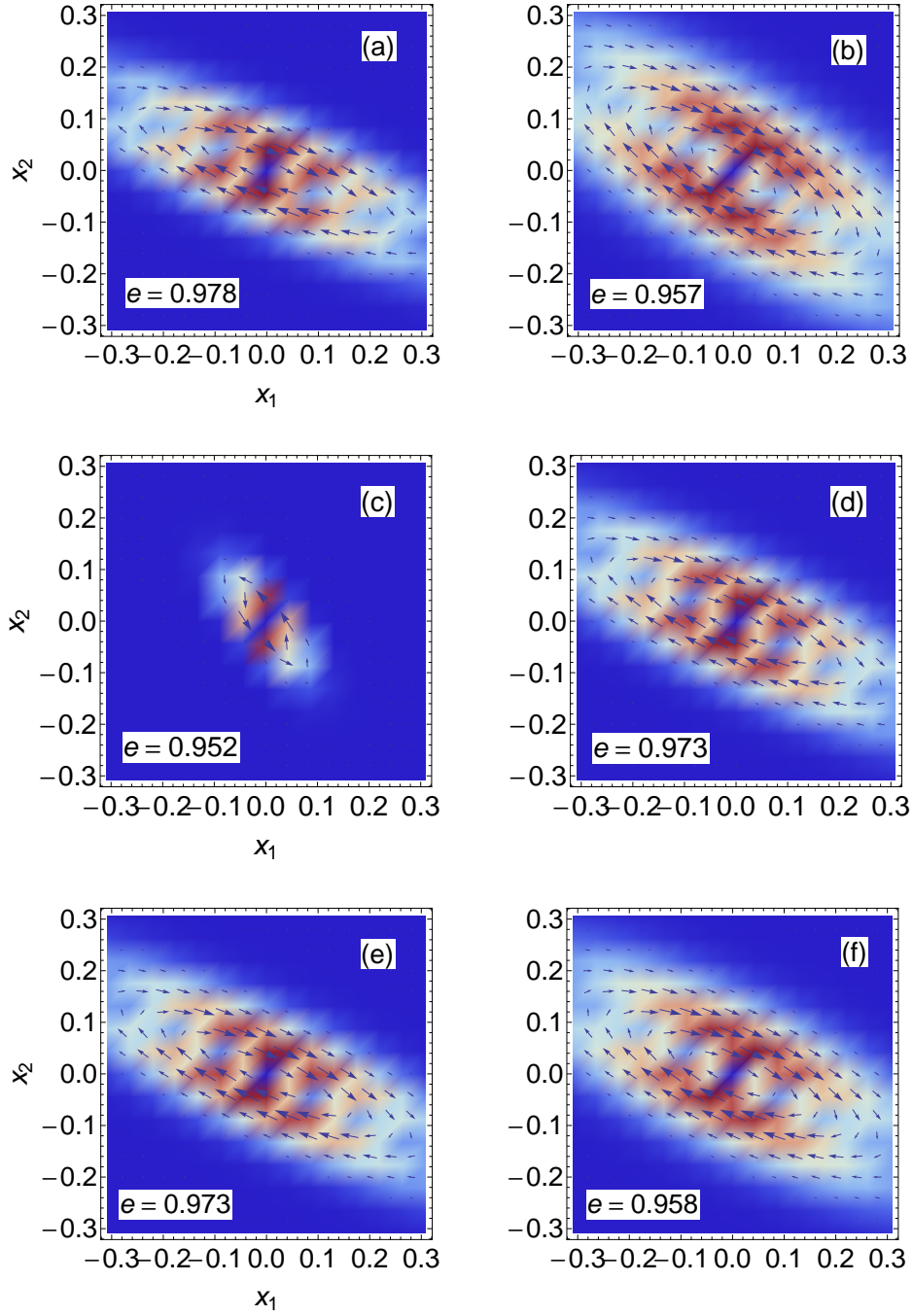


Figure 2.12: (Color online) 2D Illustration of curl quantum flux. (a)  $\bar{\Delta} = 0.1\text{eV}$ ,  $\delta\bar{\varepsilon} = 0.01\text{eV}$  and (b)  $\bar{\Delta} = 0.1\text{eV}$ ,  $\delta\bar{\varepsilon} = 0.35\text{eV}$  where  $T_1 = 5000\text{K}$  and  $T_3 = 1000\text{K}$ ; (c)  $T_1 = 2000\text{K}$ ,  $T_3 = 1000\text{K}$  and (d)  $T_1 = 5000\text{K}$ ,  $T_3 = 1000\text{K}$  where  $\bar{\Delta} = 0.1\text{eV}$ ,  $\delta\bar{\varepsilon} = 0.15\text{eV}$ ; (e)  $T_1 = 5000\text{K}$ ,  $T_3 = 1000\text{K}$  and (f)  $T_1 = 5000\text{K}$ ,  $T_3 = 2000\text{K}$  where  $\bar{\Delta} = 0.1\text{eV}$ ,  $\delta\bar{\varepsilon} = 0.15\text{eV}$ . Other parameters are  $\bar{\varepsilon}_1 = 1\text{eV}$  and  $T_2 = 2000\text{K}$ . Notice that (d) and (e) are the same. However, the reason why we keep (e) here is to provide a control to (f), showing the effect of solvent. In these figures, the eccentricity is denoted by  $e$ .

through the measurement of density-density correlation function, which has been recently probed in degenerate quantum gas [69, 70].

The large figure in Fig.2.11(e) show that (i) the thermal fluctuations in the heat source do strengthen the vibration correlations and (ii) the detuning between the frequencies of molecular vibrations destroys the vibration correlations, as long as the heat transport is on track (this will be examined in detail in the section of heat transport). These properties are also microscopically reflected by curl flux, as shown in Fig.2.11(a), Fig.2.11(b) and the paths (dashed lines) on the landscape of density-density correlation  $C_4$  in the small figure in Fig.2.11(e), in spite of the reduction of the contribution by rotation angle. Besides the geometry of the curl flux, the promotion of the magnitude of curl flux (quantified by Wilson loop) is also strongly correlated to the increase of correlation function, by improving the coupling strength between vibrational modes, as shown in Fig.2.11(h).

As will show later in the section of coherence effect, the site-basis coherence has no contribution to the heat transport in the secular approximation since it is decoupled from the population dynamics. As approaching this regime, one can easily demonstrate that  $\lim_{\epsilon \rightarrow 0} \tilde{c} = 0$  in Eq.(2.4.5.4), which subsequently gives  $\beta \rightarrow 0$ . Hence  $\lim_{\epsilon \rightarrow 0} C_4 = 0$ , which is physically reasonable owing to the polarization of flux at the moment orientated in the vicinity of  $x_1$ -axis. As the entanglement between coherence and population dynamics adiabatically increases, the macroscopic correlation  $C_4$  is considerably promoted by coherence from the microscopic curl flux as it becomes significantly polarized with the angle approaching  $-\frac{\pi}{4}$ , as illustrated in Fig.2.11(c,d) and Fig.2.11(f). Therefore we can conclude that the coherence generates and considerably improves the correlation between the molecular vibrations.

#### 2.4.4 Heat transport intermediated by molecular vibrations

To uncover the behaviors of vibrational energy transport in the molecules, one essentially needs to study the macroscopic heat current flowing through the molecular chain, output work in the view of the system as a quantum heat engine (QHE) and the efficiency quantifying the quality of this QHE. On the other hand, the correlation between the heat currents are also useful to measure to heat transport.

## Heat current and working efficiency

We first introduce the heat-current operators  $J_1$ ,  $J_2$  for the heat currents pumping into and flowing out from the system, respectively. By ignoring the back influence of system to reservoirs, the current operators are defined as  $J_\nu = \frac{1}{i\hbar}[H_s, H_{int}^{(\nu)}]$ , and furthermore in our system

$$\begin{aligned} J_1 &= \frac{1}{i\hbar} \sum_{\mathbf{k}, \sigma} g_{\mathbf{k}\sigma} \left[ \left( \bar{\varepsilon}_1 a_1^\dagger + \bar{\Delta} a_2^\dagger \right) b_{\mathbf{k}\sigma}^{(1)} - \text{h.c.} \right] \\ J_2 &= \frac{i}{\hbar} \sum_{\mathbf{k}, \sigma} g_{\mathbf{k}\sigma} \left[ \left( \bar{\varepsilon}_2 a_2^\dagger + \bar{\Delta} a_1^\dagger \right) b_{\mathbf{k}\sigma}^{(2)} - \text{h.c.} \right] \end{aligned} \quad (2.4.4.1)$$

To calculate the heat current up to the 2nd order of coupling strength, we need to carry out the 1st order correction to the density matrix so that  $\rho_s(t) = \rho_s(0) + \frac{i}{\hbar} \int_0^t [\rho_s(\tau), \tilde{H}_{int}(\tau)] d\tau$ . Substituting this into the product  $\rho_s(t) \tilde{J}_1(t)$  and after a lengthy derivation shown in SM of Ref.[33] the subsequent heat current pumping into the molecules is

$$\begin{aligned} \langle J_1 \rangle_{ss} &= \lim_{t \rightarrow \infty} \text{Tr}[\rho_s(t) \tilde{J}_1(t)] \\ &= (-\gamma) \left[ 2\bar{\varepsilon}_1 \langle a_1^\dagger a_1 \rangle + \bar{\Delta} \langle a_1^\dagger a_2 + a_2^\dagger a_1 \rangle - 2(E_1 n_{\nu_1}^{T_1} \cos^2 \theta + E_2 n_{\nu_2}^{T_1} \sin^2 \theta) \right] \\ &= -\frac{\gamma}{6} \left\{ \left[ E_1 (7\cos^2 \theta - 2\sin \theta \cos \theta) + E_2 (7\sin^2 \theta + 2\sin \theta \cos \theta) \right] Y_1^1 \right. \\ &\quad \left. + \left[ E_1 (\cos^2 \theta - 2\sin \theta \cos \theta) + E_2 (\sin^2 \theta + 2\sin \theta \cos \theta) \right] (Y_2^2 - 2Y_{12}^{21}) \right. \\ &\quad \left. - 12(E_1 n_{\nu_1}^{T_1} \cos^2 \theta + E_2 n_{\nu_2}^{T_2} \sin^2 \theta) \right\} \end{aligned} \quad (2.4.4.2)$$

where  $\hbar\nu_1 = \frac{1}{2} \left[ \bar{\varepsilon}_1 + \bar{\varepsilon}_2 - \sqrt{(\bar{\varepsilon}_1 - \bar{\varepsilon}_2)^2 + 4\bar{\Delta}^2} \right]$  and  $\hbar\nu_2 = \frac{1}{2} \left[ \bar{\varepsilon}_1 + \bar{\varepsilon}_2 + \sqrt{(\bar{\varepsilon}_1 - \bar{\varepsilon}_2)^2 + 4\bar{\Delta}^2} \right]$  are the eigenenergies of the coupled oscillators. Moreover the coherence contribution to heat currents  $J_1, J_2$  is governed by the term  $\langle a_1^\dagger a_2 + a_2^\dagger a_1 \rangle$  which will vanishes in secular approximation as shown later.  $\langle a_1^\dagger a_2 \rangle = \sum_{n_1, n_2} \sqrt{n_1 n_2} \langle n_1 - 1, n_2 | \rho_s | n_1, n_2 - 1 \rangle$ . The similar manner for calculating the heat current mediated by the molecular vibrations and we can simply

replace the  $\tilde{H}_{int}^{(1)}$  by  $\tilde{H}_{int}^{(2)}$  in  $J_1$ , to reach the following result

$$\begin{aligned} \langle J_2 \rangle_{ss} = \frac{\gamma}{6} \left\{ [E_1 (\sin^2\theta - 2\sin\theta\cos\theta) + E_2 (\cos^2\theta + 2\sin\theta\cos\theta)] (Y_1^1 - 2Y_{12}^{21}) \right. \\ \left. + [E_1 (7\sin^2\theta - 2\sin\theta\cos\theta) + E_2 (7\cos^2\theta + 2\sin\theta\cos\theta)] Y_2^2 \right. \\ \left. - 12 (E_1 n_{\nu_1}^{T_2} \sin^2\theta + E_2 n_{\nu_2}^{T_2} \cos^2\theta) \right\} \quad (2.4.4.3) \end{aligned}$$

As a QHE, the stationary working efficiency of the vibrational energy transport is naturally defined as  $\eta = \frac{\langle J_2 \rangle_{ss}}{\langle J_1 \rangle_{ss}}$ . Fig.2.13(a) shows the effect of external pumping on the heat flowing into the system according to Eq.(2.4.4.2), which demonstrates the improvement of energy pumping into system by the activity of external heat source. Since the excitation energy in our system is around 1eV, the considerable excitation with respect to this energy scale needs the effective temperature of the environment to be around 5000 K. On the other hand, the analog is the light-harvesting complex in which the temperature of radiations is around 5800K. Fig.2.13(c) and 2.13(e) illustrate the heat flow (quantifying the vibrational energy transfer) and working efficiency  $\eta$  under the influence of external energy pumping by heat source, according to Eq.(2.4.4.2) and (2.4.4.3). As seen first, the thermal fluctuation and pumping of the external heat source causes a considerable improvement of the energy transferred by the molecular vibrations and the working efficiency reflected in Fig.2.13(e) as well. More importantly, it is also shown in Fig.2.13(c) that the energy transport relates to a critical value of  $(\delta\bar{\epsilon}, T_1)$ , under which the vibrational energy transport is suspended. The critical points are determined by acquiring  $\langle J_2 \rangle_{ss} = 0$  which will be shown in Supplementary Materials (SM) of Ref.[33]. In Fig.2.13(c) the critical values of  $T_1$  are 3372K, 2514K and 2257K with respect to  $\delta\bar{\epsilon} = 0.3, 0.1, 0.01\text{eV}$ , respectively. Above the critical point, the promotion of energy current flowing through molecules and the efficiency by thermal fluctuation of the heat source and also the frequency detuning between molecular vibrations can be critically demonstrated by the polarization of the curl flux, illustrated in Fig.2.12(c,d) and Fig.2.12(a,b), respectively, since the correlation between the molecular vibrations is enhanced which will be reached later. Therefore we can evidently claim that *the curl quantum flux in Eq.(2.4.2.5) and (2.4.2.6) on microscopic level significantly correlates to and characterizes the vibrational energy transport on macroscopic level*. We will come back to this issue when discussing the correlation

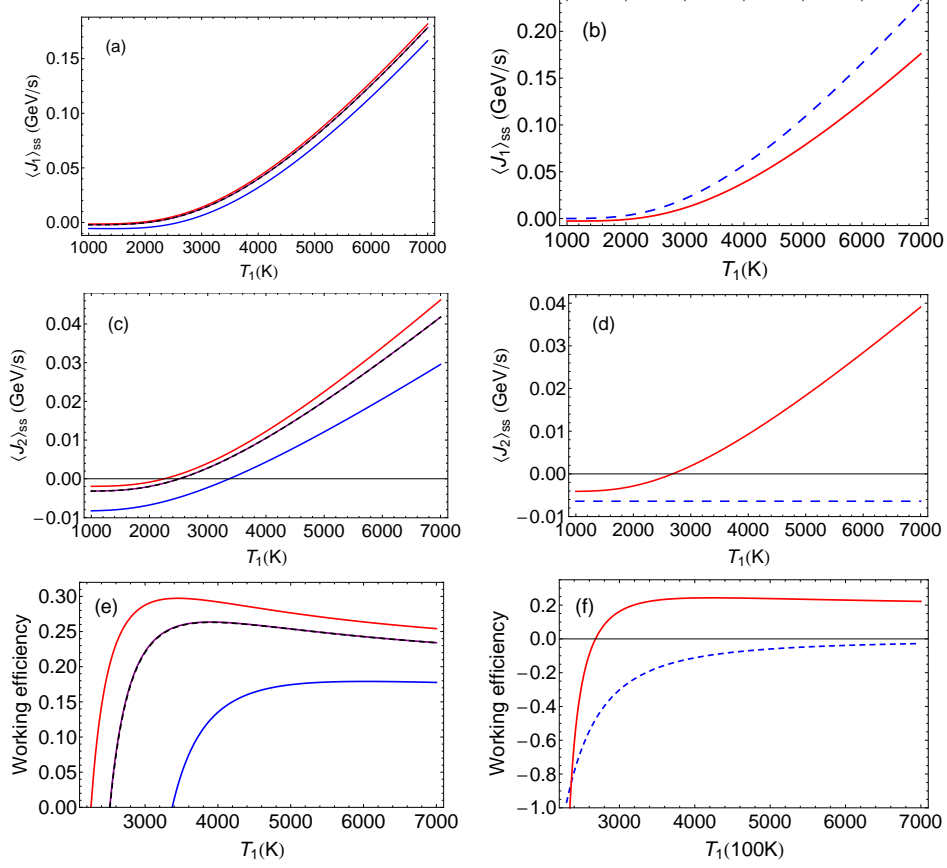


Figure 2.13: (Color online) (a,b) Energy pumping into molecules from heat source, (c,d) heat current flowing through the molecules into cool reservoir and (e,f) working efficiency vary as a function of  $T_1$ ; Blue, purple and red curves in (a,c,e) correspond to  $\delta\bar{\varepsilon} = 0.3, 0.1, 0.01\text{eV}$ , respectively, where other parameters are  $\bar{\Delta} = 0.1\text{eV}$ ,  $\bar{\varepsilon}_1 = 1\text{eV}$ ,  $T_2 = 2000\text{K}$  and  $T_3 = 1000\text{K}$ . The dashed black curve in (a,c,e) is for  $\bar{\Delta} = 0.1\text{eV}$ ,  $T_3 = 500\text{K}$  with other parameters being the same as other curves in (a,c,e); Red and blue (dashed) curves in (b,d,f) correspond to the cases without and with secular approximation, respectively, where the parameters are  $\bar{\Delta} = 0.1\text{eV}$ ,  $\delta\bar{\varepsilon} = 0.15\text{eV}$ ,  $\bar{\varepsilon}_1 = 1\text{eV}$ ,  $T_2 = 2000\text{K}$  and  $T_3 = 1000\text{K}$

functions later.

### Current-current correlation

To explore the statistical distribution of heat current, one does not only necessarily calculate the mean heat current as what we did above, but also need to uncover the higher order properties, i.e., the correlations between the currents. By replacing the summation over different modes in reservoir by the integration

$$\begin{aligned} & \sum_{\mathbf{k}, \sigma} g_{\mathbf{k}\sigma}^2 \langle b_{\mathbf{k}\sigma}^{(2)\dagger} b_{\mathbf{k}\sigma}^{(2)} \rangle e^{i(\nu - \omega_{\mathbf{k}\sigma})\Delta t} \\ & \longrightarrow \gamma \sin(\nu \Delta t) \int_0^\infty \frac{\sin(\omega_{\mathbf{k}\sigma} \Delta t)}{e^{\hbar \omega_{\mathbf{k}\sigma} / kT} - 1} d\omega_{\mathbf{k}\sigma} = \frac{\pi \gamma}{2} \sin(\nu \Delta t) \left( \coth \frac{\pi \Delta t}{\beta \hbar} - \frac{\beta \hbar}{\pi \Delta t} \right) \end{aligned} \quad (2.4.4.4)$$

and after a lengthy calculation we arrive at the current-current correlation function at steady state

$$\begin{aligned} & \text{Re} \left[ \langle \tilde{J}_2(t) \tilde{J}_2(t') \rangle_{ss} \right] \\ & = \frac{\pi \gamma}{\hbar^2} \left\{ \left( E_1^2 \langle \eta_1^\dagger \eta_1 \rangle \sin^2 \theta + E_2^2 \langle \eta_2^\dagger \eta_2 \rangle \cos^2 \theta + E_1 E_2 \langle \eta_1^\dagger \eta_2 + \eta_2^\dagger \eta_1 \rangle \sin \theta \cos \theta \right) \delta(\Delta t) \right. \\ & \quad + \frac{1}{2} \left[ E_1^2 \sin(\nu_1 \Delta t) \langle 2\eta_1^\dagger \eta_1 + 1 \rangle \sin^2 \theta + E_2^2 \sin(\nu_2 \Delta t) \langle 2\eta_2^\dagger \eta_2 + 1 \rangle \cos^2 \theta \right. \\ & \quad \left. \left. + E_1 E_2 \left( \sin(\nu_1 \Delta t) + \sin(\nu_2 \Delta t) \right) \langle \eta_1^\dagger \eta_2 + \eta_2^\dagger \eta_1 \rangle \sin \theta \cos \theta \right] \left( \coth \frac{\pi \Delta t}{\beta_1 \hbar} - \frac{\beta_1 \hbar}{\pi \Delta t} \right) \right\} \end{aligned} \quad (2.4.4.5)$$

where  $\Delta t \equiv t - t'$ ,  $\beta_i \equiv \frac{1}{kT_i}$ . Eq.(2.4.4.5) roughly illustrates the beat oscillation will occur if the detuning between the frequencies of vibrations is suppressed. To demonstrate this, in Fig.2.14 we show both the cases  $\delta\bar{\varepsilon} \ll \bar{\Delta}$  and  $\delta\bar{\varepsilon} \gg \bar{\Delta}$  in current-current correlation function (apart from the cusp peak described by the  $\delta$ -function). The former one characterizing the strong vibrational coupling of molecular chain to the molecule stretching (i.e., C=O stretching) reveals the beat oscillation and subsequently a coherent regime

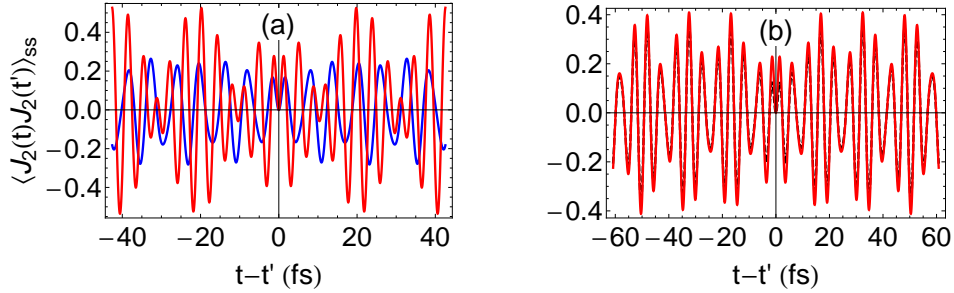


Figure 2.14: (Color online) The smooth part of current-current correlation function as a function of  $t - t'$ . Red and blue curves correspond to  $\delta\bar{\epsilon} = 0.01$  and  $0.3\text{eV}$ , respectively, where other parameters are  $\bar{\Delta} = 0.1\text{eV}$ ,  $T_1 = 4000\text{K}$ ,  $T_2 = 2000\text{K}$  and  $T_3 = 1000\text{K}$ ; The black (dashed) curve are for  $\delta\bar{\epsilon} = 0.15\text{eV}$  and  $T_1 = 2000\text{K}$ , where other parameters are the same.

of correlation, in which the correlation is strong. This is in contrast to the latter one characterizing the weak vibrational coupling of molecular chain to the molecule stretching, with an incoherent way of correlation in which the correlation is much weaker.

### 2.4.5 Coherence effect on curl flux and heat transport

In order to uncover how the entanglement of site-coherence terms to population dynamics gradually affects the nonequilibrium quantities (i.e., curl flux and heat transport), we essentially introduce an adiabatic parameter  $\epsilon$  into the coupling coefficients between coherence and populations, which originally as shown in Eq.(2.4.2.1) gives rise to the entanglement between coherence and population dynamics. The case  $\epsilon = 0$  is so-called secular approximation popularly applied to Lindblad equation before [71, 72, 73, 74],

which will be carried out as a comparison to our results with  $\epsilon = 1$ .

$$\begin{aligned}
\frac{d\rho_s}{dt} = \frac{1}{2\hbar^2} & \left\{ \sum_{\nu=1}^2 [\gamma_{\nu}^{T_{\nu,+}} (a_{\nu}\rho_s a_{\nu}^{\dagger} - a_{\nu}^{\dagger} a_{\nu}\rho_s) + \gamma_{\nu}^{T_{\nu,-}} (a_{\nu}^{\dagger}\rho_s a_{\nu} - a_{\nu} a_{\nu}^{\dagger}\rho_s)] \right. \\
& + \sum_{p=1}^2 [\gamma_p^{T_{3,+}} (a_p\rho_s a_p^{\dagger} - a_p^{\dagger} a_p\rho_s) + \gamma_p^{T_{3,-}} (a_p^{\dagger}\rho_s a_p - a_p a_p^{\dagger}\rho_s)] \\
& + \epsilon \sum_{\nu \neq p=1}^2 [\gamma_p^{T_{\nu,+}} (a_p\rho_s a_{\nu}^{\dagger} - a_{\nu}^{\dagger} a_p\rho_s) + \gamma_p^{T_{\nu,-}} (a_p^{\dagger}\rho_s a_{\nu} - a_{\nu} a_p^{\dagger}\rho_s)] \\
& \left. + \epsilon \sum_{j \neq p=1}^2 [\gamma_p^{T_{3,+}} (a_p\rho_s a_j^{\dagger} - a_j^{\dagger} a_p\rho_s) + \gamma_p^{T_{3,-}} (a_p^{\dagger}\rho_s a_j - a_j a_p^{\dagger}\rho_s)] \right\} + \text{h.c.}
\end{aligned} \tag{2.4.5.1}$$

in which the  $\epsilon$ -terms describe the behaviors of the dynamics when the coherence adiabatically comes into the system. Correspondingly the dynamical equation in the coherent representation is of the form

$$\begin{aligned}
\frac{\partial}{\partial t} P(\alpha_{\beta}, \alpha_{\beta}^*) & = \gamma \left[ 2 \left( \frac{\partial}{\partial \alpha_1} \alpha_1 + \frac{\partial}{\partial \alpha_2} \alpha_2 \right) + \epsilon \left( \frac{\partial}{\partial \alpha_1} \alpha_2 + \frac{\partial}{\partial \alpha_2} \alpha_1 \right) + \text{c.c.} \right] P(\alpha_{\beta}, \alpha_{\beta}^*) \\
& + \gamma \left[ 2Y_1^1 \frac{\partial^2}{\partial \alpha_1^* \partial \alpha_1} + 2Y_2^2 \frac{\partial^2}{\partial \alpha_2^* \partial \alpha_2} + \epsilon Y_{12}^{21} \left( \frac{\partial^2}{\partial \alpha_1^* \partial \alpha_2} + \frac{\partial^2}{\partial \alpha_1 \partial \alpha_2^*} \right) \right] P(\alpha_{\beta}, \alpha_{\beta}^*)
\end{aligned} \tag{2.4.5.2}$$

thus the drift and diffusion matrices are (in the order of  $\{1, 2, 1^*, 2^*\}$ )

$$\Sigma = \gamma \begin{pmatrix} 2 + \eta & \epsilon & 0 & 0 \\ \epsilon & 2 - \eta & 0 & 0 \\ 0 & 0 & 2 + \eta & \epsilon \\ 0 & 0 & \epsilon & 2 - \eta \end{pmatrix}, \quad D = \gamma \begin{pmatrix} 0 & 0 & Y_1^1 & \frac{\epsilon}{2} Y_{12}^{21} \\ 0 & 0 & \frac{\epsilon}{2} Y_{12}^{21} & Y_2^2 \\ Y_1^1 & \frac{\epsilon}{2} Y_{12}^{21} & 0 & 0 \\ \frac{\epsilon}{2} Y_{12}^{21} & Y_2^2 & 0 & 0 \end{pmatrix} \tag{2.4.5.3}$$

where  $\eta$  is a small and positive number, which ensures the uniqueness of the solution to Eq.(2.4.5.2). Finally we will carry out the limit  $\eta \rightarrow 0^+$ . By introducing  $f_{\pm} = \sqrt{1 + \frac{\eta^2}{\epsilon^2}} \pm \frac{\eta}{\epsilon}$ , the steady-state solution to Eq.(2.4.5.2) can

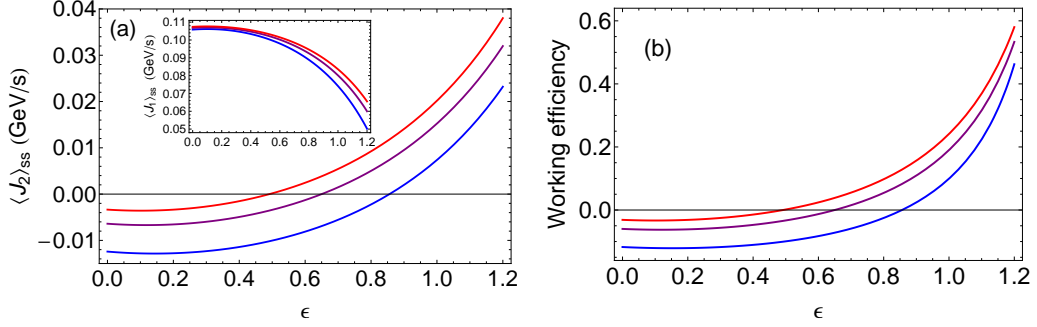


Figure 2.15: (Color online) The contribution of coherence to heat transport. (a) The heat flow pumping from the heat source (small) as well as the heat current intermediated by molecular vibrations (large), (b) working efficiency of the QHE. The blue, purple and red lines are for  $\delta\bar{\epsilon} = 0.3, 0.15$  and  $0.01\text{eV}$ , respectively. Other parameters are  $\bar{\Delta} = 0.1\text{eV}$ ,  $T_1 = 5000\text{K}$ ,  $T_2 = 2000\text{K}$ ,  $T_3 = 1000\text{K}$  and  $\eta = 0.0001$ .

be written as  $P_{ss} = \frac{\tilde{a}\tilde{b}-\tilde{c}^2}{\pi^2}\exp\{-[\tilde{a}|\alpha_1|^2 + \tilde{b}|\alpha_2|^2 + 2\tilde{c}\text{Re}(\alpha_1^*\alpha_2)]\}$  where

$$\tilde{a} = \frac{A_{11}^{24}Y_1^1 + A_{22}^{24}Y_2^2 + A_{1221}^{24}Y_{12}^{21}}{\det(B)}, \quad \tilde{b} = \frac{A_{11}^{13}Y_1^1 + A_{22}^{13}Y_2^2 + A_{1221}^{13}Y_{12}^{21}}{\det(B)},$$

$$\tilde{c} = -\frac{A_{11}^{14}Y_1^1 + A_{22}^{14}Y_2^2 + A_{1221}^{14}Y_{12}^{21}}{\det(B)} \quad (2.4.5.4)$$

$$B = \begin{pmatrix} A_{11}^{13}Y_1^1 + A_{22}^{13}Y_2^2 + A_{1221}^{13}Y_{12}^{21} & A_{11}^{14}Y_1^1 + A_{22}^{14}Y_2^2 + A_{1221}^{14}Y_{12}^{21} \\ A_{11}^{14}Y_1^1 + A_{22}^{14}Y_2^2 + A_{1221}^{14}Y_{12}^{21} & A_{11}^{24}Y_1^1 + A_{22}^{24}Y_2^2 + A_{1221}^{24}Y_{12}^{21} \end{pmatrix}$$

where the expressions of  $A_{..}$  are provided in Appendix C in Ref.[33]. Since  $\lim_{\eta \rightarrow 0} \lim_{\epsilon \rightarrow 1} f_{\pm} = 1$  and  $\lim_{\eta \rightarrow 0} \lim_{\epsilon \rightarrow 0} f_{+} = +\infty$ ,  $\lim_{\eta \rightarrow 0} \lim_{\epsilon \rightarrow 0} f_{-} = 0$ , it is straightforward to verify that Eq.(2.4.5.4) will reduce to Eq.(2.4.2.6) and  $\bar{a}$ ,  $\bar{b}$  in the forthcoming  $P_{sec}^{ss}$ , respectively. Therefore the heat currents transferred by molecular vibrations is

$$\begin{aligned}
\langle J_2 \rangle_{ss} = 2\gamma \bigg\{ & [E_1 (A_{11}^{24} \sin^2 \theta + A_{11}^{14} \sin \theta \cos \theta) + E_2 (A_{11}^{24} \cos^2 \theta - A_{11}^{14} \sin \theta \cos \theta)] Y_1^1 \\
& + [E_1 (A_{22}^{24} \sin^2 \theta + A_{22}^{14} \sin \theta \cos \theta) + E_2 (A_{22}^{24} \cos^2 \theta - A_{22}^{14} \sin \theta \cos \theta)] Y_2^2 \\
& + [E_1 (A_{1221}^{24} \sin^2 \theta + A_{1221}^{14} \sin \theta \cos \theta) + E_2 (A_{1221}^{24} \cos^2 \theta - A_{1221}^{14} \sin \theta \cos \theta)] Y_{12}^{21} \\
& - E_1 n_{\nu_1}^{T_2} \sin^2 \theta - E_2 n_{\nu_2}^{T_2} \cos^2 \theta \bigg\} \tag{2.4.5.5}
\end{aligned}$$

and the heat current pumping by the thermal fluctuations in heat source can be reached by the replacement  $\cos \theta \rightarrow \sin \theta$ ,  $\sin \theta \rightarrow -\cos \theta$  in the expression of  $J_2$ . The density-density correlation function is

$$\tilde{C}_4 = \frac{\tilde{e}^4 \sin^2 \beta}{4(1 - \tilde{e}^2) + \tilde{e}^4 \sin^2 \beta}, \quad \tilde{e} = \sqrt{\frac{2\sqrt{(\tilde{a} - \tilde{b})^2 + 4\tilde{c}^2}}{\tilde{a} + \tilde{b} + \sqrt{(\tilde{a} - \tilde{b})^2 + 4\tilde{c}^2}}} \tag{2.4.5.6}$$

Now within the secular approximation, the entanglement between coherence and populations in Eq.(2.4.5.2) dies as reflected by the disappearance of the mixed differentials with respect to  $\alpha_1, \alpha_2$ . Then the steady-state solution is simplified to  $P_{sec}^{ss}(\alpha_\beta, \alpha_\beta^*) = \frac{\tilde{a}\tilde{b}}{\pi^2} e^{-(\tilde{a}|\alpha_1|^2 + \tilde{b}|\alpha_2|^2)}$ , with  $\tilde{a} = \frac{2}{Y_1^1}$ ,  $\tilde{b} = \frac{2}{Y_2^2}$ . By reducing to the  $(x_1, x_2)$  domain, the polarization of curl flux is along the  $x_1$ -axis, since

$$\lim_{\eta \rightarrow 0} \lim_{\epsilon \rightarrow 0} \beta = 0 \Rightarrow \lim_{\eta \rightarrow 0} \lim_{\epsilon \rightarrow 0} \tilde{C}_4 = 0 \tag{2.4.5.7}$$

as firstly mentioned before. Therefore the secular approximation leads to the death of correlation between molecular vibrations (numerical verification refers to Fig.2 in Appendix C in Ref.[32]).

Eq.(2.4.5.6), Eq.(2.4.5.7), Fig.2.11(c,d) and Fig.2.11(f) illustrate the coherence effect on the curl quantum flux that the site-basis coherence causes the correlations between the molecular vibrations, which is determined by the polarization and orientation of the curl flux in coherence space, as uncovered before. Hence the shape and orientation of flux provides a quantification to the coherence contribution to nonequilibrium-related quantities.

As is shown in Fig.2.13(b,d,e), the coherence terms considerably contribute to heat current flowing through the molecules and the efficiency for the vibrational energy transport. This is because of the promotion of density-density correlation originated from the coherence quantified by the polarization and orientation of the curl flux, as illustrated in Eq.(2.4.5.6), (2.4.5.7) and Fig.2.11(c,d) and Fig.2.11(f) before. Consequently it is evident that the site-basis coherence is critical and non-trivial for the nonequilibrium behaviors on microscopic level and the quantum transport on macroscopic level. Experimentally this coherence effect can be observed by the high-resolution multidimensional laser spectroscopy, as being applied in the study of long-lived coherence in photosynthesis. On the other hand, the vibrational interfacial energy transfer can be investigated using surface-specific 2D-IR sum-frequency generation (2D-SFG) spectroscopy, by studying the effect of widely tunable excitation pulses ( $2100\text{-}3000\text{cm}^{-1}$ ) in heavy water ( $\text{D}_2\text{O}$ ) [75].

As is shown in Fig.3.1.2.9(a), the heat pumping into the molecules by the thermal fluctuations in the heat source (small figure) is suppressed while the heat transferred by the molecular vibrations (large figure) is considerably improved, as the coupling between site-coherence and population dynamics increases adiabatically. This results in the significant promotion of working efficiency, as illustrated in Fig.3.1.2.9(b). More importantly, it is noted that *the slight increase of coupling between coherence and population dynamics beyond  $\epsilon = 1$  causes a surprising improvement of efficiency to  $\geq 42\%$ , in comparison to the result in Fig.2.13(f) (blue line). This demonstrates the possibility for optimizing the quality of QHE in the regime of large interaction with coherence.* Fig.2.11(d) and 2.11(f) support the conclusion in above that the correlation between the occupations in different molecules is generated and further strengthened by the contribution of coherence, as quantified by Eq.(2.4.5.6).

## 2.4.6 Conclusion and remarks

In this section we develop a theoretical framework of curl quantum flux in continuous space, to study the microscopic nonequilibrium behaviors and the macroscopic vibrational energy transport in molecules. It was found in an analytical manner of the connection between the microscopic curl flux and the macroscopic quantum transport (i.e., correlation function) from the geometric and magnitude perspectives. By adiabatically tuning the coupling of site-coherence to the population dynamics and further comparing to the

secular approximation, the coherence is demonstrated to be essential to generate the density-density correlations and further facilitate the heat transport process by a considerable improvement. These *non-trivial* coherence effects originate from the microscopic channel, in which coherence-population entanglement results in the slender-cigar shape of curl flux polarized in the vicinity of anti-diagonal, quantified by its geometric parameters. By exploring the current-current correlation, the beat oscillation feature with strong correlation characterizes the delocalization of vibrations induced by large VP coupling, contrary to weak VP coupling where the vibrations are kept localized. Our investigation provides the possibility of probing the microscopic quantum flux in experiments and also the insights for the exploration of the nonequilibrium heat transport in more general quantum systems, i.e., the molecular chain with several vibrational modes.

# Chapter 3

## Energy transport and coherence dynamics: relaxation process I

The contents in this chapter are based on Ref.[34, 35].

### 3.1 Vibration and coherence dynamics in molecules

The relaxation processes of quantum systems recently attracted much attention, because of the experimental advances on monitoring the quantum dynamics [76, 77, 78]. The quantum dynamical behaviors cannot be completely determined by the steady-state properties, which differs from that in classical stochastic processes where the steady-state behavior governs the driving force [1, 42]. This is due to the decoherence and dephasing in dissipative quantum dynamics, which are not presented in classical case.

Studies of the relaxation of quantum systems is motivated by the idea that how to combat decoherence remains the central role on processing quantum information and computing. The details of dynamical decoherence and dephasing could provide some clues for people to figure out the way to effectively suppress or eliminate the influence from the environmental fluctuations. Usually the relaxation refers to two different scenarios: relaxing towards equilibrium and nonequilibrium steady states (NESS). The latter one is much *non-trivial* since the detailed-balance-breaking considerably promotes the amplitude of coherence, based on recent studies [31, 34]. Furthermore the

properties of NESS were much explored in recent experiments on quantum transport using the ultracold Fermi and Bose gases [79, 80, 81, 82].

One of the objectives in this chapter is to study the vibrational and coherence dynamics in intermolecular vibrational energy transport by exploring the two typical time scales  $t_1$ ,  $t_2$ . These characterize the vibrational dynamics of molecules associated with the population (longitudinal,  $t_1$ ) and phase relaxations (decoherence,  $t_2$ ). First we find that the phase relaxation is much slower than the population, namely,  $t_1 < t_2$ . This, in other words, gives rise to the coherent energy transfer, in contrast to the incoherent one predicted by Förster theory [83, 84]. Secondly the environment-induced coherence is found to considerably improve the phase-surviving time  $t_2$  and amplify the amplitude of the coherence dynamics, by comparing to the secular approximation where the coherence dynamics is decoupled to the populations [22]. This result can be further applied to the processes (including both the bosonic and fermionic cases) described by quantum master equation in general [85]. Under the secular approximation, the quantum master equation reduces to

$$\frac{\partial}{\partial t} \begin{pmatrix} \rho_p \\ \rho_c \end{pmatrix} = \begin{pmatrix} \mathcal{M}_p & 0 \\ 0 & \mathcal{M}_c \end{pmatrix} \begin{pmatrix} \rho_p \\ \rho_c \end{pmatrix} \quad (3.1.0.1)$$

which shows that the coherence has no contribution to the population dynamics and vice versa. This keeps its validity for predicting the excitation energy transfer and coherence dynamics when the system is individually coupled to environments. However, as we will show later such approximation will fail on predicting the coherence dynamics when the collective coupling between system and environment is considered. This, as will be shown later, reveals that the environmental contribution can enhance the coherence.

### 3.1.1 Vibrational energy transfer in molecules

Owing to the complexity of molecular degree of freedoms reflected by the spectroscopy, the energy can be transferred mediated by the molecular vibrations besides the electronic excitations. One of the widely-known example is the relaxation of OH-stretching of the water molecules dissolved in D<sub>2</sub>O [86, 87]. The motions of molecular vibrations can be theoretically described by several coupled quantum oscillators. To capture the key features, we model the vibrational energy transfer as two quantum-mechanically coupled oscillators. In order to realize the energy transfer, the two-oscillator system

needs to interact with two independent environments, one of which provides the excitations in molecules and the other harvests the dissipation energy. Moreover, both vibrational modes interact with the energy source which gives rise to the collective coupling to the environment. The dissipation environment only connects to one vibrational mode since in the water some of the surface OH groups couple to bulk water which is described by the harmonic oscillation bath. Therefore the free and interaction Hamiltonian of system and environments read

$$\begin{aligned}
H_0 &= \varepsilon_1 a_1^\dagger a_1 + \varepsilon_2 a_2^\dagger a_2 + \Delta(a_1^\dagger a_2 + a_2^\dagger a_1) + \sum_{\nu=1}^2 \sum_{\mathbf{k},\sigma} b_{\mathbf{k}\sigma}^{(\nu)\dagger} b_{\mathbf{k}\sigma}^{(\nu)} \\
H_{int} &= \sum_{\mathbf{k},\sigma} g_{\mathbf{k}\sigma} \left( c^\dagger b_{\mathbf{k}\sigma}^{(1)} + c b_{\mathbf{k}\sigma}^{(1)\dagger} \right) + \sum_{\mathbf{q},s} f_{\mathbf{q}s} \left( a_2^\dagger b_{\mathbf{k}\sigma}^{(2)} + a_2 b_{\mathbf{k}\sigma}^{(2)\dagger} \right)
\end{aligned} \tag{3.1.1.1}$$

where  $c \equiv a_1 + a_2$  and  $b_{\mathbf{k}\sigma}^{(1)}, b_{\mathbf{k}\sigma}^{(2)}$  are the bosonic annihilation operators of environments. The rotating-wave approximation has been applied to the vibration-bath interactions, owing to ignorance of virtual-process in long time limit. The first term in  $H_{int}$  above describes the collective coupling of vibrational modes to environment, which as shown later, leads to the strong entanglement between coherence and population dynamics. This considerably promotes both the dynamical and steady-state coherence. In realistic systems, the two vibrational modes do interact with other discrete vibrations, i.e., the stretching of OH bond in other molecules [88, 89], which in some sense, can be treated as the vibron-phonon (VP) interaction. As pointed out previously [58, 61], the strong interactions between the system and some discrete vibrational modes due to the quasi-resonance between frequencies, leads to the comparable time scales of system and these vibrational modes, which subsequently acquires us to include the dynamics of these modes together with the system. In other words, these vibrational modes must be separated from the bath degree of freedoms. They cause the renormalization of the coupling strength  $\Delta$  between the excitations in the system. The remaining modes consisting of low-energy fluctuations can then be reasonably treated as the baths, which are in weak coupling to the systems owing to the mismatch of the frequencies between these continuous modes and system.

### 3.1.2 Quantum Master Equation

Based on the perturbation theory with the rational given in last subsection, the whole solution of the density operator can be written as  $\rho_{SR} = \rho_s(t) \otimes \rho_R(0) + \rho_\delta(t)$  with the traceless term in higher orders of system-bath coupling. From the Born-Markoff approximation where the time scale associated with the environmental correlations is much smaller than that of system over which the state varies appreciably, the dynamics of the reduced density matrix of the systems can be achieved by substituting  $H_s$ ,  $H_{int}$  into Eq.(2.3.1.6) with  $H_s = \varepsilon_1 a_1^\dagger a_1 + \varepsilon_2 a_2^\dagger a_2 + \Delta(a_1^\dagger a_2 + a_2^\dagger a_1)$ . Then one has the operator master equation  $\dot{\rho}_s = \frac{i}{\hbar}[\rho_s, H_s] + \frac{1}{2\hbar^2}\mathcal{D}(\rho_s)$  and

$$\begin{aligned} \mathcal{D}(\rho_s) = & \sum_{j,p=1}^2 \left[ \gamma_p^{T_1,+} \left( a_p \rho_s a_j^\dagger - a_j^\dagger a_p \rho_s \right) + \gamma_p^{T_1,-} \left( a_p^\dagger \rho_s a_j - a_j a_p^\dagger \rho_s \right) \right] \\ & + \sum_{p=1}^2 \left[ \gamma_p^{T_2,+} \left( a_p \rho_s a_2^\dagger - a_2^\dagger a_p \rho_s \right) + \gamma_p^{T_2,-} \left( a_p^\dagger \rho_s a_2 - a_2 a_p^\dagger \rho_s \right) \right] + \text{h.c.} \end{aligned} \quad (3.1.2.1)$$

where the reservoirs are assumed to be in thermal equilibrium. The expressions of dissipation rates  $\gamma_p^{T_\nu,\pm}$  are of the form

$$\begin{aligned} \gamma_1^{T_1,+} &= \gamma \hbar^2 \left[ n_{\nu_1}^{T_1} \cos^2 \theta + n_{\nu_2}^{T_1} \sin^2 \theta + 1 + (n_{\nu_1}^{T_1} - n_{\nu_2}^{T_2}) \sin \theta \cos \theta \right] \\ \gamma_2^{T_1,+} &= \gamma \hbar^2 \left[ n_{\nu_1}^{T_1} \sin^2 \theta + n_{\nu_2}^{T_1} \cos^2 \theta + 1 + (n_{\nu_1}^{T_1} - n_{\nu_2}^{T_2}) \sin \theta \cos \theta \right] \\ \gamma_1^{T_1,-} &= \gamma \hbar^2 \left[ n_{\nu_1}^{T_1} \cos^2 \theta + n_{\nu_2}^{T_1} \sin^2 \theta + (n_{\nu_1}^{T_1} - n_{\nu_2}^{T_2}) \sin \theta \cos \theta \right] \\ \gamma_2^{T_1,-} &= \gamma \hbar^2 \left[ n_{\nu_1}^{T_1} \sin^2 \theta + n_{\nu_2}^{T_1} \cos^2 \theta + (n_{\nu_1}^{T_1} - n_{\nu_2}^{T_2}) \sin \theta \cos \theta \right] \\ \gamma_1^{T_2,+} &= \gamma \hbar^2 (n_{\nu_1}^{T_2} - n_{\nu_2}^{T_2}) \sin \theta \cos \theta, \quad \gamma_2^{T_2,+} = \gamma \hbar^2 (n_{\nu_1}^{T_2} \sin^2 \theta + n_{\nu_2}^{T_2} \cos^2 \theta + 1) \\ \gamma_1^{T_2,-} &= \gamma \hbar^2 (n_{\nu_1}^{T_2} - n_{\nu_2}^{T_2}) \sin \theta \cos \theta, \quad \gamma_2^{T_2,-} = \gamma \hbar^2 (n_{\nu_1}^{T_2} \sin^2 \theta + n_{\nu_2}^{T_2} \cos^2 \theta) \end{aligned} \quad (3.1.2.2)$$

and  $T_\nu$ 's are the temperatures of environments. The mixture angle is

$$\theta = \frac{1}{2} \tan^{-1} \left( \frac{2\Delta}{\varepsilon_1 - \varepsilon_2} \right), \quad \frac{\pi}{2} < \theta < \frac{3\pi}{4} \quad (3.1.2.3)$$

We will solve the dynamics governed by the QME in coherent representation which differs from the conventional way in Liouville space. This method

was first developed by Glauber [66]. It is alternatively named as Glauber-Sudarshan  $P$  representation in quantum optics. As is known the density matrix is expanded in terms of the eigenstates of the annihilation operators [90]

$$\rho_s(t) = \int P(\alpha_\mu, \alpha_\mu^*, t) |\alpha_1, \alpha_2\rangle \langle \alpha_1, \alpha_2| d^2\alpha_1 d^2\alpha_2 \quad (3.1.2.4)$$

where  $\hat{a}_j|\alpha_1, \alpha_2\rangle = \alpha_j|\alpha_1, \alpha_2\rangle$  and  $P(\alpha_\mu, \alpha_\mu^*, t)$  is called quasi-probability, due to the overcompleteness of the coherent basis. By projecting into the coherent representation, the QME is in the form of PDE

$$\begin{aligned} \frac{\partial}{\partial t} P(\alpha_\mu, \alpha_\mu^*, t) = & \left[ (i\omega_1 + \gamma) \frac{\partial}{\partial \alpha_1} \alpha_1 + (i\omega_2 + 2\gamma) \frac{\partial}{\partial \alpha_2} \alpha_2 + (iu + \epsilon\gamma) \times \right. \\ & \left. \left( \frac{\partial}{\partial \alpha_1} \alpha_2 + \frac{\partial}{\partial \alpha_2} \alpha_1 \right) + \text{c.c.} \right] P(\alpha_\mu, \alpha_\mu^*, t) + \gamma \left[ 2Y_1^1 \frac{\partial^2}{\partial \alpha_1^* \partial \alpha_1} + 2Y_2^2 \frac{\partial^2}{\partial \alpha_2^* \partial \alpha_2} \right. \\ & \left. + \epsilon Y_{12}^{21} \left( \frac{\partial^2}{\partial \alpha_1^* \alpha_2} + \frac{\partial^2}{\partial \alpha_1 \partial \alpha_2^*} \right) \right] P(\alpha_\mu, \alpha_\mu^*, t) \end{aligned} \quad (3.1.2.5)$$

with  $\omega_j = \varepsilon_j/\hbar$ ,  $u = \Delta/\hbar$ .  $\gamma = \pi D(\bar{\nu})g_{\bar{\nu}}^2/\hbar^2$  and  $D(\varepsilon)$  is the density of states (DOS) which is a smooth function. The coupling between the coherence and population dynamics is governed by the adiabatic parameter  $\epsilon$ , whose importance will be uncovered later. To solve the dynamical equation Eq.(3.1.2.5) we adopt the approach illustrated in the literature for Ornstein-Uhlenbeck process [42] and then write down the drift as well as diffusion matrices

$$\Sigma = \begin{pmatrix} \Gamma & 0 \\ 0 & \Gamma^\dagger \end{pmatrix}, \quad D = \gamma \begin{pmatrix} 0 & M \\ M & 0 \end{pmatrix} \quad (3.1.2.6)$$

where

$$\Gamma = \begin{pmatrix} i\omega_1 + \gamma & iu + \epsilon\gamma \\ iu + \epsilon\gamma & i\omega_2 + 2\gamma \end{pmatrix}, \quad M = \begin{pmatrix} Y_1^1 & \frac{\epsilon}{2} Y_{12}^{21} \\ \frac{\epsilon}{2} Y_{12}^{21} & Y_2^2 \end{pmatrix} \quad (3.1.2.7)$$

To solve the PDE in Eq.(3.1.2.5) above, we need to get the eigenvalues and biorthogonal eigenvectors of the drift matrix, which will be shown in detail in Supporting Information (SI) in Ref.[34]. Here two quantities  $F$  and  $G$  are

introduced

$$F = \sqrt{\frac{1}{2} \left[ 1 + 4\epsilon - 4d^2 - w^2 + \sqrt{(1 + 4\epsilon - 4d^2 - w^2)^2 + 4(w - 4\epsilon d)^2} \right]}$$

$$G = \frac{4\epsilon d - w}{F}, \quad F^2 + G^2 = \sqrt{(1 + 4\epsilon - 4d^2 - w^2)^2 + 4(w - 4\epsilon d)^2}$$
(3.1.2.8)

where  $p_{\pm} = 1 \pm F$ ,  $q_{\pm} = G \mp w$ ,  $d = \frac{\Delta}{\hbar\gamma}$  and  $w = \frac{\omega_1 - \omega_2}{\gamma}$ . Initially the system is properly assumed to stay at the ground state  $\rho_0 = |0, 0\rangle\langle 0, 0|$ , since there is no excitation at the beginning. To solve the PDE above, one needs to obtain the Glauber representation of the initial state  $\rho_0$ . First we get the matrix element  $\langle -\alpha_1, -\alpha_2 | \rho_0 | \alpha_1, \alpha_2 \rangle = e^{-(|\alpha_1|^2 + |\alpha_2|^2)}$ , which leads to the Glauber representation of the initial state based on the Fourier transform in the complex domain

$$P(\alpha_{\mu}, \alpha_{\mu}^*, 0) = \frac{e^{|\alpha_1|^2 + |\alpha_2|^2}}{\pi^4} \int \int d^2\beta_1 d^2\beta_2 \langle -\beta_1, -\beta_2 | \rho_0 | \beta_1, \beta_2 \rangle$$

$$\times e^{|\beta_1|^2 + |\beta_2|^2} e^{2i\text{Im}(\beta_1^* \alpha_1 + \beta_2^* \alpha_2)} = \delta^{(2)}(\alpha_1) \delta^{(2)}(\alpha_2)$$
(3.1.2.9)

Notice that the measure we used is  $d^2\alpha = d(\text{Re}\alpha)d(\text{Im}\alpha)$ . Therefore under the initial condition (3.1.2.9), the full solution to the dynamical equation Eq.(3.1.2.5) is  $P(\alpha_{\mu}, \alpha_{\mu}^*, t) = \frac{a(t)b(t) - |c(t)|^2}{\pi^2} \exp\{-[a(t)|\alpha_1|^2 + b(t)|\alpha_2|^2 + c(t)\alpha_1^* \alpha_2 + c^*(t)\alpha_1 \alpha_2^*]\}$  and

$$a(t) = \frac{A_{11}^{24} Y_1^1 + A_{22}^{24} Y_2^2 + A_{1221}^{24} Y_{12}^{21}}{\det(B)}$$

$$b(t) = \frac{A_{11}^{13} Y_1^1 + A_{22}^{13} Y_2^2 + A_{1221}^{13} Y_{12}^{21}}{\det(B)}$$

$$c(t) = -\frac{A_{11}^{14} Y_1^1 + A_{22}^{14} Y_2^2 + A_{1221}^{14} Y_{12}^{21}}{\det(B)}$$
(3.1.2.10)

The coefficients  $A_{\dots}$  are given in SI in Ref.[34].

### 3.1.3 Coherence and population dynamics

Given a density matrix representing the state of the molecular vibrations, we wish to evaluate the amount of entanglement in the state, which refers to

non-local correlations between the vibrational modes of spatially separated molecules. The mixed-state entanglement entropy quantifying the degree of entanglement of mixture ensemble is still an open question, despite the fact that it is well defined for the pure state. Another measure of entanglement is the concurrence, which is computable for only two qubits. Here we choose the coherence

$$C[\rho] = \text{Tr}(\rho_s a_1^\dagger a_2) = \sum_{n_1=1}^{\infty} \sum_{n_2=1}^{\infty} \sqrt{n_1 n_2} \langle n_1 - 1, n_2 | \rho_s | n_1, n_2 - 1 \rangle \quad (3.1.3.1)$$

to quantify the entanglement between different vibrational modes, from the combination of off-diagonal elements of density matrix in Fock space. First this quantity is basis-independent while the conventional description is not. Secondly as reflected in the operator master equation Eq.(3.1.2.1) the  $C[\rho]$  introduced here interacts with the populations, which in other words, may have significant contribution to the population dynamics. In analogy with the NMR experiment, the population dynamics is governed by the polarization

$$M_z = \frac{n_1 - n_2}{n_1 + n_2} \quad (3.1.3.2)$$

or alternatively  $M_z$  can be also called population imbalance.  $n_1 = \text{Tr}(\rho_s a_1^\dagger a_1)$ ,  $n_2 = \text{Tr}(\rho_s a_2^\dagger a_2)$ . In our model, these two observables are written as

$$\begin{aligned} C[\rho] &= A_{11}^{14,*} Y_1^1 + A_{22}^{14,*} Y_2^2 + A_{1221}^{14,*} Y_{12}^{21} \\ M_z &= \frac{(A_{11}^{13} - A_{11}^{24}) Y_1^1 + (A_{22}^{13} - A_{22}^{24}) Y_2^2 + (A_{1221}^{13} - A_{1221}^{24}) Y_{12}^{21}}{(A_{11}^{13} + A_{11}^{24}) Y_1^1 + (A_{22}^{13} + A_{22}^{24}) Y_2^2 + (A_{1221}^{13} + A_{1221}^{24}) Y_{12}^{21}} \end{aligned} \quad (3.1.3.3)$$

The first column of Fig.3.8 illustrates the coherence dynamics. It is commonly shown that the coherence is generated by the environments, before the dephasing takes place. Fig.3.8(a,b) show that (i) the sharp increase of both coherence as well as population imbalance and (ii) the considerable promotion of the amplitude of both coherence as well as population imbalance contributed from the thermal fluctuations in environments. In other words, these results elucidate that the environments do not only cause the dephasing process, but can also considerably enhance the quantum coherence, especially at the beginning of the dynamics. In fact the origination of (ii) is from the improvement of steady-state coherence in far-from-equilibrium regime, as uncovered before [31, 32].

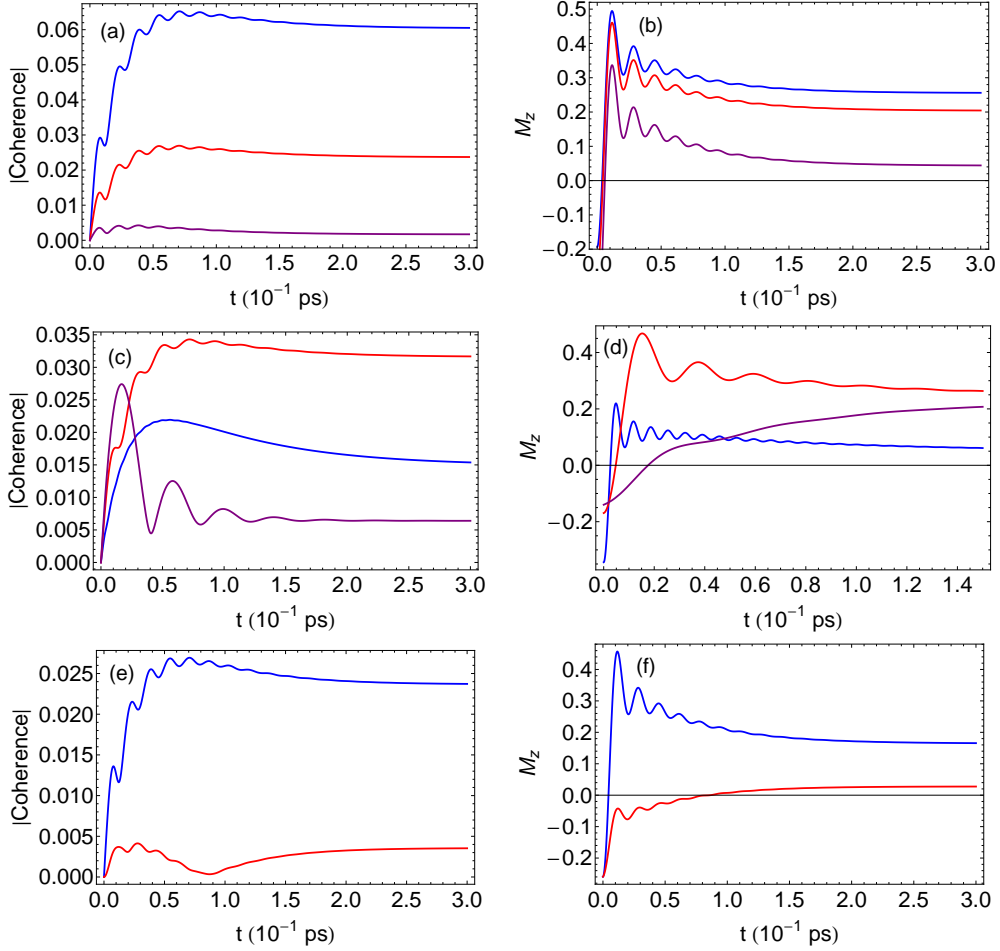


Figure 3.1: (Color online) Time evolution of coherence and magnetization (population imbalance) under various (a,b)  $T_1$  measuring the thermal fluctuations of environments, (c,d) vibron-vibron interactions and (e,f) coherence-population entanglement; In (a,b) the blue, red and purple lines are for  $T_1 = 8000\text{K}$ ,  $5600\text{K}$  and  $3500\text{K}$ , respectively.  $\Delta = 0.1\text{eV}$ ; In (c,d) the blue, red and purple lines are for  $\Delta = 0.3\text{eV}$ ,  $0.08\text{eV}$  and  $5\text{meV}$ , respectively.  $T_1 = 5600\text{K}$ ; In (e,f) the blue and red curves correspond to the cases without and with secular approximation. Other parameters are  $\delta\varepsilon = 0.15\text{eV}$ ,  $T_2 = 2100\text{K}$  and  $\gamma = 10\text{ps}^{-1}$ .

$T_1(\text{K})$	$t_1(\text{fs})$	$t_2(\text{fs})$	$t_2/t_1$
3500	36	71.6	1.98
5600	35.8	70.4	1.97
8000	35.6	80	2.25

Table 3.1: Time constants  $t_1$  and  $t_2$  with different temperatures.  $\Delta = 0.1\text{eV}$ ,  $\delta\varepsilon = 0.15\text{eV}$ ,  $T_2 = 2100\text{K}$  and  $\gamma = 10\text{ps}^{-1}$ .

It is widely known that the intramolecular relaxation process is governed by two distinct time scale  $t_1$  and  $t_2$  where  $t_1$  refers to the time constant of longitudinal relaxation or relaxation in  $z$ -direction and  $t_2$  refers to the transverse relaxation or phase relaxation. Physically  $t_1$  relaxation describes the process of re-establishing the normal Guassian distribution of populations in states in the presence of environments.  $t_2$  is the loss of phase correlation among molecules. Classically  $t_1 \geq t_2$ . In quantum systems, however as shown later,  $t_2$  can be larger than  $t_1$ , which indicates a strong coherent nature and further means that the coherence will survive during the process of energy or charge transfer. Roughly by comparing the decay tails between the two columns in Fig.3.8 it seems apparent that the relaxation of phase coherence is slower than the longitudinal relaxation. This is reflected by the tail of decay which is smooth for coherence while it is of sharp decrease for population. To quantify this issue in detail, we need to estimate the time length of relaxation by  $e^{-1}$  decay, since the behavior of time evolutions of population and coherence is of exponential feature as reflected in A<sub>1</sub> and Eq.(3.1.3.3). Both Table I and II show that the longitudinal relaxation is faster than the coherence relaxation, namely,  $t_1 < t_2$  which is contrary to the usual cases [37, 91]. On the other hand, both of longitudinal and coherence relaxations are nearly not affected by the thermal fluctuations in reservoirs while they are sensitive to the vibron-vibron interaction. This is because the  $F$ ,  $G$  defined before are independent of the bath parameters. In particular, the longitudinal relaxation becomes faster while the coherence relaxation becomes slower, as the vibron-vibron coupling increases. This originates from the vibron-phonon interaction (i.e., hydrogen bond) which leads to the renormalization of vibron-vibron couplings. Furthermore, the slower relaxation of phase coherence indicates that the dynamical energy transport process is more coherent at large vibron-vibron couplings.

By applying our model to the OH-stretching mode of HDO dissolved in

$\Delta$ (eV)	$t_1$ (fs)	$t_2$ (fs)	$t_2/t_1$
0.005	--	14.6	--
0.08	28.3	79.1	2.8
0.3	28.3	112	3.96

Table 3.2: Time constants  $t_1$  and  $t_2$  with various vibron-vibron couplings.  $\delta\varepsilon = 0.15\text{eV}$ ,  $T_1 = 5600\text{K}$ ,  $T_2 = 2100\text{K}$  and  $\gamma = 10\text{ps}^{-1}$ .

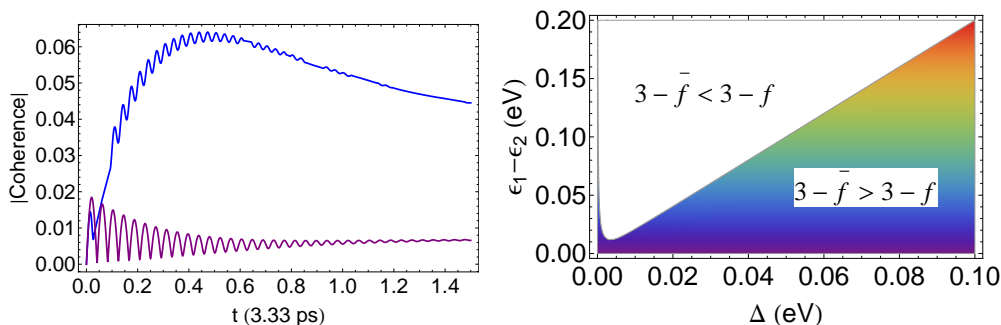


Figure 3.2: (Color online) (Left) Orientation (coherence) dynamics for the OH-stretching mode of HDO dissolved in  $\text{D}_2\text{O}$  and (right) 2D plot of  $\frac{3-F|_{\varepsilon=0}}{3-F|_{\varepsilon=1}}$  as a function of  $\Delta$  and  $\delta\varepsilon$ . (Left) The blue and purple lines correspond to  $\Delta = 0.0112\text{eV}$  and  $0.5\text{meV}$ , respectively. Other parameters are  $T_1 = 5600\text{K}$  and  $T_2 = 2100\text{K}$

$\text{D}_2\text{O}$ , the parameters are  $\varepsilon_1 = 3500\text{cm}^{-1}$ ,  $\varepsilon_2 = 3320\text{cm}^{-1}$  and  $\gamma = 0.3\text{ps}^{-1}$  according to Ref.[87]. The vibrational and orientational dynamics of OH-stretching mode of HDO molecules was measured by the femtosecond mid-infrared pump-probe study. Here, the orientational dynamics refers to the coherence dynamics in our terminology. Our theoretical investigation illustrates the coherence (orientation) dynamics in Fig.3.7(left).

The  $e^{-1}$ -decay-estimation of the time constant for coherence-surviving gives  $\tau \simeq 2.6\text{ps}$  associated with strongly hydrogen-bonded water molecules, whereas  $\tau \simeq 0.7\text{ps}$  for the weakly hydrogen-bonded water molecules. These are in good agreement (at least qualitatively, except the minor deviation caused by the simplification of theoretical model) with the measurements in recent experiments [86, 87], where the measurement of the time constants gives  $\tau \simeq 13\text{ps}$  and  $0.7\text{ps}$ , respectively.

### 3.1.4 Quantification of coherence effect

There was long debate on the coherence contribution to the vibrational and coherence dynamics, and also the energy (charge) transport. By introducing an adiabatic parameter  $\epsilon$  in Eq.(3.1.2.1) and (3.1.2.5) before, here we will study how the coherence-population entanglement gradually affects the relaxation process. Notice that the coherence-population entanglement is mainly generated by the environments. We will further perform a comparison between our full quantum dynamics ( $\epsilon = 1$ ) and the one within the secular approximation ( $\epsilon = 0$ ), in which the coherence and population dynamics are unentangled. The secular approximation has been popularly applied to the Lindblad equation describing the chemical reactions and light-harvesting complex, so that its validity should be examined hereafter. The dissipation term in Eq.(3.1.2.1) reduces to

$$\begin{aligned} \bar{\mathcal{D}}(\rho_s) = & \sum_{j=1}^2 \left[ \gamma_j^{T_{1,+}} \left( a_j \rho_s a_j^\dagger - a_j^\dagger a_j \rho_s \right) + \gamma_j^{T_{1,-}} \left( a_j^\dagger \rho_s a_j - a_j a_j^\dagger \rho_s \right) \right] \\ & + \gamma_2^{T_{2,+}} \left( a_2 \rho_s a_2^\dagger - a_2^\dagger a_2 \rho_s \right) + \gamma_2^{T_{2,-}} \left( a_2^\dagger \rho_s a_2 - a_2 a_2^\dagger \rho_s \right) + \text{h.c.} \end{aligned} \quad (3.1.4.1)$$

which leads to the case  $\epsilon = 0$  in Eq.(3.1.2.5). Correspondingly the solution shares the same expression as Eq.(3.1.2.5) by setting  $\epsilon = 0$ . Therefore the population imbalance (magnetization) and coherence are in the same formalisms as the ones previously in Eq.(3.1.3.3), under the limit  $\epsilon \rightarrow 0^+$ . Moreover the residue coherence in long time limit even under secular approximation (shown in Fig.3.8(e)) is due to the coupling between vibrational modes (vibron-vibron interaction as mentioned before), although in the dissipation part the coherence is decoupled from population dynamics.

As is shown in Fig.3.8(e) and 3.8(f), for phase coherence we found that (i) the amplitude is considerably improved and (ii) the time constant for decay is significantly extended (see the tail of decay), by the coherence-population entanglement. Quantitative analysis gives rise to  $t_2 \simeq 81\text{fs}$  and  $37.3\text{fs}$  for including coherence-population entanglement and not, respectively. This behavior is attributed to the reduction of drift force quantified by eigenvalues of the drift matrix  $\Sigma$ , by adding the coherence. Quantitatively it is  $3 - F|_{\epsilon=1} < 3 - F|_{\epsilon=0}$  in the region  $2\Delta \geq \varepsilon_1 - \varepsilon_2$ , as estimated in the right figure in Fig.3.7. To elucidate this, we adopt the Langevin-Heisenberg theory [21] to develop the dynamical equation for the system operators  $a_\nu$  from

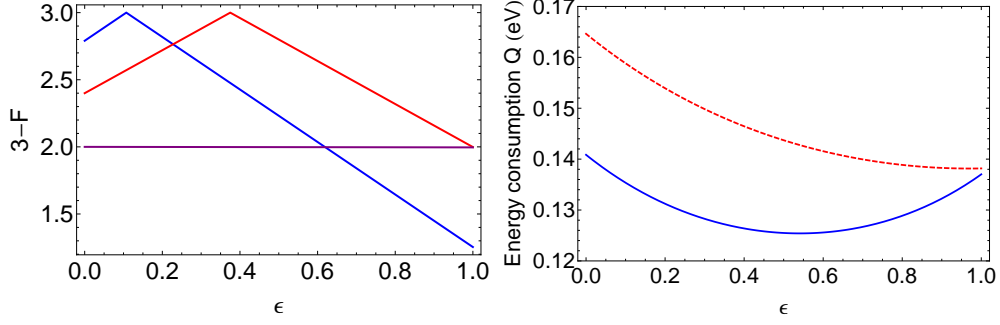


Figure 3.3: (Color online) (Left) The parameter  $3-F$  varies as a function of  $\epsilon$ . The blue, red and purple lines are for  $\Delta = 0.35\text{eV}$ ,  $0.1\text{eV}$  and  $0$ , respectively; (Right) Energy consumption as a function of  $\epsilon$ , where blue and red lines are for  $\Delta = 0.1\text{eV}$  and  $0.05\text{eV}$ , respectively. Other parameters are  $\delta\varepsilon = 0.15\text{eV}$  and  $\gamma = 10\text{ps}^{-1}$ .

$\dot{a}_\nu = \frac{1}{i\hbar}[a_\nu, H]$  and thus we have

$$\begin{aligned}
\dot{a}_1 &= -i\omega_1 a_1 - iua_2 + \frac{1}{i\hbar} \sum_{\mathbf{k},\sigma} g_{\mathbf{k}\sigma} b_{\mathbf{k}\sigma}^{(1)} \\
\dot{a}_2 &= -iua_1 - i\omega_2 a_2 + \frac{1}{i\hbar} \sum_{\mathbf{k},\sigma} \left( g_{\mathbf{k}\sigma} b_{\mathbf{k}\sigma}^{(1)} + f_{\mathbf{k}\sigma} b_{\mathbf{k}\sigma}^{(2)} \right) \\
\dot{b}_{\mathbf{k}\sigma}^{(1)} &= -i\omega_{\mathbf{k}\sigma} b_{\mathbf{k}\sigma}^{(1)} + \frac{g_{\mathbf{k}\sigma}}{i\hbar} (a_1 + a_2) \\
\dot{b}_{\mathbf{k}\sigma}^{(2)} &= -i\omega_{\mathbf{k}\sigma} b_{\mathbf{k}\sigma}^{(2)} + \frac{f_{\mathbf{k}\sigma}}{i\hbar} a_2
\end{aligned} \tag{3.1.4.2}$$

Eliminate the bath freedom by formally solving the last two equations in

Eq.(3.1.4.2) above

$$\begin{aligned} \begin{pmatrix} \dot{a}_1 \\ \dot{a}_2 \end{pmatrix} &= - \begin{pmatrix} i\omega_1 + \gamma & iu + \gamma \\ iu + \gamma & i\omega_2 + 2\gamma \end{pmatrix} \begin{pmatrix} a_1 \\ a_2 \end{pmatrix} + \begin{pmatrix} F_1(t) \\ F_2(t) \end{pmatrix} \\ F_1(t) &= \frac{1}{i\hbar} \sum_{\mathbf{k},\sigma} g_{\mathbf{k}\sigma} b_{\mathbf{k}\sigma}^{(1)}(0) e^{-i\omega_{\mathbf{k}\sigma} t} \\ F_2(t) &= \frac{1}{i\hbar} \sum_{\mathbf{k},\sigma} \left[ g_{\mathbf{k}\sigma} b_{\mathbf{k}\sigma}^{(1)}(0) + f_{\mathbf{k}\sigma} b_{\mathbf{k}\sigma}^{(2)}(0) \right] e^{-i\omega_{\mathbf{k}\sigma} t} \end{aligned} \quad (3.1.4.3)$$

which indeed is the quantum Langevin equation.  $F_j(t)$  on the right hand side of Eq.(3.1.4.3) stands for the stochastic force. As is known, the left hand side of Eq.(3.1.4.3) represents the drift force in phase space and then the right hand side recovers the drift matrix defined before as quantifying the drift force induced by the environments. Therefore, *the dephasing originates from the drift force induced by the random scattering between the system and environmental modes. The effect of environment-induced coherence-population entanglement is to reduce the drift force and the coherence subsequently survives much longer.* On the other hand, it elucidates here that the environments have *non-trivial* contribution to the long-lived coherence in the excitation energy transport, contrary to the previous statements.

To explore the gradual effect of coherence-population entanglement on the drift force and the relaxation process, we need to further study the response of quantity  $F$  to the adiabatic variation of the strength of the environment-induced coherence-population entanglement in QME. As shown in Fig.3.3, the dephasing becomes rapid in the weak  $\epsilon$  regime ( $\epsilon \ll 1$ ) while it is reduced in the strong  $\epsilon$  regime ( $\epsilon \sim 1$ ), as the coherence-population entanglement increases. Physically this indicates that the coherence can reduce the environmental diffusion only when its coupling to population dynamics becomes significant. Such behavior can be understood in general by the following

expansion of  $F$  about  $\epsilon = 0$  and 1

$$\begin{aligned}
F &= F|_{\epsilon=0} + \left(1 + \frac{1 - (2d + w)^2}{\sqrt{(1 - 4d^2 - w^2)^2 + 4w^2}}\right) \frac{\epsilon}{F|_{\epsilon=0}} + o(\epsilon^2) \\
F &= F|_{\epsilon=1} + \left(1 + \frac{5 + (6d + w)(2d - w)}{\sqrt{(5 - 4d^2 - w^2)^2 + 4(4d - w)^2}}\right) \frac{\epsilon - 1}{F|_{\epsilon=1}} \\
&\quad + o[(\epsilon - 1)^2]
\end{aligned} \tag{3.1.4.4}$$

In our regime of parameters for vibrational energy transport,  $\partial F/\partial\epsilon|_{\epsilon=0}$  is always negative while  $\partial F/\partial\epsilon|_{\epsilon=1}$  is always positive.

Before leaving this section, it is worthwhile to point out that the mechanism of the increase of lifetime of coherence is not only restricted to the molecular vibrations as discussed here, but can also be applied to the exciton process in photosynthesis [85] described by the Redfield equation [22], where the coherence-population entanglement (beyond secular approximation) led to the enhancement of coherence lifetime as well. In this sense the reduction of decoherence caused by the environmental-induced coherence-population coupling is a general feature based on the structure of quantum master equation.

### 3.1.5 Heat current

Macroscopically, the energy transfer should be affected by the quantum interference, as being much debated in the excitation energy transport in light-harvesting complex. Here we will carefully explore the contribution by the non-local correlation originated from coherence, to the heat current. The transient process, or in other words, the relaxation, demands the non-vanishing energy consumption for the molecular machine to reach the nonequilibrium steady state. The energy consumption in our model is therefore  $Q = \int_0^\infty (\langle J_1 \rangle - \langle J_2 \rangle) dt = \int_0^\infty [\langle J_1 \rangle - \langle J_1^\infty \rangle - (\langle J_2 \rangle - \langle J_2^\infty \rangle)] dt$  and

after some algebra the energy consumption reads

$$\begin{aligned}
Q &= Q_p - 4\Delta \int_0^\infty \text{Re}(\bar{C}[\rho]) dt \\
\frac{Q_p}{2} &= - \sum_{i=1}^2 (\varepsilon_1 \mathcal{I}_{ii}^{13} + \varepsilon_2 \mathcal{I}_{ii}^{24}) Y_i^i + (\varepsilon_1 \mathcal{I}_{1221}^{13} + \varepsilon_2 \mathcal{I}_{1221}^{24}) Y_{12}^{21} \\
\int_0^\infty \text{Re}(\bar{C}[\rho]) dt &= \text{Re}[\mathcal{I}_{11}^{14}] Y_1^1 + \text{Re}[\mathcal{I}_{22}^{14}] Y_2^2 + \text{Re}[\mathcal{I}_{1221}^{14}] Y_{12}^{21}
\end{aligned} \tag{3.1.5.1}$$

where  $\bar{C}[\rho] = C[\rho](t) - C[\rho](\infty)$ .  $\mathcal{I}_{\dots} = \gamma \int_0^\infty \mathcal{A}_{\dots} dt$  and their expressions will be given in SI in Ref.[34]. In general the 2<sup>nd</sup> term in Eq.(3.1.5.1) originates from the coherence, which demonstrates the non-negligible contribution from the coherence. To support this point numerically, Fig.3.3(b) shows the *non-trivial* contribution of coherence-population entanglement to the energy consumption of the QHE. Moreover the coherence leads to the overall suppression of the energy consumption which in other words, indicates that the energy transport efficiency is effectively enhanced by adding the quantum interference.

### 3.1.6 Conclusion and remarks

We have studied the dynamical energy transport mediated by the molecular vibrations. It was found that the decoherence is much slower than the population relaxation, which suggests the coherent energy transfer, contrary to the one described by Förster theory. Since the quantum interference suppresses the drift force originated from the environments, the environment-induced coherence-population entanglement leads the coherence to survive much longer than the case with population involving only. Moreover the amplitudes of both coherence and population dynamics are also considerably amplified by the coherence-population entanglement. These demonstrate the significance of the *environment-assisted* coherence effect on the vibrational relaxation process. Our theoretical exploration further provides the prediction of the time scale of orientational relaxation of OH-stretching mode, with good agreement with the experimental measurements in HDO molecules dissolved in D<sub>2</sub>O. On the macroscopic level, the coherence is shown to have *non-trivial* contribution to the enhancement of the quantum yield of vibrational energy transfer, as reflected by the suppression of the energy consumption.

## 3.2 Origin of long-lived quantum coherence and excitation dynamics in pigment-protein complexes

### 3.2.1 Breakdown of adiabatic approximation and electron-phonon interaction

In molecular aggregates, the energy transfer can be mediated by the electronic excitations, besides the vibrational modes investigated before. The wide interest in exploring this excitation energy transfer in solar cell and photosynthetic process was recently triggered by experimental investigations of excitonic dynamics in light-harvesting and Fenna-Matthews-Olson (FMO) complexes [8, 92, 93]. The transport of excitation energy in the antenna is remarkably fast and efficient, usually with quantum yields close to 100% [9], which is conjectured to correlate with the quantum nature of the aggregates. Even with the knowledge on electronic structure in antenna and the advances in spectroscopy that uncovered the long-lived quantum coherence in noisy environment [11, 94], the full understanding of the role of coherence and mechanism of excitation energy transfer has still remained mysterious.

Conventionally, either in Förster theory [83, 84] or the advanced models including dephasing [12, 15, 95, 96], the excitonic energy transfer is considered in adiabatic framework under Born-Oppenheimer approximation [97] where only the degrees of freedoms of the electrons are included. In such adiabatic regime, it has been realized that the electronic coherence has no contribution to the energy transfer in pigment-protein complexes, since the dynamics of electronic coherence and populations are unentangled. Although the models under this approximation were somehow successful in describing the population dynamics of excitons in a quasi-classical way, it shows its failure on explaining the long-lived coherence oscillations [95, 98] observed in 2D femtosecond electronic spectroscopy [13, 14, 23, 24, 25]. In fact, some discrete intramolecular vibrations are of comparable time scale of relaxation with the exciton, which subsequently leads to the breakdown of adiabatic approximation [27, 29, 30]. This in other words, reveals the deviation of equilibrium configurations on the energy surface of excitons, as illustrated in Fig.3.4. Thus this phonon dynamics often has crucial effect on the energy transport when the energy quanta of vibrational modes are in resonance with the energy splitting of excitons [26, 28, 99, 100]. Here the

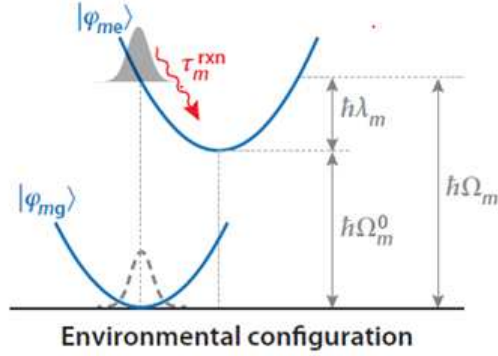


Figure 3.4: (Color online) Schematic of the deviation of equilibrium of energy surface of excitons, caused by the intramolecular vibrations. The excitonic wave packet relaxes to the new equilibrium position after the electronic excitation. This results in the breakdown of Condon approximation.

non-adiabaticity explicitly refers to the case including the phonon dynamics owing to the comparable relaxation of phonons with the excitons. Quantitatively, the deviation of the equilibrium positions of exciton energy surface is reflected by the defect of the lattice formed by nuclei in molecules. This subsequently results in the displacement of equilibrium positions of the electron potential energy  $V(\mathbf{r}) \equiv V(\mathbf{r} - \mathbf{R}_1, \mathbf{r} - \mathbf{R}_2, \dots, \mathbf{r} - \mathbf{R}_N)$  and  $V(\mathbf{r}) \rightarrow V(\mathbf{r} + \mathbf{s}) = V(\mathbf{r} - \mathbf{R}_1 - \mathbf{s}_1, \mathbf{r} - \mathbf{R}_2 - \mathbf{s}_2, \dots, \mathbf{r} - \mathbf{R}_N - \mathbf{s}_N)$  where the vectors  $\mathbf{R}_i$  and  $\mathbf{s}_i$  represents the original equilibrium positions and displacement from original equilibrium positions, respectively. Assuming  $\mathbf{s}$  is small, one can expand the electron potential in powers of deviations and break off after the linear term

$$V(\mathbf{r} + \mathbf{s}) = V(\mathbf{r}) - \sum_{i=1}^N \mathbf{s}_i \cdot \nabla_i V \quad (3.2.1.1)$$

$$\nabla_i V \equiv \frac{\partial}{\partial(\mathbf{r} - \mathbf{R}_i)} V(\mathbf{r} - \mathbf{R}_1 - \mathbf{s}_1, \mathbf{r} - \mathbf{R}_2 - \mathbf{s}_2, \dots, \mathbf{r} - \mathbf{R}_N - \mathbf{s}_N)$$

The 2nd term is the exciton-phonon interaction which quantifies the coupling between exciton and molecular vibrational motions. The displacement

can be written in terms of the normal coordinates of vibrational modes

$$\mathbf{s}_i = - \sum_{\mathbf{k}, \sigma} Q_{\mathbf{k}\sigma}^{(i)} \mathbf{e}_{\mathbf{k}\sigma} \left( a_{\mathbf{k}\sigma} + a_{-\mathbf{k}, \sigma}^\dagger \right) \quad (3.2.1.2)$$

and the electron potential is of the form

$$V(\mathbf{r} + \mathbf{s}) = V(\mathbf{r}) + \sum_{i=1}^N \sum_{\mathbf{k}, \sigma} Q_{\mathbf{k}\sigma}^{(i)} (\mathbf{e}_{\mathbf{k}\sigma} \cdot \nabla_i V) (a_{\mathbf{k}\sigma} + a_{-\mathbf{k}, \sigma}^\dagger) \quad (3.2.1.3)$$

where  $a_{\mathbf{k}\sigma}$  is the annihilation operator of phonons associated with wave vector  $\mathbf{k}$  and polarization  $\sigma$ .  $Q_{\mathbf{k}\sigma}^{(i)}$  and  $\mathbf{e}_{\mathbf{k}\sigma}$  are the amplitude of the normal coordinate with  $(\mathbf{k}, \sigma)$  and unit vector of polarization, respectively.  $Q_{\mathbf{k}\sigma}^{(i)*} = Q_{-\mathbf{k}, \sigma}^{(i)}$  is to ensure the reality of the displacement  $\mathbf{s}_i$ . From the second quantization formalism, the Hamiltonian of excitons and vibrational modes (phonons) takes the form of

$$H = \int \psi^\dagger \left[ \frac{\mathbf{p}^2}{2m} + V(\mathbf{r} + \mathbf{s}) \right] \psi \, d^3\mathbf{r} + \sum_{\mathbf{k}, \sigma} \hbar\omega_{\mathbf{k}\sigma} a_{\mathbf{k}\sigma}^\dagger a_{\mathbf{k}\sigma} \quad (3.2.1.4)$$

By expanding the field operator in terms of single electron orbitals  $\psi(\mathbf{r}) = \sum_n c_n \phi_n(\mathbf{r})$  and using Eq.(3.2.1.3) we obtain the expression of Hamiltonian governing electron-phonon interaction

$$H = \sum_{n=1}^N \varepsilon_n c_n^\dagger c_n + \sum_{\mathbf{k}, \sigma} \hbar\omega_{\mathbf{k}\sigma} a_{\mathbf{k}\sigma}^\dagger a_{\mathbf{k}\sigma} + \sum_{n, m=1}^N \sum_{\mathbf{k}, \sigma} M_{nm}^{\mathbf{k}\sigma} c_n^\dagger c_m (a_{\mathbf{k}\sigma} + a_{-\mathbf{k}, \sigma}^\dagger) \quad (3.2.1.5)$$

$$M_{nm}^{\mathbf{k}\sigma} = \sum_{i=1}^N Q_{\mathbf{k}\sigma}^{(i)} \mathbf{e}_{\mathbf{k}\sigma} \cdot \langle \phi_n | \nabla_i V | \phi_m \rangle \quad (3.2.1.5)$$

where  $c_n$  is the fermionic annihilation operator of electrons and  $\varepsilon_n$  is the energy of the  $n$ -th level of single electron which satisfies the eigenequation

$$\left[ \frac{\mathbf{p}^2}{2m} + V(\mathbf{r}) \right] |\phi_n\rangle = \varepsilon_n |\phi_n\rangle \quad (3.2.1.6)$$

### 3.2.2 Organization of the section

In this section, we develop an effective theory to uncover in a general scenario the underlying mechanism for long-lived quantum coherence, while other investigations *numerically* show the existence of such effect without illustrating the mechanism [27, 99]. The bare electron is surrounded by discrete

vibrational modes. As a result, the new composite called polaron emerges, resulting in the suppression of system-reservoir coupling and therefore the screening of the exciton-bath interaction. This leads to much longer survival of quantum coherence than that with bare excitons only. Our general theory, on the other hand, suggests a physical mechanism for slowing down the dynamical decoherence, which is potentially applicable in quantum computation. Our motivation is to understand the role of vibrational coherence on the long-lived coherence and also the efficient energy transfer measured in recent experiments [13, 14, 23]. Our general effective theory is verified in the pigment-protein complex by uncovering the long-lived electronic and excitonic coherences caused by vibrational coherence. Moreover such a system the ground-state coherence contributed by incoherent environment is found to give rise to the considerable enhancement of excitation energy transfer. This, however, fails to be predicted by the previous model without incoherent radiations.

### 3.2.3 Model and Hamiltonian

For the general consideration of the coupling of molecular excitations to the motions of molecular vibrations, we introduce the  $N$ -site fermionic system coupled to the phonons. From the electron-phonon interaction introduced in Eq.(3.2.1.5) the subsequent Hamiltonian is

$$\begin{aligned}
H = & \sum_{n=1}^N \varepsilon_n a_n^\dagger a_n + \sum_{n < m} J_{nm} (a_n^\dagger a_m + a_m^\dagger a_n) + \sum_{\mathbf{q},s} \hbar \omega_{\mathbf{q}s} b_{\mathbf{q}s}^\dagger b_{\mathbf{q}s} \\
& + \sum_{\mathbf{q},s} \sum_{n=1}^N f_{\mathbf{q}s} \hbar \omega_{\mathbf{q}s} \gamma_n a_n^\dagger a_n (b_{\mathbf{q}s} + b_{-\mathbf{q},s}^\dagger)
\end{aligned} \tag{3.2.3.1}$$

where  $\varepsilon_n$  and  $J_{nm}$  are the on-site energy and electronic coupling of excitons, respectively. In the last term  $f_{\mathbf{q}s}$  governs the strength of electron-phonon interaction and  $\gamma_n$  quantifies the diagonal disorder of the system, leading to the renormalization of the on-site energies as shown later.  $\omega_{\mathbf{q}s}$  stands for the dispersion relation of phonons as a function of wave vector  $\mathbf{q}$  and  $s$  denotes the phonon polarization.  $a_n$  and  $b_{\mathbf{q}s}$  are the fermionic and bosonic annihilation operators of excitons and phonons, respectively. To take into account the effect of discrete vibrational modes, we need to reach the effective theory, by applying the polaron transform to the entire system with the generating

function

$$S = \sum_{m=1}^N \sum_{\mathbf{q},s} f_{\mathbf{q}s} \gamma_m a_m^\dagger a_m (b_{-\mathbf{q},s}^\dagger - b_{\mathbf{q}s}) \quad (3.2.3.2)$$

Because of some phonon modes being quasi-resonance with excitonic energy gap which leads them to strongly couple to excitons, these discrete modes should be separated from others and then the remaining phonon modes weakly interact with the excitons. This results in the effective Hamiltonian  $\tilde{H} = H_S + H_{ph} + H_{int}$  and

$$\begin{aligned} H_S &= \sum_{i=1}^N (\varepsilon_i - \gamma_i^2 V_0) a_i^\dagger a_i + 2V_0 \sum_{i<j} \gamma_i \gamma_j a_i^\dagger a_j^\dagger a_i a_j \\ &\quad + \sum_n \hbar \omega_n d_n^\dagger d_n + \sum_{i<j} J_{ij} \left[ \prod_n e^{\lambda_n (\gamma_i - \gamma_j) (d_n^\dagger - d_n)} a_i^\dagger a_j + \text{h.c.} \right] \\ H_{int} &= \sum_{\mathbf{q},s} \sum_{i<j} (\gamma_i - \gamma_j) J_{ij} \prod_m e^{-\lambda_m^2 (\gamma_i - \gamma_j)^2 / 2} f_{\mathbf{q}s} \\ &\quad \times \left( a_i^\dagger a_j \prod_n \chi_{ij}^n - a_j^\dagger a_i \prod_n \chi_{ij}^{n,\dagger} \right) (b_{-\mathbf{q},s}^\dagger - b_{\mathbf{q}s}) \\ H_{ph} &= \sum'_{\mathbf{q},s} \hbar \omega_{\mathbf{q}s} b_{\mathbf{q}s}^\dagger b_{\mathbf{q}s} \end{aligned} \quad (3.2.3.3)$$

where the on-site energy of excitons is renormalized by phonons reflected by the 1<sup>st</sup> term of  $H_S$  and  $V_0 = \sum_{\mathbf{q},s} f_{\mathbf{q}s}^2 \hbar \omega_{\mathbf{q}s}$ . The 2<sup>nd</sup> and 3<sup>rd</sup> terms are the exciton-exciton interaction (intermediated by phonons) and the free Hamiltonian of discrete vibrational modes, respectively. The last term in  $H_S$  quantifies the electronic coupling renormalized by exciton-vibrational (discrete phonon modes) coupling. The exciton-phonon interaction strength  $f_{\mathbf{q}s}$  is replaced by  $\lambda_n$  where  $\lambda_n = f_{\mathbf{q}'s'}$  for those discrete modes.  $|\lambda_n \gamma_i|$  refers to the Huang-Rhys or Frank-Condon factor [101] which quantifies the overlap between the vibrational wavefunctions. The vibrational operator is  $\chi_{ij}^n = e^{\lambda_n (\gamma_i - \gamma_j) d_n^\dagger} e^{-\lambda_n (\gamma_i - \gamma_j) d_n}$ . Those discrete vibrational modes are denoted by the operator  $d_n$ 's.  $H_{int}$  above is obtained up to the 1st order of  $f_{\mathbf{q}s}$  and it describes the coupling of excitons to the remaining phonon modes, other than the discrete phonon modes. Eq.(3.2.3.3) shows that the effective coupling

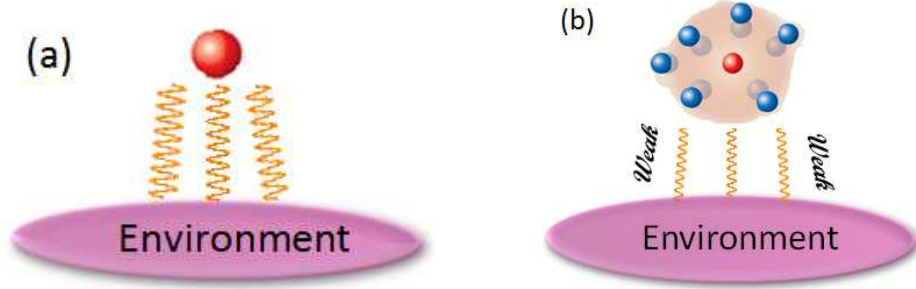


Figure 3.5: (Color online) The schematic of exciton-environment interaction. (a) The coupling between bare exciton and environment; (b) The exciton-vibration coupling forms a new composite called polaron. In (b) the bare exciton (red) is surrounded by a cloud consisting of discrete vibrational modes (blue), which leads to the suppression of the coupling strength between exciton and environment.

strength between exciton and phonon is renormalized by the polaron effect, which leads to the weak interaction of the new composite (exciton+vibron) with the environmental modes, as will be illustrated in details later.

### 3.2.4 General mechanism for long-lived quantum coherence

Based on Eq.(3.2.3.3), the discrete phonon modes are glued to excitons and the whole system forms the polarons, which weakly couple to the quasi-continuous phonon modes. This results in the renormalization of the effective coupling strength between exciton and phonon, as illustrated in Fig.3.5. Because the energy gap of excitons is in quasi-resonance with the vibrational energy, the dynamics of those vibrations can therefore be restricted to the space spanned by  $|\{m_n\}\rangle$ ,  $|\{m_n + 1\}\rangle$  where  $m_n = \langle\{m_n\}|d_n^\dagger d_n|\{m_n\}\rangle$  represents the occupation number of phonons on each vibrational mode. In most circumstance, the molecular vibrations are always excited from the ground state so that only the eigenstates  $|\{0\}\rangle$ ,  $|\{1\}\rangle$  are included. Therefore by taking into account the matrix elements of the vibrational operator  $\chi_{ij}^n$ :  $\langle\{m_n\}|\chi_{ij}^n|\{m_n\}\rangle = L_{m_n}(\lambda_n^2(\gamma_i - \gamma_j)^2)$ ,  $\langle\{m_n\}|\chi_{ij}^n|\{m_n + 1\}\rangle = -(\gamma_i - \gamma_j)\lambda_n\sqrt{m_n + 1}F_1(-m_n; 2; \lambda_n^2(\gamma_i - \gamma_j)^2)$ , which are of order  $\sim 1$  especially for the case  $m_n = 0$ , the effective coupling between system and phonon

environment is renormalized as

$$\bar{f}_{\mathbf{qs}}^{ij} = (\gamma_i - \gamma_j) \prod_n e^{-\lambda_n^2(\gamma_i - \gamma_j)^2/2} f_{\mathbf{qs}} \quad (3.2.4.1)$$

which shows that the system-bath interaction is suppressed by a factor of  $\prod_m e^{-\lambda_m^2(\gamma_i - \gamma_j)^2/2}$ . In the framework of weak system-reservoir interaction, the typical dephasing rate  $\Gamma$  is determined by the square of system-bath coupling, namely,  $\Gamma \sim f_{\mathbf{qs}}^2$  [22]. This leads to the reduction of the dephasing rate induced by phonon environment, namely,  $\bar{\Gamma} = (\gamma_i - \gamma_j)^2 \frac{\langle J_{ij}^2 \rangle}{\hbar^2 \langle \bar{\omega} \rangle^2} \prod_n e^{-\lambda_n^2(\gamma_i - \gamma_j)^2} \Gamma \simeq \prod_n e^{-\lambda_n^2(\gamma_i - \gamma_j)^2} \Gamma$  and then the typical lifetime of coherence is elongated

$$\frac{\bar{\tau}}{\tau} \simeq \prod_n \frac{e^{\lambda_n^2(\gamma_i - \gamma_j)^2}}{(\gamma_i - \gamma_j)^2} \quad (3.2.4.2)$$

Notice that in the matrix elements of  $\chi_{ij}^n$ ,  $L_n(z)$  is the Laguerre polynomial and  ${}_1F_1(a; b; z)$  is the Hypergeometric function of order (1,1). Eq.(3.2.4.2) demonstrates that the lifetime of coherence of the system is *exponentially* improved by the exciton-vibration coupling. In pigment-protein complexes such as FMO systems,  $|\gamma_i - \gamma_j| \sim 2$  and  $\lambda_n \sim 1$  so that  $\bar{\tau}_2 \gtrsim 10\tau_2$  if  $n = 1$ , namely, only one discrete vibrational mode is included. Furthermore it should be noticed that the amplification factor of the typical lifetime of coherence will be  $e^{\lambda^2(\gamma_i - \gamma_j)^2 M}$  when considering  $M$  discrete vibrational modes in quasi-resonance with exciton energetic gap. As a brief summary, this demonstrates the mechanism in a general scenario: some modes of molecular vibrations surrounding the exciton form the new quasiparticle called polaron which results in the screening of interaction between bare exciton and environment. Hence we suggest that the consequent weak coupling of polarons to the environment is the origin of the long-lived quantum coherence. It is also worthy to point out that based on this mechanism, *the vibrational coherence generated by vibrational modes will play a significant role in understanding the long-lived excitonic coherence.*

### 3.2.5 Pigment-protein Complex

As an example for elucidating the general mechanism proposed in the last section, we will study in detail the coherence dynamics of the pigment-protein complex, as illustrated in Fig.3.6. By considering a prototype dimer strongly

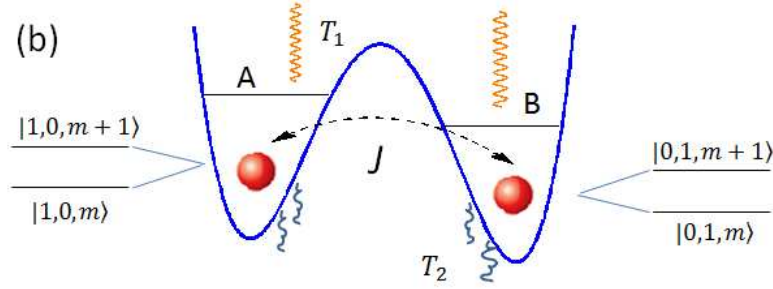


Figure 3.6: Schematic of a dimer in pigment-protein complex. The excitons in pigments couple to a vibrational mode and the radiation energy with temperature  $T_1$  is absorbed by such joint system and then dissipated into the noisy protein environment with temperature  $T_2$ .

coupled to intramolecular vibration of frequency  $\omega$ , the interaction between exciton and vibrational modes reads

$$H_{ex-vib}^{pp} = (\eta\hbar\omega/2^{1/2}) (|A\rangle\langle A| - |B\rangle\langle B|) (d_- + d_-^\dagger) \quad (3.2.5.1)$$

for the non-adiabatic treatment and total Hamiltonian is  $H_S^{pp} = H_0^{pp} + H_{vib} + H_{ex-vib}^{pp}$ , where  $H_0^{pp} = \varepsilon_A|A\rangle\langle A| + \varepsilon_B|B\rangle\langle B| + J(|A\rangle\langle B| + |B\rangle\langle A|)$  and  $H_{vib} = \hbar\omega d_-^\dagger d_-$ .  $|A\rangle$  and  $|B\rangle$  denote the electronic states of pigments  $A$  and  $B$ , respectively. The minus sign in Eq.(3.2.5.1) is due to the relative motion between the vibrational modes [61].  $\eta$  is the Franck-Condon factor of the vibrations. The energy gap between the localized excitons is  $\Delta = \varepsilon_A - \varepsilon_B > 0$ .

In pigment-protein complexes, the excitons interact with both the incoherent radiations and the low-frequency fluctuations of protein (phonons), to funnel the unidirectional energy transfer. The interaction with radiations takes the dipolar form of  $\mathbf{p} \cdot \mathbf{A}$  in *quantum electrodynamics*, where  $\mathbf{p}$  and  $\mathbf{A}$  are the exciton momentum and vector potential, respectively. The interaction then reads

$$H_{int}^{pp} = \sum_{n=1}^2 \sum_{m=2,4} \sum_{\mathbf{k},p} g_{\mathbf{k}p} (\sigma_{n,n+m}^- + \sigma_{n,n+m}^+) (a_{\mathbf{k}p} + a_{-\mathbf{k},p}^\dagger) + \sum_{n=3}^6 \sum_{\mathbf{q},s} f_{\mathbf{q}s} \gamma_n \sigma_{nn} (b_{\mathbf{q}s} + b_{-\mathbf{q},s}^\dagger) \quad (3.2.5.2)$$

where  $\sigma_{ij}^- = |i\rangle\langle j|$ ,  $\sigma_{ji}^+ = |j\rangle\langle i|$  ( $i < j$ ) are the lowering and raising operators

of excitons, and  $\sigma_{ii} = |i\rangle\langle i|$ .  $a_{\mathbf{k}p}$  and  $b_{\mathbf{q}s}$  are the bosonic annihilation operators of the radiation and low-frequency fluctuation environments, respectively. The free Hamiltonian of the reservoirs is  $H_{bath} = \sum_{\mathbf{k},p} \hbar\nu_{\mathbf{k}p} a_{\mathbf{k}p}^\dagger a_{\mathbf{k}p} + \sum_{\mathbf{q},s} \hbar\omega_{\mathbf{q}s} b_{\mathbf{q}s}^\dagger b_{\mathbf{q}s}$ . Usually the low-frequency fluctuations are effectively described by the Debye spectral density  $S(\omega) = (2E_R/\pi\hbar)(\omega\omega_d/(\omega^2 + \omega_d^2))$  where  $E_R$  is the so-called reorganization energy and it governs the coupling strength between system and low-energy fluctuations.  $\omega_d$  refers to the Debye cut-off frequency. Owing to fast relaxation of the environments and weak system-bath interaction as pointed out in our model, the quantum master equation (QME) for the reduced density matrix of the systems can be derived by tracing out the degree of freedoms of the environments. In Liouville space the QME can be further formulated as two-component form

$$\frac{\partial}{\partial t} \begin{pmatrix} \rho_p \\ \rho_c \end{pmatrix} = \begin{pmatrix} \mathcal{L}_p & \mathcal{L}_{pc} \\ \mathcal{L}_{cp} & \mathcal{L}_c \end{pmatrix} \begin{pmatrix} \rho_p \\ \rho_c \end{pmatrix} \quad (3.2.5.3)$$

where  $\rho_p$  and  $\rho_c$  represent the population and coherence components of the density matrix, respectively.  $\mathcal{L}_{pc}$  and  $\mathcal{L}_{cp}$  quantify the *non-trivial* entanglement between the dynamics of population and electronic coherence, beyond the secular approximation. Their forms can be directly obtained from Eq.(S20) in Supporting Information (SI) in Ref.[35] and the details are omitted here to avoid redundancy.

### 3.2.6 Coherence dynamics and excitation energy transfer

As is known, the excitation energy transfer is reflected by the transient behavior of the population on pigment  $B$ . This is quantified by the scaled probability

$$\bar{P}_B(t) = \frac{\sum_{\nu=m}^{m+1} \langle B, \nu | \rho | B, \nu \rangle}{\sum_{i=A,B} \sum_{\nu=m}^{m+1} \langle i, \nu | \rho | i, \nu \rangle} \quad (3.2.6.1)$$

To clarify the contribution of quantum coherence, we denote the coherence in the *localized basis* into two groups: electronic and vibronic coherences. The

former and latter ones are defined as

$$C_{ele} = \text{Im}\langle A, m | \rho | B, m \rangle + \text{Im}\langle A, m + 1 | \rho | B, m + 1 \rangle$$

$$C_{vib}^{(i)} = \text{Im}\langle i, m | \rho | i, m + 1 \rangle; \quad i = A, B \quad (3.2.6.2)$$

Moreover the ground-state coherence takes the form of  $C_{gs} = \text{Im}\langle 0, m | \rho | 0, m + 1 \rangle$ . As will be shown later, these vibronic coherences will dramatically affect the behaviors of energy transfer and decoherence process. In our calculations, the vibrational mode is assumed to be excited at ground state, namely,  $m = 0$ .

### Long-lived coherence

To explore the effect of molecular vibrations on the decoherence process, we will study the coherence dynamics, for both the cases including exciton-vibrational coupling (non-adiabatic regime) or not (adiabatic regime). Fig.3.7(a) shows the dynamical behavior of the electronic coherences in both the adiabatic (purple) and non-adiabatic (blue) regimes. Obviously the non-adiabatic framework makes the electronic wavepacket  $C_{ele}$  become long-lived in oscillation, comparing to the case in adiabatic regime. Quantitatively, the time constant of beating of the electronic wave packet with exciton-vibron coupling is  $\tau_{na} \sim 0.024t_0$  while it is  $\tau_a \sim 0.005t_0$  without exciton-vibron coupling. Taking FMO complex as example  $\Delta \simeq 150\text{cm}^{-1}$ ,  $\omega \simeq 200\text{cm}^{-1}$ ,  $J \simeq 66\text{cm}^{-1}$  and  $\gamma \simeq 0.1\text{ps}^{-1}$  [29, 102], thus  $\tau_{na} \sim 2.2\text{ps}$  and  $\tau_a \sim 500\text{fs}$ . This confirms the mechanism given by Eq.(3.2.4.1) and (3.2.4.2) in our model such that the weak coupling of polaron to environment by including exciton-vibrational interaction serves as the origin for the long-lived electronic coherence. The structure of QME in Eq.(3.2.5.3) reveals that the environments are forbidden to generate the direct transition between vibrational states, namely, between  $|f, 0\rangle, |f, 1\rangle$ ;  $f = A, B$ . This, in other words, will lead to the long surviving time of vibrational wave packet oscillation at excited states, as reflected in Fig.3.7(b). The ground-state vibronic coherence  $C_{gs}$  holds extremely long-lived oscillation of ground-state wave packet, compared to the vibrations of excited-state wave packet (the time scale for GS wave packet is  $\geq 0.2t_0$  while it is  $\sim 0.024t_0$  for excited-state wave packet), as shown in Fig.3.7(c). Such extremely long surviving time is attributed to the fact that there is no chance for exciton to decay when the wave packet is oscillating in the ground state.

In 2D femtosecond experiments, coherence dephasing appears as the decay of oscillations in the amplitudes of the cross peaks, which describes the

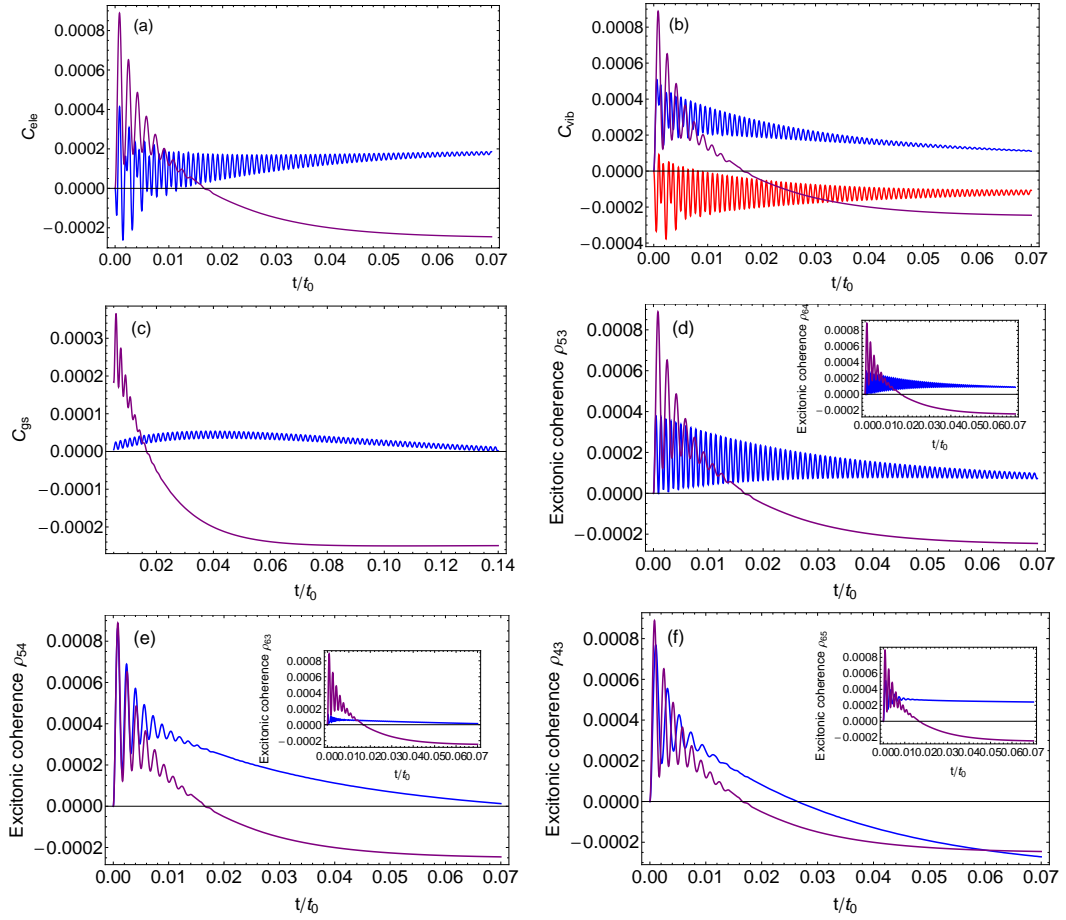


Figure 3.7: (Color online) Time evolution of (a) electronic wave packet, (b) excited-state vibrational wave packet and (c) ground-state vibrational wave packet. In (a,c), blue lines are for our model in non-adiabatic regime; In (b) the blue and red lines correspond to excited-state vibrational wave packets  $\langle A, 0 | \rho | A, 1 \rangle$  and  $\langle B, 0 | \rho | B, 1 \rangle$ , respectively. Time evolution of the *excitonic* coherence in delocalized basis, where blue lines correspond to non-adiabatic regime. Purple lines in (a,b,c) electronic and (d,e,f) excitonic coherences are for adiabatic regime, respectively. The parameters are: Frank-Condon factor  $\eta \simeq 1$ ,  $\Delta = 0.023\varepsilon_A$ , electronic coupling  $J = 0.01\varepsilon_A$ , frequency of vibrational mode  $\hbar\omega = 1.33\Delta$ ,  $k_B T_1 = 0.63\varepsilon_A$ ,  $k_B T_2 = 1.4\Delta$ , Debye frequency  $\hbar\omega_d = 0.7\Delta$ , typical decay rate  $h\gamma = 0.0005\varepsilon_A$ , reorganization energy  $E_R = 0.23\Delta$  and  $t_0 = 10\gamma^{-1}$ .

superpositions of excitonic states (localized). Thereby the position  $(\omega_\tau, \omega_t)$  of the cross-peak refers to the delocalized excitonic states rather than the localized ones. In such spirit, we should therefore investigate the *excitonic coherence* as shown in delocalized basis, in distinction from the electronic as well as vibronic coherences in localized basis before. From Fig.3.7(d) we can see that the oscillation of the excitonic coherence is long-lived with the surviving time  $\bar{\tau}_{na} \sim 0.024t_0$  being at least  $\sim 5$  times than  $\bar{\tau}_a \sim 0.005t_0$  in adiabatic regime, because of the long-lived oscillations of vibrational and electronic wave packets as shown in Fig.3.7(a) and 3.7(b). This numerical evaluation of the lifetime of excitonic coherence illustrates the validity of the mechanism of long-lived coherence shown in Eq.(3.2.4.1) and (3.2.4.2), as suggested by our model. For FMO complex from green sulfur bacteria,  $\bar{\tau}_{na} \sim 2.4\text{ps}$  and  $\bar{\tau}_a \sim 500\text{fs}$ , which are almost identical to the measurements in recent experiments [13, 14, 23]. This consequently leads excitation energy transfer on the paths  $(|A, 0\rangle; |B, 0\rangle)$  and  $(|A, 1\rangle; |B, 1\rangle)$  to be coherent while on the other paths it is still incoherent, due to the short-lived oscillation of wave packet between other states, as shown in Fig.3.7(e) and 3.7(f).

### Population dynamics and energy transfer

To uncover the effect of incoherent radiations on energy transfer, we need to study the time evolution of population on pigment  $B$ , for both adiabatic and non-adiabatic regimes, as shown in Fig.3.8, where the incoherent radiations are included in 3.8(a) but not in 3.8(b). The initial conditions are: (a)  $\rho(0) = |0, 0\rangle\langle 0, 0|$  for blue and  $\rho(0) = |0\rangle\langle 0|$  for purple; (b)  $\rho(0) = |A, 0\rangle\langle A, 0|$  for blue and  $\rho(0) = |A\rangle\langle A|$  for purple. By comparing Fig.3.8(a) and 3.8(b), one can conclude that the vibrational coherence, especially ground-state vibrational coherence facilitates the excitation energy transport by including the incoherent radiations (blue line is higher than purple in Fig.3.8(a)). Otherwise, it is unable to promote the energy transfer process (blue line is lower than purple in Fig.3.8(b)). In particular, the excitation energy transfer to pigment  $B$  is considerably promoted by the ground-state vibrational coherence while including the incoherent environment (in Fig.3.8(a) blue line is of

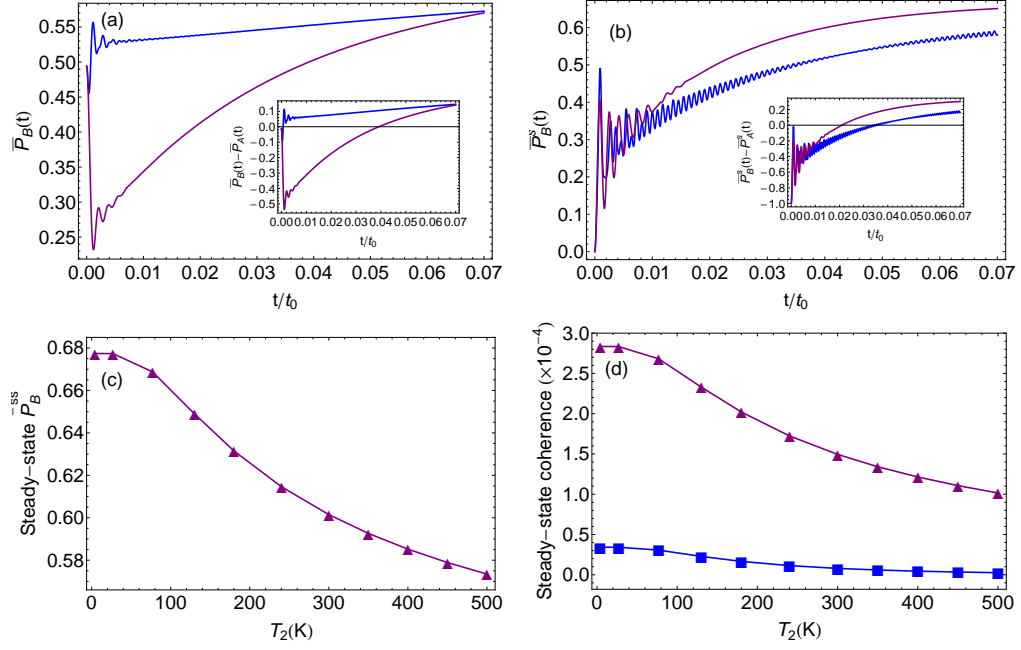


Figure 3.8: (Color online) The dynamics of scaled population on pigment  $B$  for (a) including and (b) NOT including the incoherent radiation environment. In both (a,b), the blue and purple curves correspond to the non-adiabatic and adiabatic regimes, respectively. (c) Steady-state population on pigment  $B$  with respect to the temperature of low-frequency fluctuations; (d) Steady-state quantum coherence varies as a function of the temperature of low-frequency fluctuations. In (d) the purple and blue lines are for electronic (localized) and excitonic (delocalized) coherences, respectively. The parameters are the same as in Fig.3.7.

much larger value than purple line), due to the nonvanishing coefficients

$$\begin{aligned}\mathcal{L}_{ii,12} &= \sum_{\nu=3}^6 \gamma n_{\omega_{2\nu}}^{T_1} (U_{4\nu} + U_{6\nu}) U_{\nu i}^T \\ \mathcal{L}_{jj,12} &= \sum_{\nu=3}^6 \gamma n_{\omega_{1\nu}}^{T_1} (U_{3\nu} + U_{5\nu}) U_{\nu j}^T, \quad i = 3, 5; j = 4, 6\end{aligned}\quad (3.2.6.3)$$

in Eq.(S20) in SI in Ref.[35]. This physically indicates that the excitation energy transfer is entangled with the ground-state vibrational coherence by absorbing photons from incoherent radiations. In contrast, the excited-state vibrational coherences themselves are unable to enhance the excitation energy transfer from pigment  $A$  to  $B$  as shown in Fig.3.8(b), if only the low-energy noise by protein is included. This is because of the fact that the dynamics of populations is decoupled to that of vibrational coherence, namely,  $\mathcal{L}_{nn,n\pm 1n} = 0$  based on the analysis of the structure of QME in Eq.(3.2.5.3) and (S20)(SI in Ref.[35]). Furthermore, Fig.3.8(a) shows that the cumulative population on pigment  $B$ :  $\int \bar{P}_B dt$  is much larger than the one without including exciton-vibrational coupling. This means that the total energy transport is much enhanced by the vibrational coherence, when including the radiations. This promotion of energy transport, in fact, is natural from the view of point of nonequilibriumness, which will be illustrated later.

Moreover, because the lifetime of the enhancement of excitation energy transfer is *almost* identical to the surviving time of the excitonic coherence oscillation as shown in Fig.3.7(d) and 3.8(a), our results lead to the conclusion that the optimization of the energy transfer is always assisted by the wave-like behavior of coherence, *when the time-reversibility is broken at steady state*. This is consistent with the measurements in ultrafast spectroscopy where the coherent wave-like motion of excitations was conjectured to facilitate the excitonic energy transfer.

### 3.2.7 Nonequilibriumness, steady-state coherence and energy transfer

It is important to note that the nonvanishing steady-state coherence is reached for both of the localized and delocalized cases, as shown in Fig.3.7. To elucidate this in detail, we explore the nonequilibrium effect (induced by two heat sources, one is from radiations and the other is from phonons) on steady-state

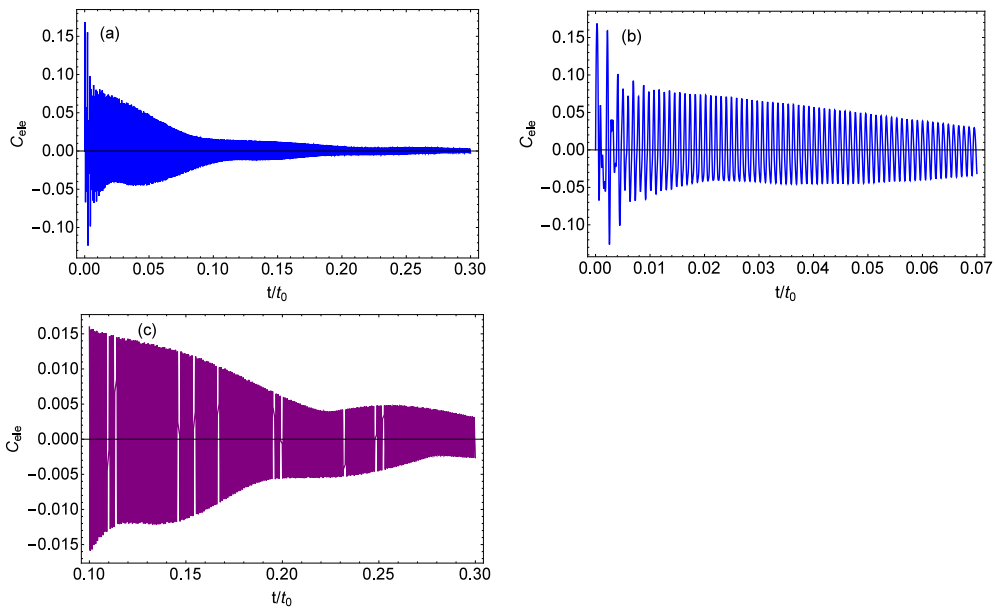


Figure 3.9: (Color online) Time evolution of electronic coherence for the cases including two vibrational modes. (b) and (c) are the zooming-in of coherence dynamics in different subintervals of time. The parameters are the same as in Fig.1 in main text.

coherence, as shown in Fig.3.8(d). It shows that both electronic and excitonic coherences are enhanced by decreasing the temperature of low-frequency fluctuations (phonons). This with the fixing temperature of incoherent radiations effectively increases the degree of nonequilibriumness characterized by detailed-balance-breaking. It indicates that the enhancement of steady-state quantum coherence can be attributed to the time-irreversibility (from nonequilibriumness by detailed-balance-breaking) of the whole system. It is also demonstrated that the steady-state coherence is considerably promoted in the far-from-equilibrium regime [31, 34].

Moreover, the promotion of energy transfer discussed above can be understood from the underlying nonequilibrium feature with the detailed-balance-breaking at steady state as we suggested [31, 32, 34, 61, 65], since the nonequilibriumness generated by two heat sources can funnel the path and subsequently facilitate the unidirectional energy transfer, as shown in Fig.3.8(c). As pointed out above, the breakdown of time-reversal symmetry at steady state from the violation of the detailed balance plays an essential role for long-survived oscillation of coherence to assist the enhancement of energy transfer.

On the other hand, the general mechanism uncovered in our model demonstrates that the slowing-down of dynamical decoherence is dominated by the suppression of exciton-environment interaction, rather than the time-irreversibility. Hence from Lindblad equation, it is important to emphasize that the typical time scale for decoherence is mainly governed by the system-environment interaction, while the time-irreversibility from the detailed-balance-breaking is mostly responsible for efficient energy transport and the improvement of coherence at steady state [31, 34, 65], shown in Fig.3.8(c).

### 3.2.8 Effect of multiple vibrational modes

It is worthy to point out that multiple vibrational modes will considerably elongate the surviving time of excitonic coherence, as generally elucidated in our model. As shown in Fig.3.9, the electronic coherence by including two vibrational modes survives much longer than that by including one mode only (Fig.3.7). Quantitatively  $\bar{\tau}_2/\bar{\tau}_1 \sim 10$ , which agrees with our theoretical estimation at the beginning.

### 3.2.9 Discussion and conclusion

In this section we uncover a mechanism in a general scenario for the long-lived coherence. The bare exciton is surrounded by a cloud consisting of discrete vibrational modes. This forms a new composite called polaron. The interactions between the system and the environments are consequently suppressed with respect to that of the bare excitons. This suggests that vibrational coherences generated by exciton-vibron coupling play a significant role in improving greatly the surviving time of the electronic and the excitonic coherences. This general mechanism has never been uncovered before to the best of our knowledge, although some investigations show the existence of the long-lived coherence, at numerical level [27, 99]. Besides, the role of the ground-state coherence was also uncovered, which was elucidated to be non-trivial and essential for promoting the excitation energy transfer in pigment-protein complexes. The approaches popularly applied before were also shown to fail in predicting the role of vibrational coherence, especially the ground-state coherence on dynamical excitonic energy transfer. We also illustrated the nonvanishing steady-state coherence is promoted by the time-irreversibility originated from the detailed-balance-breaking of the system. Furthermore our results on the slowing-down of dynamical decoherence from weaker coupling to environment and nonvanishing steady-state coherence from detailed-balance-breaking leading to efficient energy transfer provide a possible way to optimize the quantum information process.

# Chapter 4

## Quantum dynamics in ultracold gas and quantum information: relaxation process II

The contents in this chapter are based on Ref.[103, 104].

### 4.1 Breakdown of scale invariance in the vicinity of the Tonks-Girardeau limit

#### 4.1.1 Lieb-Liniger model

The one-dimensional Bose gas with contact interactions is a simple and important model for the study of many-body physics. The recent progress in the trap, laser cooling have made it experimentally realizable and also have led to a renewed interest in quasi-one-dimensional ultracold bosons with short-range interactions. One of the most significant results in previous decades relevant to this field was the Lieb-Liniger (LL) gas [105, 106], in which point interactions were described by Dirac delta functions:  $U(x_n - x_m) = g_B \delta(x_n - x_m)$ . The recent development of Bose-Einstein condensate provides the feasibility to transversally confine the spinless bosons by tight harmonic potentials and thus to allow the longitudinal  $s$ -wave scattering only. Therefore the effective coupling strength between bosons in 1D could be achieved by the 3D scattering length  $a_{3D}$  [49] and the characteristic length scale  $\ell_{\perp} = \sqrt{\hbar/m\omega_{\perp}}$  of transverse motion where  $\omega_{\perp}$  designates the transverse

trapping frequency. As is known, the interaction between bosons in 3D can be simply governed by one parameter called scattering length, in low energy limit (*s*-wave approximation). Hence the 3D pseudopotential between two bosons is

$$U(\mathbf{r}, \mathbf{r}') = \frac{4\pi\hbar^2 a_{3D}}{m} \delta(\mathbf{r} - \mathbf{r}') \frac{\partial}{\partial |\mathbf{r} - \mathbf{r}'|} |\mathbf{r} - \mathbf{r}'| \quad (4.1.1.1)$$

which was also called Lee-Huang-Yang potential [107, 108, 109].  $m$  is the mass of the atom. The scattering length  $a_{3D}$  can be successfully tuned in a wide range by Feshbach resonance [110]. For quasi-1D case, by considering the effects of transverse confinement it was found that  $g_B = 2\hbar^2/(ma)$ . Here  $a$  refers to the effective 1D *s*-wave scattering length [111, 112] and

$$a = -\frac{\ell_{\perp}^2}{2a_{3D}} \left( 1 - C \frac{a_{3D}}{\ell_{\perp}} \right) \quad (4.1.1.2)$$

where  $C = 1.4603\dots$  [111]. This result show that the 1D coupling strength between bosons can be tuned by adjusting the 3D scattering length in the experiments. Hence the Hamiltonian of Lieb-Liniger model is of the form

$$H_{LL} = -\frac{\hbar^2}{2m} \sum_{i=1}^N \frac{\partial^2}{\partial x_i^2} + \frac{2\hbar^2}{ma} \sum_{i<j} \delta(x_i - x_j) \quad (4.1.1.3)$$

which is exactly solvable by Bethe ansatz [105, 106]. One can see that in Tonks-Girardeau limit ( $g_B \rightarrow \infty$ ) the system is scale invariant [113, 114, 115]. This in other words, indicates that the many-body interaction will lead to the breakdown of scale invariance, which may be testable in experiments.

## 4.1.2 Scale invariance

In scale-invariant systems, the Hamiltonian is of a homogeneous function:  $H(\lambda\mathbf{r}) = \lambda^{\beta} H(\mathbf{r})$ , which indicates the rescaling of system energy by an arbitrary dimensionless constant. This in other words, means no bound state in the system, since the scale invariance is always associated with an inability of the interaction potential to introduce a distinct length scale. Several examples emerged recently in the physics of quantum gases. In three dimensions, the  $\delta$ -interaction with infinite coupling strength (the Tonks-Girardeau gas), even when properly regularized, ensures the scale invariance of the unitary

gases [116, 117, 118, 119, 120]. In 2D, the unregularized  $\delta$ -potential, for arbitrary coupling strength, induces the scale invariance of two-dimensional Bose [121, 122] and spin-1/2 Fermi [123] gases at the classical field level, which is however broken by quantization. Scale invariance enables a robust frequency gauge: when a scale-invariant gas is placed in a symmetric harmonic trap of frequency  $\omega$  and a monopole oscillation is produced, the signal shows neither damping nor amplitude-dependent frequency shifts: its frequency is fixed to  $2\omega$ , for all scale invariant systems and for all spatial dimensions [124]. As a consequence, monopole excitations in scale-invariant systems are very sensitive to changes in the equation of state, whether produced by a quantum anomaly [125, 126, 127], by an influence of the confining dimension [128], or just by a small shift in the coupling constant away from the scale-invariant point. Later on we will elucidate this point by studying both the microscopic and macroscopic excitations of the harmonically trapped Lieb-Liniger gas.

### 4.1.3 Lieb-Liniger gas in a trapping potential

The Lieb-Liniger model for a homogeneous Bose gas is too idealized to study close to most experiments which involve a longitudinal confinement. Therefore it is natural and necessary to generalize this model to the situation with an external trap [129, 130, 131]. The simplest and most commonly applied one is the harmonic trap  $V(x) = \frac{1}{2}m\omega^2x^2$ , experimentally produced by magnetic quadrupole interaction [110]. Then the Hamiltonian for a harmonically trapped Lieb-Liniger gas is

$$H_B = \sum_{i=1}^N \left( -\frac{\hbar^2}{2m} \frac{\partial^2}{\partial x_i^2} + \frac{1}{2}m\omega^2x_i^2 \right) + \frac{2\hbar^2}{ma} \sum_{i<j} \delta(x_i - x_j) \quad (4.1.3.1)$$

where  $a$  refers to the 1D scattering length and  $\omega$  stands for the trapping frequency of harmonic potential.

Unfortunately, this harmonically trapped Lieb-Liniger model is difficult to investigate for general values of the particle number  $N$  and interaction strength  $g_B$ , even though it still remains solvable in certain limits, e.g., TG gas of infinite repulsion ( $g_B \rightarrow \infty$ ) [113]. This is because the external trap breaks the translational symmetry of the system, which furthermore gives rise to the position-dependence of the two-body scattering phase. Thus the integrability of the system is destroyed. On the other hand, for the situation away from the TG limit—even remaining infinitesimally close to it—there exists

conceptual difficulties in interpreting the resulting system as one governed by a Hamiltonian for free fermions plus a small correction [132]. Despite of this, as inspired by recent experiments associated with ultradilute gas [114, 115], the ground state and low-lying excitations have been studied in the strongly-coupling regime [133] and Thomas-Fermi limit by a numerical way [129, 130, 134, 135, 136]. In the forthcoming section we will *analytically* obtain the monopole excitation with microscopically small amplitude and will show its surprising agreement with the macroscopic excitation with microscopical large but macroscopic small amplitude [103].

#### 4.1.4 Bose-Fermi duality

The Bose-Fermi duality in one dimension can establish the mapping between the bosonic and fermionic models with the same energy spectrum and the inversed coupling strength [137, 138]. Particularly the spinless bosons with contact coupling strength  $c$  can be mapped into a scalar fermionic model with interaction of strength  $\sim 1/c$  [139]. Specifically the duality between the spinless bosons and its fermionic counterpart is written as the following correspondence

$$\Phi_B(x_1, x_2, \dots, x_N) = \mathcal{A}\Phi_F(x_1, x_2, \dots, x_N) \quad (4.1.4.1)$$

where the function  $\mathcal{A} = \prod_{j<l} \text{sgn}(x_j - x_l)$ . From the  $\delta$ -barrier scattering in quantum mechanics we know that the bosonic wave function  $\Phi_B$  for Eq.(4.1.3.1) is continuous at the boundary  $x_i = x_j$  but has a jump on derivative

$$\left( \frac{\partial}{\partial x_i} - \frac{\partial}{\partial x_j} \right) \Phi_B \Big|_{x_i \rightarrow x_j^+} - \left( \frac{\partial}{\partial x_i} - \frac{\partial}{\partial x_j} \right) \Phi_B \Big|_{x_i \rightarrow x_j^-} = \frac{2}{a} \Phi_B|_{x_i=x_j} \quad (4.1.4.2)$$

Correspondingly it is straightforward to show that the fermionic wave function itself has a jump at the boundary  $x_i = x_j$  but is continuous on derivative

$$\Phi_F|_{x_i \rightarrow x_j^+} - \Phi_F|_{x_i \rightarrow x_j^-} = 2a \left( \frac{\partial}{\partial x_i} - \frac{\partial}{\partial x_j} \right) \Phi_F \Big|_{x_i \rightarrow x_j} \quad (4.1.4.3)$$

Thus  $\Phi_F$  becomes continuous as approaching the TG limit of infinite repulsion ( $g_B \rightarrow +\infty$ ). As a result of Bose-Fermi mapping, all of the physical

quantities that are functions of the local density of the particles are identical in both systems in that only the absolute values of wave functions are involved, which are the same for both systems [140, 141].

For our purpose, the interaction produced by mapping to fermionic system needs to be found. It has explicitly constructed the interaction potential by considering the boundary conditions in Eq.(4.1.4.3) [139, 142]. Thus the fermionic interaction can be written in terms of an integral kernel [139, 141]

$$U_F(x_1, x_2; x'_1, x'_2) = -\frac{4\hbar^4}{m^2 g_B} \delta\left(\frac{x_1 + x_2 - x'_1 - x'_2}{2}\right) \delta'(x_1 - x_2) \delta'(x'_1 - x'_2) \quad (4.1.4.4)$$

The Hamiltonian  $H_F$  for fermionic counterpart is of the same form of Eq.(4.1.3.1) but with a different interaction term  $\sum_{i<j} U_F(x_i, x_j; x'_i, x'_j)$ .  $\Phi_F$  obeys the eigenequation of  $H_F$  if  $\Phi_B$  obeys the eigenequation for  $H_B$ , with the identical eigenvalues.

From the formalism of *quantum field theory*, the Hamiltonian for the scalar fermions can be written in a compact form using the fermionic field operators  $\hat{\Psi}(x)$  and  $\hat{\Psi}^\dagger(x)$

$$\hat{\mathcal{H}}_F = \frac{\hbar^2}{2m} (\partial_x \hat{\Psi}^\dagger \partial_x \hat{\Psi}) + \frac{m x^2}{2} \hat{\Psi}^\dagger \hat{\Psi} - \frac{2\hbar^4}{m^2 g_B} (\partial_x \hat{\Psi}^\dagger) \hat{\Psi}^\dagger \hat{\Psi} (\partial_x \hat{\Psi}) \quad (4.1.4.5)$$

and  $\hat{H}_F = \int_{-\infty}^{+\infty} \hat{\mathcal{H}}_F dx$ . The fermionic field operators obey the anti-commutation relation

$$\{\Psi(x), \Psi^\dagger(y)\} = \delta(x - y), \quad \{\Psi(x), \Psi(y)\} = \{\Psi^\dagger(x), \Psi^\dagger(y)\} = 0 \quad (4.1.4.6)$$

This effective fermionic Hamiltonian enables us to work in the regime of strongly repulsive coupling, based on the perturbation expansion, in that the strongly repulsive bosons are mapped into the weakly attractive fermions.

### 4.1.5 Monopole excitaiton of a microscopically small amplitude

The fermionic field in Eq.(4.1.4.5) can be expanded into a series over the single atom orbitals of the harmonic trap

$$\hat{\Psi}_F(x) = \sum_n \hat{b}_n \varphi_n(x), \quad \varphi_n(x) = \left(\frac{1}{2^n n! \sqrt{\pi} \ell}\right)^{\frac{1}{2}} e^{-x^2/(2\ell^2)} H_n(x/\ell) \quad (4.1.5.1)$$

where  $H_n(\xi)$  is the  $n$ -th Hermite polynomial and  $\ell \equiv \sqrt{\hbar/m\omega}$ . The operator  $\hat{b}_n$  is the fermionic annihilation operator that removes one particle from the  $n$ -th eigenstate. The operators  $\hat{b}_n$  obey the standard fermionic commutation relations and the Hamiltonian in Fock space is of the form

$$\hat{H}_F = \frac{N}{2}\hbar\omega + \sum_{n=0}^{\infty} n\hbar\omega\hat{b}_n^\dagger\hat{b}_n - \frac{\hbar^4}{m^2g_B\ell^3} \sum_{\substack{n<m \\ n+m+k+l=\text{even}}}^{\infty} \sum_{k<l}^{\infty} \Omega_{kl}^{nm}\hat{b}_n^\dagger\hat{b}_m^\dagger\hat{b}_k\hat{b}_l \quad (4.1.5.2)$$

where  $\Omega_{kl}^{nm} = 2 \int_{-\infty}^{\infty} d\xi (\varphi'_n\varphi_m - \varphi_n\varphi'_m) (\varphi'_l\varphi_k - \varphi_l\varphi'_k)$ . The ground state of whole system is

$$|\Psi_0\rangle = \left( \prod_{n=0}^{N-1} \hat{b}_n^\dagger \right) |vac\rangle \quad (4.1.5.3)$$

where  $|vac\rangle$  stands for the vacuum with no particle at all. The energy correction of ground state is analyzed in section of derivation in Ref.[103], where we will show our result recovers the formula in Ref.[133].

Now we will come to the 2<sup>nd</sup> excitations. The unperturbed manifold of energy  $E_0^{(0)} + 2\hbar\omega$  is of two-fold degeneracy. The set of unperturbed eigenstates is  $\left\{ |\Psi_{2a}\rangle = \hat{b}_{N+1}^\dagger\hat{b}_{N-1}\hat{b}_N|\Psi_0\rangle, |\Psi_{2b}\rangle = \hat{b}_N^\dagger\hat{b}_{N-2}\hat{b}_N|\Psi_0\rangle \right\}$ . Based on the perturbation theory, corrections to the energies are represented by the spectrum of the  $2 \times 2$  matrix of the perturbation term in the space spanned by the members of the manifold

$$\hat{V} = \frac{\hbar^4}{m^2g_{1D}\ell^3} \begin{pmatrix} I_N^{(2a)} & \Omega_N \\ \Omega_N & I_N^{(2b)} \end{pmatrix} \quad (4.1.5.4)$$

with  $\Omega_N \equiv \Omega_{N-1,N}^{N-2,N+1}$ ,  $I_N^{(2a)} = \sum_{m=1}^{N+1(a)} \sum_{n=0}^{m-1} v_{nm}$ , and  $I_N^{(2b)} = \sum_{m=1}^{N(b)} \sum_{n=0}^{m-1} v_{nm}$ . Hence the transition frequencies for microscopically small amplitude read

$$\begin{aligned} \hbar\omega_{2\pm,0} &= 2\hbar\omega + \frac{1}{2} \frac{\hbar^4}{m^2g_{1D}\ell^3} \left[ I_N^{(2a)} + I_N^{(2b)} - 2I_N^{(0)} \right. \\ &\quad \left. \pm \sqrt{(I_N^{(2a)} - I_N^{(2b)})^2 + 4\Omega_N^2} \right] + \mathcal{O}(1/(g_{1D})^2) \end{aligned} \quad (4.1.5.5)$$

where  $I_N^{(0)} \equiv \sum_{m=1}^{N-1} \sum_{n=0}^{m-1} v_{nm}$  and  $v_{nm}$  takes the form of

$$v_{nm} = \sqrt{\frac{2}{\pi^3}} \frac{(m-n)^2 \Gamma(m-\frac{1}{2}) \Gamma(n-\frac{1}{2})}{\Gamma(m+1) \Gamma(n+1)} {}_3F_2 \left[ \begin{matrix} \frac{3}{2}, -n, -m \\ \frac{3}{2} - n, \frac{3}{2} - m \end{matrix}; 1 \right] \quad (4.1.5.6)$$

After a lengthy but straightforward calculation (see the Appendices in Ref.[103]), we obtain the analytical form of  $1/g_{1D}$  corrections to the relevant transition frequencies:

$$\hbar\omega_{2+,0} \equiv 2\hbar\Omega_D = \left(2 + \mathcal{O}\left(\frac{1}{\gamma_0^2(N)}\right)\right) \hbar\omega \quad (4.1.5.7)$$

$$\begin{aligned} \hbar\omega_{2-,0} \equiv \hbar\Omega_M = & \left(2 - \frac{6}{\sqrt{\pi}} \frac{\sqrt{N}\Gamma(N - \frac{5}{2})\Gamma(N + \frac{1}{2})}{\Gamma(N)\Gamma(N + 2)} \right. \\ & \left. \times {}_3F_2 \left[ \begin{matrix} \frac{3}{2}, 1 - N, -N \\ \frac{7}{2} - N, \frac{1}{2} - N \end{matrix}; 1 \right] \frac{1}{\gamma_0(N)} + \mathcal{O}\left(\frac{1}{\gamma_0^2(N)}\right) \right) \hbar\omega, \end{aligned} \quad (4.1.5.8)$$

where  $\hbar\omega_{2\pm,0} = E_{2\pm} - E_0$ , are the transition frequencies,  $E_0$  is the ground state energy, and  $E_{2\pm}$  are the energies of the states that, in the strict TG limit, form a two-fold degenerate manifold,  $2\hbar\omega$  above the ground state. The effective Lieb-Liniger parameter  $\gamma_0(N) \equiv (mg_{1D})/(n_{\text{TF}}\hbar^2)$  [106] uses the TG (i.e.  $g_{1D} \rightarrow \infty$ ) density in the center of the trap,  $n_{\text{TF}} \equiv (\sqrt{2}/\pi)\sqrt{N}\sqrt{m\omega/\hbar}$ , instead of the true density. Here,  ${}_3F_2[a_1, a_2, a_3; b_1, b_2; z]$  is the generalized hypergeometric function of order (3, 2).

The interpretation of the  $2\pm$  eigenstates can be inferred from the corresponding transition frequencies. The first one (2+) is the second state of an infinite  $\hbar\omega$ -spaced “dipole” ladder: coherent wave packets formed out of the members of the ladder represent finite amplitude dipole excitations; their frequency  $\Omega_D$  is equal to the frequency of the trap *exactly*, interactions notwithstanding [143]. The zeroth state is the ground state. The first state of the ladder corresponds to the unique state  $|\Psi_1\rangle = \hat{b}_N^\dagger \hat{b}_{N-1} |\Psi_0\rangle$  in the first excited state manifold, and thus the correction to the energy is  $E_1^{(1)} = \langle \Psi_1 | \hat{V} | \Psi_1 \rangle$ . The formula for the transition frequency,  $\hbar\omega_{1,0} \equiv E_1 - E_0$ , assumes a compact form, and it reads

$$\hbar\omega_{1,0} \equiv \hbar\Omega_D = \hbar\omega + \mathcal{O}\left(\frac{1}{\gamma_0(N)^2}\right) \quad (4.1.5.9)$$

We interpret the state  $|\Psi_1\rangle$  as the first state of an infinite  $\hbar\omega$ -spaced “dipole” ladder: coherent wave packets formed out of the members of the ladder represent finite-amplitude dipole excitations (*i.e.* oscillations of the center of mass); their frequency  $\Omega_D$  is equal to the frequency of the trap *exactly*, interactions notwithstanding. The zeroth state of the ladder is the ground state.

The second eigenstate ( $2-$ ) in the  $E_0^{(0)} + 2\hbar\omega$  manifold, is the first (ground state being the zeroth) step in the “monopole” ladder, that corresponds to the breathing excitations of frequency  $\Omega_M$ . In the noninteracting case, the ladder (exactly  $2\hbar\omega$ -spaced) can be obtained by a recurring application of the creation operator  $\hat{L}_+$  of an appropriate  $SO(2, 1)$  group to the ground state [124]. The excitation dynamics consists of a periodic scaling transformation of frequency  $2\omega$ . The existence of this structure is a direct consequence of the scale invariance of the TG gas and its free-fermionic counterpart in the harmonic potential.

A deviation from the TG limit (and the corresponding fermion-fermion interactions (4.1.4.5)) *breaks the scale invariance weakly*. The goal of this work is to assess the impact that this effect has on the excitations of a microscopic amplitude and compare it to the corresponding predictions for the microscopically large but macroscopically small excitations.

As far as the microscopic amplitude excitations are concerned, our program is already fulfilled. Indeed, a linear combination of the ground state and a small admixture of the state  $2-$  is already a small amplitude monopole excitation. Its frequency is given by the formula (4.1.5.8) that *constitutes the central result of this work*.

#### 4.1.6 Comparison to the other few-body results

We verified that for two atoms ( $N = 2$ ), the formula (4.1.5.8) for the frequency of the small amplitude monopole excitations coincides with the known exact results [144].

In the three-body case ( $N = 3$ ) we perform a Diffusion Monte Carlo simulation of the imaginary time evolution and extract the  $\omega_{2-,0}$  transition frequency from the inverse Laplace transform components of the imaginary-time dynamic structure factor.

In Fig. 4.1 we compare our (non-perturbative) numerical three-body results with the perturbative prediction (4.1.5.8). In Fig. 4.2, the dominant corrections to the monopole frequency for  $N = 2$  and  $N = 3$ , extracted from the non-perturbative data, are also compared to formula (4.1.5.8).

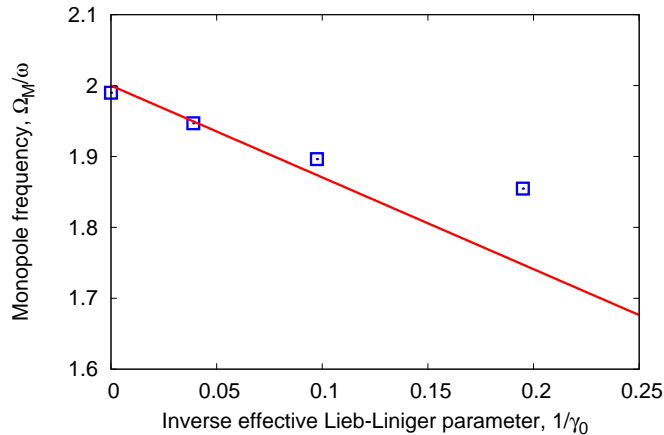


Figure 4.1: (Color online). The frequency of a small amplitude monopole excitation for  $N = 3$  one-dimensional bosons in a harmonic trap, as a function of the inverse of the effective Lieb-Liniger parameter  $\gamma_0$  (see text). Solid line (red online): the prediction of the formula (4.1.5.8) for the first two terms of the expansion of frequency in powers of  $1/\gamma_0$ . Open squares (blue online): the ab initio Diffusion Monte Carlo simulation.

#### 4.1.7 Large- $N$ asymptotics and a comparison with the sum-rule predictions

The frequency of the monopole excitations of a microscopically small amplitude can be bounded from above using the sum rules [130] (see Fig. 4.3). The order  $1/g_{1D}$  correction to this bound can also be computed analytically, for large atom numbers [145]:

$$\hbar\Omega_M \stackrel{N \gg 1}{\cong} \left( 2 - \frac{64}{15\pi} \frac{1}{\gamma_0(N)} + \mathcal{O}\left(\frac{1}{\gamma_0^2(N)}\right) \right) \hbar\omega \quad (4.1.7.1)$$

We conjecture that the upper bound (4.1.7.1) actually equals the exact prediction (4.1.5.8) in the limit of large  $N$ . To test this conjecture, we multiplied the  $\frac{1}{\gamma_0(N)}$ -term in the the bound (4.1.7.1) by  $AN^\sigma$ , with  $A$  and  $\sigma$  being free parameters to be used to fit the  $\frac{1}{\gamma_0(N)}$  term in the series (4.1.5.8). Indeed we found the values that support our conjecture, namely  $A = 1.000$  and  $\sigma = 0.0003$ .

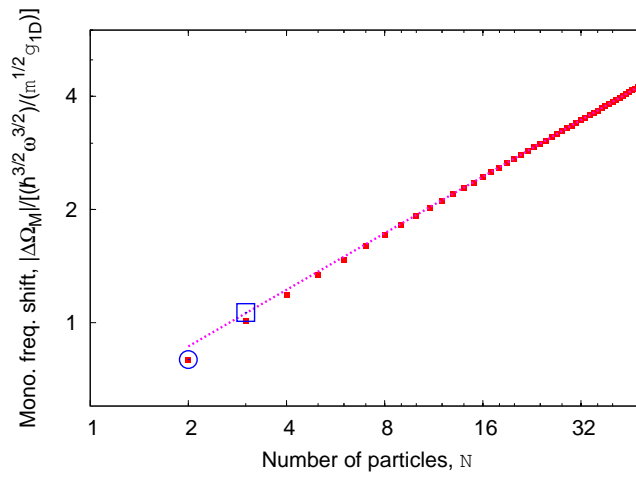


Figure 4.2: (Color online). The magnitude of the dominant correction, in a power-series expansion in  $1/\gamma_0$ , to the result predicted by the scale invariance,  $\Omega_M = 2\omega$ . Filled squares (red online): the analytic formula (4.1.5.8). Open circle (blue online): the exact nonperturbative solution for  $N = 2$ . Open square (blue online): the Diffusion Monte Carlo simulation for  $N = 3$ . Dotted line (purple online): the  $N \gg 1$  limit of the sum-rule prediction (also Eq. (4.1.7.1)).

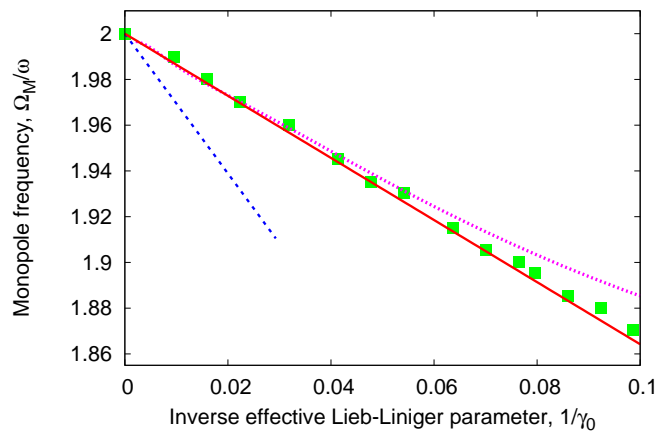


Figure 4.3: (Color online). The frequency of both the microscopically small and microscopically large but macroscopically small monopole excitations, in the limit of  $N \gg 1$ . Solid line (red online): the formula (4.1.5.8). Dotted line (purple online): the sum-rule upper bound (courtesy of Chiara Menotti and Sandro Stringari). Filled squares (green online): the numerically exact hydrodynamic simulation of the motion of a macroscopic motion of small amplitude. Dashed line (blue online): the hydrodynamic perturbation theory for the latter. For definition of  $\gamma_0$ , see text.

### 4.1.8 Comparison to the frequencies of the excitations of a microscopically large but macroscopically small amplitude

The monopole frequencies obtained above correspond to excitations of *microscopically small amplitude*: there the many-body energy of the excited atomic cloud is only a few one-body harmonic quanta above the ground state energy. *A priori* it is not obvious if the microscopic predictions will remain valid for *microscopically large but macroscopically small* excitations, whose *spatial amplitude is smaller than but comparable to the size of the cloud*.

To compare the two frequencies, we investigate the time dynamics using the hydrodynamic equations (see e.g. Eqs. (1) and (2) of Ref.[146]). We use the well-known thermodynamic limit for the dependence of the zero-temperature chemical potential  $\mu(n)$  on the one-dimensional particle density  $n$ , for a uniform one-dimensional  $\delta$ -interacting Bose gas; this equation of state was obtained by Lieb and Liniger, using Bethe Ansatz [106]. We propagate the hydrodynamic equations numerically. To excite the monopole mode, we quench the trapping frequency. Fig. 4.3 shows a good agreement with the large- $N$  asymptotics for the frequency of the microscopically small excitations (4.1.7.1).

In order to obtain an analytic expression for the frequency shift, we apply the perturbation theory developed by Pitaevskii and Stringari in Ref.[146] (with more technical details worked out in Ref.[128], for the purpose of computing an analytic expression for the dominant beyond-mean-field correction to the monopole frequency of a BEC. Here we use the TG equation of state (EoS),  $\mu_0(n) = (\pi^2\hbar^2/2m)n^2$  as the unperturbed EoS, and the first-order (in  $\gamma(n)^{-1}$ ) correction to the EoS,  $\Delta\mu(n) = (8\pi^2\hbar^2/3m)n^2\gamma(n)^{-1}$ , as a perturbation. The function  $\gamma(n) \equiv (mg_{1D})/(n\hbar^2)$  is the so-called Lieb-Liniger parameter [106]. While most of the outlined steps of the study in Ref.[128, 146] are universally applicable to any EoS, the boundary conditions for the density mode functions  $\delta n(z)$  at the edge of the atomic cloud  $|z| = R_{\text{TF}}$  are typically dictated by the specific physical properties of the system at hand. (Here  $R_{\text{TF}}$  is the Thomas-Fermi radius.) In the TG case, with or without further beyond-the-TG corrections to the EoS, those are given by

$$\begin{aligned}\delta n(z) &= A(R_{\text{TF}} - |r|)^{-1/2} + B + \mathcal{O}((R_{\text{TF}} - |r|)^{1/2}) \\ B &= 0.\end{aligned}\tag{4.1.8.1}$$

Indeed, following the analysis developed in Ref.[128], one can show (i) that

the first two terms in (4.1.8.1) correspond to the near-edge asymptotic of the two linearly independent solutions of the mode equation, and (ii) that when rewritten in Lagrange form [147], the solutions that violate condition (4.1.8.1) lead to the appearance of crossing particle trajectories, incompatible with hydrodynamics.

To our surprise, we found that the macroscopic perturbation theory leads to a frequency shift that is 9/4 times greater in magnitude than its microscopic counterpart Eq. (4.1.7.1) (see Fig. 4.3). This is definitely an artifact of the perturbative treatment of the macroscopic theory rather than of the macroscopic theory per se. Indeed, our macroscopic nonperturbative numerical results are consistent with the microscopic theory. We attribute the failure of the perturbation theory to the divergence of the spatial derivative of the steady-state density at the edge of the cloud: in a monopole excitation this will lead to an infinite time derivative of the density itself, possibly invalidating the perturbation theory.

In the same plot, we also present the sum-rule bound [130]. At weak fermion-fermion interactions, it reproduces well the perturbative prediction Eq. (4.1.7.1).

#### 4.1.9 Conclusion and outlook

In this work, we obtained an analytic expression, Eq. (4.1.5.8) for the leading behavior of the deviation of the frequency of the microscopically small monopole excitations of a strongly-interacting one-dimensional Bose gas from the value predicted by the scale invariance in the TG limit.

We further compare this prediction with (a) the known non-perturbative analytic expressions for two atoms [144] and to (b) the Diffusion Monte Carlo predictions for three atoms. For large numbers of atoms, the prediction in Eq. (4.1.5.8) stands in excellent agreement with (c) the sum-rule bound (4.1.7.1) [130, 145]. It was not *a priori* obvious to us if our formula will also apply to *microscopically large but macroscopically small* excitations: they correspond to a large number of atoms (still covered by the formula (4.1.5.8)), and have a macroscopic magnitude (that is formally beyond the scope of Eq. (4.1.5.8)). We found that (d) the numerically propagated hydrodynamic equations produce the same leading-order frequency correction as the large- $N$  limit of Eq. (4.1.5.8). Finally, we find that (e) the hydrodynamic perturbation theory, which was so successful in predicting the beyond-mean-field corrections to the monopole frequency in both the three-dimensional

[146] and the two-dimensional [128] Bose gases, fails to predict the analogous beyond-TG correction in our case: the hydrodynamic perturbative prediction turns out to be approximately 9/4 higher than the *ab initio* numerical value it was designed to approximate. We conjecture that the sharp boundary of the TG cloud, characterized by an infinite density gradient, renders the perturbation theory inapplicable.

Experimentally, the monopole excitation frequency of the Lieb-Liniger gas has been already studied, in Ref.[131]. In the range of parameters our article is devoted to, the beyond-scale-invariance shifts are too small to be reliably compared with the experimental data. However, we plan to extend our study of the frequency of microscopically large but macroscopically small monopole excitations to the whole range of the interaction strengths. One can already observe that in the intermediate range, the experimental frequencies [131] depart from the sum-rule upper bound [130]. It appears to be of interest to verify that the numerically propagated hydrodynamic equations can reproduce the experimental points.

A study of the *finite amplitude* beyond-TG corrections to the monopole frequency may be of interest. Another possible direction is computing the higher orders of the perturbation theory for the frequency correction. This step is challenging, however: the odd-wave fermion-fermion interaction potential in Eq. (4.1.4.5) cannot be used as such, and it requires a prior regularization [132], similar to the Fermi-Huang regularization of the three-dimensional  $\delta$ -potential.

Results of our work directly apply to another system: the spin-polarized  $p$ -wave-interacting fermions in a wave-guide [148]. The mapping between this system and the Lieb-Liniger gas of  $\delta$ -interacting bosons is provided by Granger and Blume, in the final formula of Ref.[149]. In the case of  $^{40}\text{K}$  atoms, the  $p$ -wave scattering volume  $V_p$  can be controlled at will, using an accessible  $l = 1$ ,  $m_l = 0$  Feshbach resonance at 198.8 G [150]. When atoms are confined to a one-dimensional harmonic waveguide, the position of the resonance is further shifted [148] due to the presence of a confinement-induced resonance (CIR) [149]. For example, an ensemble of  $N = 500$   $^{40}\text{K}$  atoms, transversally frozen to a harmonic waveguide of a confining frequency of  $2\pi \times 25$  kHz and longitudinally trapped by a harmonic potential of frequency  $2\pi \times 5$  Hz, will show a  $\omega_{2-,0}/\omega - 2 = -4.7\%$   $p$ -wave-interaction-induced shift of the monopole frequency, for the  $p$ -wave scattering volume of  $V_p = -(1000 a_B)^3$  (with the CIR value situated at  $(V_p)_{\text{CIR}} = -(2004 a_B)^3$ ). To relate this value of the scattering volume to the detuning from the Feshbach resonance,

note that the above value of the scattering volume would correspond to a binding energy of the three-dimensional  $p$ -wave dimers [149, 151] of  $E_{\text{dimer}} \equiv -\hbar^2/2\tilde{\mu}(V_p)^{2/3} = h \times 92.3\text{kHz}$ ; the later value occurs if the magnetic field is detuned by 0.49 G below the  $l = 1$ ,  $m_l = 0$  resonance (see a the caption to Fig. 2 in Ref.[151] for the slope of the binding energy vs. magnetic field curve). In general, the slope of the dimer energy as a function of the magnetic field is measured to be  $h \times 188 \pm 2\text{kHz/G}$ . Here,  $\tilde{\mu} = m/2$  is the reduced mass, and  $h = 2\pi \times \hbar$  is Plank's constant.

## 4.2 Nonequilibrium-induced enhancement of dynamical quantum coherence of spin arrays

Quantum information and computing attracted much focus due to its great potential and perspective in the application of teleportation. To experimentally realize the quantum computing, the solid-state-based devices are shown to take much advantage, comparing to the optical devices widely used before. This is because of the experimental accessibility to control and confine the information carriers by solid-state systems, rather than optical devices. Recently the quantum-dot-based spin qubits as a solid-state method is demonstrated to be successful in quantum information processing, such as the control of electron-spin qubits in GaAs quantum dots [38, 39, 40, 41] and sensitive metrology [152]. The singlet and unpolarized triplet states of two electrons are experimentally realized by singlet-triplet (ST) qubits confined in a double quantum dot [41, 153, 154, 155]. This makes the system controllable by tuning the spin-exchange coupling associated with the gate voltage, allowing the qubits to access the control operations. Despite the controllability, the decoherence owing to the influence of nuclei spins in the host materials still remains challenging for maintaining a high fidelity during the quantum computing. Understanding the dynamics of this process is of fundamental importance.

In the materials the spins are subjected to the noise, due to the random magnetic field from the nuclear spins, which is so-called Overhauser noise. This practically results in the dynamics of coherence in a typical timescale. Although the random noise induced by nuclear spins can be artificially mitigated or even eliminated by considerable works, including the Hahn echo

through electron-spin flipping [154], dynamical decoupling [156, 157], how to considerably suppress the decoherence arising from nuclear spins still remains the central role of the study of spin dynamics, owing to the fact that the random magnetic fields from nuclear spins is unavoidable under the natural conditions.

So far, the dynamics of spin arrays has been mostly explored under the influence of Overhauser fields owing to the nuclear hyperfine interactions. However, the natural environments like the nuclei spins around GaAs quantum dots always show the inhomogeneous charge density, which implies the gradient of chemical potentials. It produces an effective voltage, causing the breakdown of detailed-balance (time-reversal symmetry). Hence the system will relax to a nonequilibrium state with time-reversal-breaking, rather than being thermalized as behaved before. Such nonequilibrium effect is lacking to be explored in the previous works, even though under the Overhauser noise certain collective quantum states of spin arrays were shown to be preserved for a long lifetime [158]. In this section, we will deal with this effect by considering the detailed-balance-breaking, and will further uncover a new as well as significant phenomenon of rapid beat oscillation.

### 4.2.1 Spin-chain model

The spin arrays of quantum-dot-based qubits are usually described by the Heisenberg spin chain model of spin- $\frac{1}{2}$  and the Hamiltonian is

$$H_{XYZ} = \sum_n h_n \sigma_n^+ \sigma_n^- - \sum_{(m,n)} (J_{mn}^x \sigma_m^x \sigma_n^x + J_{mn}^y \sigma_m^y \sigma_n^y + J_{mn}^z \sigma_m^z \sigma_n^z) \quad (4.2.1.1)$$

where  $h_n$  is local magnetic field felt by the single spin.  $J_{mn}^i$ ,  $i = x, y, z$  are the spin-spin interaction strength along the three spacial directions. In the most general case,  $J_{mn}^i$  are not equal to each other, which is the so-called XYZ model [159]. However, the one-dimensional XXZ model associated with  $J_{mn}^x = J_{mn}^y \neq J_{mn}^z$  and nearest-neighbour coupling is what people are mostly interested in, since the difference between longitudinal and transversal couplings always dominates. Hence

$$H_{XXZ} = \sum_n h_n \sigma_n^+ \sigma_n^- - \sum_m J_m (\sigma_m^x \sigma_{m+1}^x + \sigma_m^y \sigma_{m+1}^y + \Delta \sigma_m^z \sigma_{m+1}^z) \quad (4.2.1.2)$$

and notice that  $\Delta$  denotes the difference in  $z$ -directional coupling. In this circumstance the 1D XXZ model is exactly solvable by Bethe ansatz [160]. We will focus on this XXZ model hereafter.

As is known, an exact duality between one-dimensional XXZ model and Fermi-Hubbard model with long-range interaction can be established [161]. As inspired by Wigner-Jordan transformation, one can introduce the following operators

$$\begin{aligned} a_n &= \sigma^z \otimes \sigma^z \otimes \cdots \otimes \sigma^z \otimes \sigma^- \otimes 1 \otimes \cdots \otimes 1 \\ a_n^\dagger &= \sigma^z \otimes \sigma^z \otimes \cdots \otimes \sigma^z \otimes \sigma^+ \otimes 1 \otimes \cdots \otimes 1 \end{aligned} \quad (4.2.1.3)$$

where  $\sigma^z$ ,  $\sigma^\pm$  are the standard Pauli matrices. By using the definition of raising and lowering operators  $\sigma^\pm = \frac{1}{2}(\sigma^x \mp i\sigma^y)$  and substituting Eq.(4.2.1.3) into the Hamiltonian of XXZ model Eq.(4.2.1.2),  $H_{XXZ}$  can be written as

$$H_f = \sum_n \varepsilon_n a_n^\dagger a_n - 2 \sum_m J_m (a_m^\dagger a_{m+1} + a_{m+1}^\dagger a_m) - \sum_m U_m n_m n_{m+1} \quad (4.2.1.4)$$

and  $\varepsilon_n \equiv h_n + 4\Delta J_n$ ,  $U_n \equiv 4\Delta J_n$ . Obviously we can verify that  $a_n$ 's are the annihilation operators of fermions at the site  $n$  which satisfy the anti-commutation relation

$$\{a_n, a_m^\dagger\} = \delta_{nm}, \quad \{a_n, a_m\} = \{a_n^\dagger, a_m^\dagger\} = 0 \quad (4.2.1.5)$$

$H_f$  is the standard Fermi-Hubbard model and the last term in Eq.(4.2.1.4) describes the long-range many-body interaction, which originates from the  $z$ -directional coupling in the 1D spin chain. Experimentally this interaction can be tuned to be repulsive or attractive by Feshbach resonance based on ultracold quantum gas [162, 163]. The 1D spin chain alternatively provides a tool to investigate the quantum many-body physics with long-range interaction, going beyond the Hubbard model including only the contact interaction simulated by cold atoms in optical lattice [161, 164, 165, 166]. Moreover the spin chain also establishes the bridge for the communication between condensed matter and AMO physics, especially on the quantum phase transition [110, 166, 167] and quantum information process [168].

## 4.2.2 Model of spin arrays in random magnetic field from nuclear spins

We consider the arrays of two quantum dots where each contains one electron spin (qubit) subject to its own random magnetic field produced by nuclear

spins via hyperfine interactions. By assuming that the nuclei are described by 1D spin chains, two spin chains of nuclei are included and thus the Hamiltonian is

$$\begin{aligned}
H_{ar} &= -J\boldsymbol{\sigma}_1 \cdot \boldsymbol{\sigma}_2 - t \sum_{i=1}^2 \sum_{n=1}^N \mathbf{S}_{n,i} \cdot \mathbf{S}_{n+1,i} + \sum_{i=1}^2 \sum_{n=1}^N f\sigma_i^z S_{n,i}^z + H_{bg} \\
H_{bg} &= \varepsilon \left( \sigma_1^+ \sigma_1^- + \sigma_2^+ \sigma_2^- + \sum_{i=1}^2 \sum_{n=1}^N S_{n,i}^+ S_{n,i} \right) \tag{4.2.2.1}
\end{aligned}$$

where  $J$ ,  $t$  are the spin-spin coupling strengths for electron and nuclear spins, respectively.  $\sigma_n^{+(-)}$  and  $S_{n,i}^{+(-)}$  are the raising (lowering) operators of qubits and nuclear spins, respectively.  $H_{bg}$  is the background contribution to the entire Hamiltonian. In our setup, the spin qubits and nuclear spins are modeled as XY model including the transverse coupling only, namely  $\mathbf{S}_{n,i} \cdot \mathbf{S}_{n+1,i} = S_{n,i}^x S_{n+1,i}^x + S_{n,i}^y S_{n+1,i}^y$ ,  $\boldsymbol{\sigma}_1 \cdot \boldsymbol{\sigma}_2 = \sigma_1^x \sigma_2^x + \sigma_1^y \sigma_2^y$ . The qubit-nuclear interaction is encoded as Ising type, owing to the charge fluctuations [158, 169]. To further solve the dynamics, the free Hamiltonians firstly need to be diagonalized as  $H_0 = 2J(I_1^+ I_1^- - I_2^+ I_2^-) - 4t \sum_{i=1}^2 \sum_k \cos ka S_{k,i}^+ S_{k,i}^-$  where the collective operators are introduced  $I_i^\pm = \sum_{j=1}^2 O_{ij} \sigma_j^\pm$  and

$$\begin{aligned}
O &= \frac{1}{\sqrt{2}} \begin{pmatrix} 1 & -1 \\ 1 & 1 \end{pmatrix} \\
S_{k,i}^\pm &= \frac{1}{\sqrt{N}} \sum_{n=1}^N S_{n,i}^\pm e^{in ka}, \quad k = \left( \frac{2m}{N} - 1 \right) \frac{\pi}{a}; \quad m = 1, 2, \dots, N \tag{4.2.2.2}
\end{aligned}$$

in momentum space.  $\sigma_1^\pm = \sigma^\pm \otimes 1$ ,  $\sigma_2^\pm = \sigma^z \otimes \sigma^\pm$  and  $S_{n,i}^\pm = S^z \otimes S^z \otimes \dots \otimes S^z \otimes S^\pm \otimes 1 \otimes \dots \otimes 1$ , based on the mapping between XXZ spin- $\frac{1}{2}$  chain and 1D Fermi-Hubbard model [161], and  $\sigma^\pm = \frac{1}{2}(\sigma^x \mp i\sigma^y)$ ,  $S^\pm = \frac{1}{2}(S^x \mp iS^y)$  are the standard Pauli matrices. Therefore  $\sigma_n^\pm$ ,  $S_{n,i}^\pm$  satisfy the fermionic anti-commutation relation  $\{\sigma_n^-, \sigma_m^+\} = \delta_{nm}$ ,  $\{\sigma_n^\pm, \sigma_m^\pm\} = 0$ ,  $\{S_{n,i}^-, S_{m,i}^+\} = \delta_{nm}$ ,  $\{S_{n,i}^\pm, S_{m,i}^\pm\} = 0$ .

### 4.2.3 Time evolution

#### Dynamics of entire system

In order to evaluate the time evolution operator, one can start from qubit-nuclear interaction  $V_{int}(t) = V_{int}^{(1)}(t) + V_{int}^{(2)}(t)$  in the interaction picture

$$V_{int}^{(n)}(t) = f \sum_{i,j=1}^2 \sum_k O_{ni}^{-1} O_{nj}^{-1} e^{-i(\omega_i - \omega_j)t} (I_i^- I_j^+ - I_j^+ I_i^-) \otimes S_{k,n}^z \quad (4.2.3.1)$$

by utilizing the identity  $\sum_{n=1}^N e^{i(k-k')na} = N\delta_{k,k'}$  and  $S_{k,n}^z = (S_{k,n}^- S_{k,n}^+ - S_{k,n}^+ S_{k,n}^-)$ . Notice that the operators  $I_i^- I_j^+ - I_j^+ I_i^-$  generate a closed algebra. We then find the operators

$$\begin{aligned} l &= \frac{1}{2} (I_1^- I_1^+ - I_1^+ I_1^- + I_2^- I_2^+ - I_2^+ I_2^-) \\ \eta_1 &= \frac{1}{2} (I_1^- I_2^+ - I_2^+ I_1^- + I_2^- I_1^+ - I_1^+ I_2^-) \\ \eta_2 &= \frac{1}{2i} (I_1^- I_2^+ - I_2^+ I_1^- - I_2^- I_1^+ + I_1^+ I_2^-) \\ \eta_3 &= \frac{1}{2} (I_1^- I_1^+ - I_1^+ I_1^- - I_2^- I_2^+ + I_2^+ I_2^-) \end{aligned} \quad (4.2.3.2)$$

satisfy  $[l, \eta_j] = 0$ ,  $[\eta_i, \eta_j] = 2i\epsilon_{ijk}\eta_k$ , which gives rise to the Lie algebra  $su(2) \oplus u(1)$ . Thereby the qubit-nuclear interaction in Eq.(4.2.3.1) does transform according to the irreducible representation  $\mathcal{D}_0 \oplus \mathcal{D}_{\frac{1}{2}} \oplus \mathcal{D}_0$  of the Lie group  $SU(2) \times U(1)$ . As inspired by the recent experiments [154, 169] the spin qubits are initially engineered at the state  $|S\rangle = \cos\frac{\phi}{2}|1\rangle \otimes |0\rangle + e^{i\theta} \sin\frac{\phi}{2}|0\rangle \otimes |1\rangle$ , which means the dynamical evolution of qubits according to the irreducible representation  $\mathcal{D}_{\frac{1}{2}}$  of group  $SU(2) \times U(1)$  with  $l = 0$ .  $\eta_j$  take the form of  $2 \times 2$  representation

$$\eta_1 = \begin{pmatrix} 0 & -1 \\ -1 & 0 \end{pmatrix}, \quad \eta_2 = \begin{pmatrix} 0 & -i \\ i & 0 \end{pmatrix}, \quad \eta_3 = \begin{pmatrix} -1 & 0 \\ 0 & 1 \end{pmatrix}, \quad (4.2.3.3)$$

Hence by rewriting Eq.(4.2.3.1) in terms of  $l$  and  $\eta_j$ , we obtain the time-evolution operator in the following compact form

$$\begin{aligned}
\mathcal{U}(t) &= e^{-\frac{i}{\hbar} \int_0^t V_{int}^{(1)}(\tau) d\tau} e^{-\frac{i}{\hbar} \int_0^t V_{int}^{(2)}(\tau) d\tau} \\
&= \prod_k \left[ \cos^2 \left( \frac{2f}{\hbar\omega} \sin \frac{\beta}{2} \right) + S_{k,1}^z S_{k,2}^z \sin^2 \left( \frac{2f}{\hbar\omega} \sin \frac{\beta}{2} \right) \right. \\
&\quad \left. - i (\eta_1 \sin \beta - \eta_2 (\cos \beta - 1)) (S_{k,1}^z - S_{k,2}^z) \frac{\sin \left( \frac{4f}{\hbar\omega} \sin \frac{\beta}{2} \right)}{4 \sin \frac{\beta}{2}} \right] \\
&= A_N + i B_N (\sigma_x \text{Re}(p) - \sigma_y \text{Im}(p))
\end{aligned} \tag{4.2.3.4}$$

where  $\beta \equiv \omega t = 4Jt/\hbar$  and  $C_v \equiv S_{v,1}^z S_{v,2}^z$ ,  $D_v \equiv S_{v,1}^z - S_{v,2}^z$ .

$$\begin{aligned}
A_N &= \frac{1}{2} \left[ \prod_{v=1}^N (a + C_v b + i|p|D_v) + \text{h.c.} \right] \\
B_N &= \frac{1}{2i|p|} \left[ \prod_{v=1}^N (a + C_v b + i|p|D_v) - \text{h.c.} \right]
\end{aligned} \tag{4.2.3.5}$$

and

$$a \equiv \cos^2 \left( \frac{f}{2J} \sin \frac{\beta}{2} \right), \quad b \equiv \sin^2 \left( \frac{f}{2J} \sin \frac{\beta}{2} \right), \quad p \equiv \frac{1}{2} e^{i\frac{\beta}{2}} \sin \left( \frac{f}{J} \sin \frac{\beta}{2} \right) \tag{4.2.3.6}$$

Thus the dynamics of the entire system consisting of spin qubits and nuclear spins can be obtained  $\rho(t) = e^{-iH_0 t/\hbar} \mathcal{U}(t) \rho(0) \mathcal{U}^\dagger(t) e^{iH_0 t/\hbar}$ .

#### 4.2.4 Dynamics of spin qubits

In many situations, the dynamics of spin qubits is what people are mostly interested. Therefore we need to trace out the degree of freedoms of nuclear spins to obtain the non-unitary time evolution of spin qubits. Suppose that initially the qubits are engineered at state  $|\Psi(0)\rangle = \frac{1}{\sqrt{2}}(|1\rangle \otimes |0\rangle + e^{-i\theta} |0\rangle \otimes |1\rangle)$  and the nuclear spins are at thermal equilibrium with different chemical potentials (fermi energies). In other words, the initial condition takes the

product form

$$\begin{aligned}\rho(0) &= |\Psi(0)\rangle\langle\Psi(0)| \otimes \rho_{nc}^{\mu_1} \otimes \rho_{nc}^{\mu_2} \\ \rho_{nc}^{\mu_i} &= \frac{1}{Z_i} e^{-\bar{\beta}(H_{nc}^{(i)} - \mu_i N_i)}; \quad \bar{\beta} \equiv \frac{1}{k_B T}, \quad i = 1, 2\end{aligned}\quad (4.2.4.1)$$

After a lengthy but straightforward calculation one can reach the density matrix of spin qubits at moment  $t$ , by tracing out the nuclear spins as environments:  $\rho_s(t) = \text{Tr}_B[\rho(t)]$ . Thus  $\rho_s(t) = \rho_{10,10}(t)|1,0\rangle\langle 1,0| + \rho_{01,01}(t)|0,1\rangle\langle 0,1| + \rho_{10,01}(t)|1,0\rangle\langle 0,1| + \rho_{01,10}^*(t)|0,1\rangle\langle 1,0|$  and the matrix elements are of the form

$$\begin{aligned}\text{Re}\rho_{10,01}(t) &= \left( \prod_{v=1}^N K_v + \mathcal{F}_e(\mu_1, \mu_2, t) \right) \frac{\cos\theta}{2} + \mathcal{F}_o(\mu_1, \mu_2, t) \sin\theta \cos\frac{\beta}{2} \\ \text{Im}\rho_{10,01}(t) &= \left( \cos^2\frac{\beta}{2} \prod_{v=1}^N K_v - \sin^2\frac{\beta}{2} + \mathcal{F}_e(\mu_1, \mu_2, t) \cos^2\frac{\beta}{2} \right) \frac{\sin\theta}{2} \\ &\quad - \mathcal{F}_o(\mu_1, \mu_2, t) \cos\theta \cos\frac{\beta}{2} \\ \rho_{10,10}(t) - \rho_{01,01}(t) &= \left( 1 + \prod_{v=1}^N K_v + \mathcal{F}_e(\mu_1, \mu_2, t) \right) \frac{\sin\theta}{2} \sin\beta \\ &\quad - 2\mathcal{F}_o(\mu_1, \mu_2, t) \cos\theta \sin\frac{\beta}{2}\end{aligned}\quad (4.2.4.2)$$

where

$$K_v = 1 - 2[f_v^{\mu_1}(1 - f_v^{\mu_2}) + f_v^{\mu_2}(1 - f_v^{\mu_1})] \sin^2\left(\frac{f}{J} \sin\frac{\beta}{2}\right) \quad (4.2.4.3)$$

$$\mathcal{F}_e(\mu_1, \mu_2, t) = \sum_{\{m_e\}} (-4)^{\frac{c(m_e)}{2}} \sin^{c(m_e)} \left( \frac{2f}{J} \sin\frac{\beta}{2} \right) \prod_{v \in \bar{m}_e} K_v \prod_{q \in m_e} (f_q^{\mu_1} - f_q^{\mu_2})$$

$$\mathcal{F}_o(\mu_1, \mu_2, t) = \sum_{\{m_o\}} (-4)^{\frac{c(m_o)-1}{2}} \sin^{c(m_o)} \left( \frac{2f}{J} \sin\frac{\beta}{2} \right) \prod_{v \in \bar{m}_o} K_v \prod_{q \in m_o} (f_q^{\mu_1} - f_q^{\mu_2})$$

and  $m = (m_1, m_2, \dots, m_s)$ ,  $s = 1, 2, \dots, N$  is a non-empty subset of the set  $r = (1, 2, \dots, N)$ ;  $c(m)$  is the number of elements of subset  $m$ .  $m_e$ ,  $m_o$

correspond to the  $m$ 's with even and odd numbers of elements, respectively.  $\bar{m} = r - m$ .  $f_n^{\mu_i} = \left[ \exp\left(\frac{\hbar\nu_n - \mu_i}{k_B T}\right) + 1 \right]^{-1}$ ,  $\hbar\nu_n = \varepsilon + 4t \cos(2n\pi/N)$ . So far, we have obtained the *exact* dynamics of spin qubits beyond the Markovian and weak qubit-bath coupling approximations. In the forthcoming discussion, we will focus on the non-Markovian and detailed-balance-breaking effects, reflected by the functions  $\mathcal{F}_e$  and  $\mathcal{F}_o$  which vanish under equilibrium condition  $\mu_1 = \mu_2$ .

### 4.2.5 Non-Markovian and nonequilibrium effects

Based on our exact dynamics obtained above, we are able to explicitly explore the non-Markovian process beyond the memorylessness under Markovian approximation. This becomes inapplicable when the following case is encountered: evolution of environment comparable to the subsystem timescale, which indicates that the back influence of system to bath is unignorable and the correlation function of the environment is colour rather than the white one. It recently attracted much attention in the study of dissipative quantum dynamics because the experimental measurements revealed the non-Markovian noise from the nonexponential decay of echo signal [169].

#### Non-Markovian mechanism

To measure the preservation of the quantum state, one can use the *fidelity* of the state defined as  $F(t) = \sqrt{\langle \Psi(0) | \rho_s(t) | \Psi(0) \rangle}$  if the system is initially in pure ensemble. Equivalently, the fidelity can be written as

$$F(t) = \sqrt{\frac{1}{2} + \cos\theta \operatorname{Re}\langle 1, 0 | \rho_s | 0, 1 \rangle + \sin\theta \operatorname{Im}\langle 1, 0 | \rho_s | 0, 1 \rangle} \quad (4.2.5.1)$$

which shows a strong correlation to the quantum coherence. According to recent experiments [154], the spin qubits is initially prepared at singlet state  $|\Psi_\pi(0)\rangle = \frac{1}{\sqrt{2}}(|1\rangle \otimes |0\rangle - |0\rangle \otimes |1\rangle)$ , ( $\theta = \pi$ ) in the regime of strong qubit-nuclear interaction, whose dynamical behaviors are illustrated in Fig.4.4. As is shown, the preservation of quantum state and revival of coherence are perfectly elucidated. Here we only show the behavior of the real part of coherence because it contributes to the preservation of state, based on Eq.(4.2.5.1). Physically the recovery of quantum coherence can be attributed to the non-Markovian effect, since the timescale of correlations in the environment is

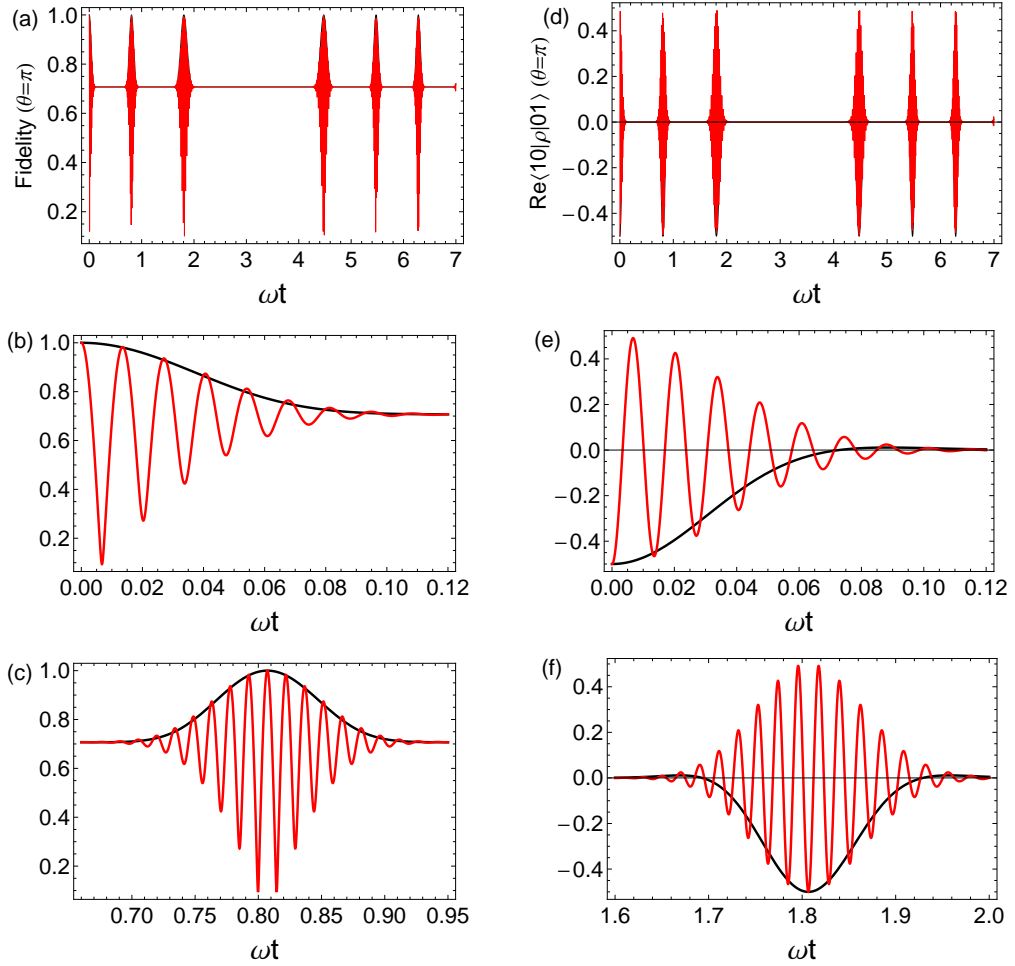


Figure 4.4: (Color online) Dynamics of (left) fidelity of quantum state  $|\Psi_\pi(0)\rangle = \frac{1}{\sqrt{2}}(|1\rangle \otimes |0\rangle - |0\rangle \otimes |1\rangle)$  and (right) the real part of coherence  $\text{Re}\langle 1,0|\rho_s|0,1\rangle$ . The red and black lines are for  $\mu_1 = 1.7$ ,  $\mu_2 = 0.5$  (far-from-equilibrium) and  $\mu_1 \simeq \mu_2 = 0.5$  (equilibrium), respectively. Other parameters are  $\varepsilon = 1$ ,  $t = 0.2$ ,  $k_B T = 0.1$ ,  $N = 100$  and  $f = 8J$ .

comparable to that of system and the phase correlation of the system has high chance to reconstruct. In contrast, the no-memory feature of system under Markovian approximation has no chance to recover its phase correlation in that the typical correlation time of environment is zero. The coherence always globally shows a monotonic decay until reaching the stationary value. Furthermore it is worthy to note that the system shows a perfect preservation of quantum state with fidelity of 100%. This feature can be alternatively understood from the coherence dynamics  $\text{Re}\langle 1, 0 | \rho_s | 0, 1 \rangle$ , shown in Fig.4.4(b), in which the magnitude of coherence periodically recovers to its initially value. The type of state protection we discuss here is completely different from what has been achieved by dynamical decoupling and other control methods. It is instead an intrinsic entanglement induced by slow relaxation of baths causing the non-Markovian process. This means no need to artificially control over the spin-spin interaction to combat decoherence.

Moreover, no global decay occurs for the local peaks of both coherence and fidelity with initially being engineered at Bell state, as compared to that in the case  $|\Psi_{\frac{\pi}{2}}(0)\rangle = \frac{1}{\sqrt{2}}(|1\rangle \otimes |0\rangle - i|0\rangle \otimes |1\rangle)$ , ( $\theta = \frac{\pi}{2}$ ) as shown in Supplementary Materials (SM) where such global decay does exist. This is because of the conservation of the total angular momentum in the case  $\theta = \pi$ :  $[L_z, H] = 0$  ( $|\Psi_{\pi}(0)\rangle$  is the eigenstate of total angular momentum  $L_z = \sigma_1^z + \sigma_2^z$ ).

To show the generality of the non-Markovian effect, we also perform the dynamics of fidelity and coherence as the spin qubits relax from another state  $|\Psi_{\frac{\pi}{2}}(0)\rangle = \frac{1}{\sqrt{2}}(|1\rangle \otimes |0\rangle - i|0\rangle \otimes |1\rangle)$ , ( $\theta = \frac{\pi}{2}$ ), whose dynamics is illustrated in SM. As is shown, the memory effect arising from the non-Markovian process always shows up, no matter which initial state is prepared. The generality of such non-Markovian effect is further demonstrated by letting the qubits to relax from other states, e.g.,  $|\Psi_{\frac{\pi}{4}}(0)\rangle = \frac{1}{\sqrt{2}}(|1\rangle \otimes |0\rangle + e^{-i\pi/4}|0\rangle \otimes |1\rangle)$  as shown in SM as well.

### **Enhancement of dynamical coherence from detailed-balance-breaking**

Now let us turn to the nonequilibrium effect with the detailed-balance-breaking induced by the gradient of chemical potential of nuclear spins. From our analytical solution to the density matrix we know that the nonequilibrium contribution is quantified by the factor  $\prod(f_q^{\mu_1} - f_q^{\mu_2})$  in the imbalance functions  $\mathcal{F}_e$  and  $\mathcal{F}_o$  which vanish under the detailed-balance. The time evolution shown in Fig.4.4 and the figure in SM in Ref.[104] illustrates that the

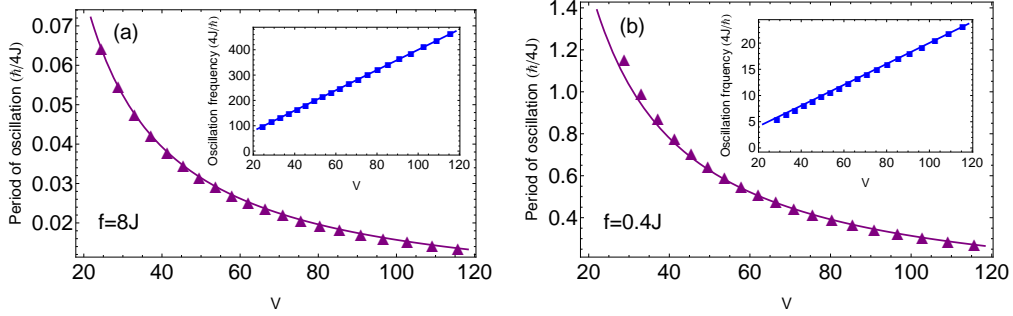


Figure 4.5: (Color online) (Large) Oscillation period and (Small) oscillation frequency vary as a function of effective voltage  $V$ , for (a) strong ( $f = 8J$ ) and (b) weak ( $f = 0.4J$ ) qubit-nuclear interactions; The triangle and square markers are for the numerical calculations of oscillation period and frequency, respectively. The smooth curves are obtained from the analytical result in Eq.(4.2.5.5). Other parameters are  $\varepsilon = 1$ ,  $t = 0.2$ ,  $k_B T = 0.1$  and  $N = 100$ .

nonequilibriumness causes the rapid oscillation, by comparing the red and black lines for far-from-equilibrium and equilibrium regimes, respectively. This in other words, reveals that the far-from-equilibrium is essential for observing the considerably coherent oscillation of spin qubits in the experiments. Later we will propose an experiment based on quantum simulation to simulate such effect.

To understand and explain the oscillation feature produced by the detailed-balance-breaking, we need to introduce the net current between the spin qubits which provides a measure to the degree of deviation from equilibrium. The current conservation gives  $\frac{d}{dt}\sigma_2^\dagger\sigma_2 = \hat{I}_{1\rightarrow 2} - \hat{I}_{2\rightarrow bath}$ . In our model the current from system to spin environment vanishes because of the Ising coupling between qubits and nuclear spins. Thus the net current reads

$$I_{1\rightarrow 2} = \frac{d}{dt}\langle\sigma_2^\dagger\sigma_2\rangle = \frac{4J}{\hbar}\text{Im}\langle 1, 0|\rho_s|0, 1\rangle \quad (4.2.5.2)$$

based on Heisenberg's equation. This coincides with curl quantum flux in our former work [31, 34], in that microscopically the current strongly correlates to the curl quantum flux, vanishing under detailed-balance-protection at steady state. However it does not necessarily vanish during the dynamical process owing to the self-consumption of energy or information in the system. As is shown by Eq.(4.2.5.2), the net current governed by the nonequilibriumness

generates the fast oscillation of coherence and fidelity of quantum state. This can be understood as follow: *the rapid oscillation of net current leads to the back and forth motion of spin wave between qubits, which results in the fast oscillation feature of coherence.* For an analogy, this is in the similar spirit of limit cycle behavior in classical stochastic processes [43, 44], driven by the curl flux breaking the detailed-balance at steady state, where a robust oscillation network can be observed [1, 45, 46].

To further explore such nonequilibrium effect, we will work under certain approximation where the nuclear spin environments evolve sufficiently slowly so that they can be well approximated by quasistatic ensembles, namely  $\frac{dS_{v,i}^z}{dt} \simeq 0$  on the typical timescales of electron spin dynamics, around a microsecond or less [170, 171, 172]. This gives rise to a highly non-Markovian bath comprised by the nuclear spins. Then the entire system can be approximately described by product state  $\rho(t) \simeq \rho_s(t) \otimes \rho_{nc}^{\mu_1} \otimes \rho_{nc}^{\mu_2}$ . From Heisenberg equation one has

$$\begin{aligned} \frac{d}{dt} (\sigma_1^+ \sigma_2^-) &= \frac{2J}{i\hbar} (\sigma_1^+ \sigma_1^- - \sigma_2^+ \sigma_2^-) + \frac{2f}{i\hbar} \sum_{v=1}^N \sigma_1^+ \sigma_2^- (S_{v,1}^z - S_{v,2}^z) \\ \frac{d}{dt} (\sigma_1^+ \sigma_1^-) &= \frac{2J}{i\hbar} (\sigma_1^+ \sigma_2^- - \sigma_2^+ \sigma_1^-) \\ \frac{d}{dt} (\sigma_2^+ \sigma_2^-) &= -\frac{2J}{i\hbar} (\sigma_1^+ \sigma_2^- - \sigma_2^+ \sigma_1^-) \end{aligned} \quad (4.2.5.3)$$

which gives rise to the following oscillation

$$\begin{aligned} \frac{d^2}{dt^2} \text{Im} \langle \sigma_1^+ \sigma_2^- \rangle + \frac{16J^2}{\hbar^2} \left( 1 + \frac{f^2 V^2}{4J^2} \right) \text{Im} \langle \sigma_1^+ \sigma_2^- \rangle &= 0 \\ V = \sum_{v=1}^N (\langle S_{v,1}^z \rangle - \langle S_{v,2}^z \rangle) &= 2 \sum_{v=1}^N (f_{\omega_v}^{\mu_1} - f_{\omega_v}^{\mu_2}) \end{aligned} \quad (4.2.5.4)$$

where  $V$  serves as an “effective voltage” vanishing under detailed-balance. Therefore the oscillation frequency of coherence is

$$\Omega = \frac{4J}{\hbar} \sqrt{1 + \frac{f^2 V^2}{4J^2}} \quad (4.2.5.5)$$

which uncovers the relation between the coherent oscillation and the nonequilibrium effect in a quantitative manner. It explicitly demonstrates that the

detailed-balance-breaking is intrinsic for the rapid oscillation of coherence and subsequently the fidelity of quantum state, which confirms our argument above. To verify the validity of our formula for  $\Omega$ , we propagate a numerical calculation of the oscillation period and frequency with respect to voltage  $V$ , illustrated in Fig.4.5, which shows a perfect agreement with our analytical formula Eq.(4.2.5.5).

It is worthy to point out that the fast coherent oscillation feature produced by nonequilibriumness is not only restricted into non-Markovian regime, but is also a phenomenon in general scenario. This is because the procedure for reaching Eq.(4.2.5.5) can be naively applied to the case under Markovian approximation. Hence in other words, one can conclude that the rapid coherent oscillation of quantum-state fidelity is a nonequilibrium phenomenon in general to be observed in spin arrays.

#### 4.2.6 Proposed experiment for realizing the dynamics of spin qubits

In order to observe the non-Markovian and nonequilibrium effects investigated before, ultracold trapped ions seems to be a good candidate to engineer our setup, since they are recently used for the spin chain simulations [173, 174, 175, 168].

The ions are usually confined by a linear RF trap with three-dimensional electrodes, which subsequently produces the internal levels of ions. The spin- $\frac{1}{2}$  structure is realized by choosing two nearly degenerate sublevels of the ground state, splitted by Zeeman field. On the other hand, the ions reside on individual lattice sites due to the strong Coulomb repulsion, which still leads to the common motional modes of ions described by phonons. Such phonons allow long-range interactions to be mediated between spins associated with the ions. To engineer the long-range spin-spin interactions, two detuning laser beams with different frequencies  $\omega_1, \omega_2$  are required to perform stimulated two-photon Raman transition between the sublevels, through a third level with higher energy, as shown in Fig.4.6(right). Here the two particular processes are crucial: (a) the transition  $|\uparrow\rangle|n'\rangle \Leftrightarrow |\downarrow\rangle|n\rangle$  ( $n' \neq n$ ) with two laser beams detuned by the frequency difference between these two states; (b) the transitions  $|\uparrow\rangle|n'\rangle \Leftrightarrow |\uparrow\rangle|n\rangle$  ( $n' \neq n$ ) and  $|\downarrow\rangle|n'\rangle \Leftrightarrow |\downarrow\rangle|n\rangle$  ( $n' \neq n$ ) with the two beams detuned by approximately the frequency of a motional mode. Here  $n', n$  denote the energy levels of ions. It can be directly shown that (a)

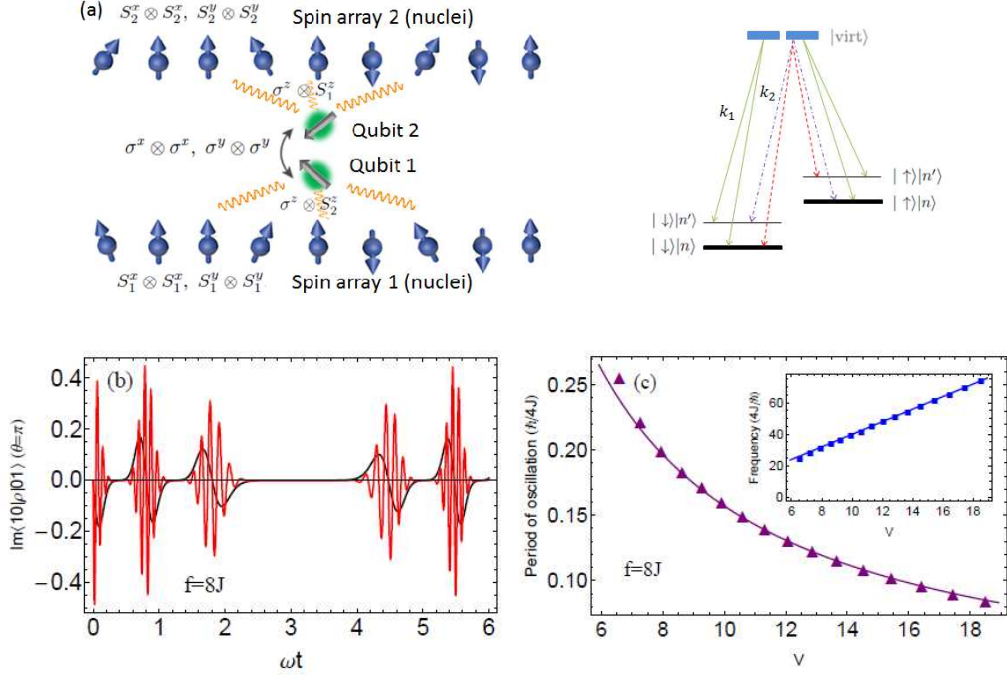


Figure 4.6: (Color online) (a) Schematics of (Left) our setup and (Right) the stimulated two-photon Raman transition for realizing (Red and blue)  $\sigma^x \otimes \sigma^x + \sigma^y \otimes \sigma^y$  and (Orange)  $\sigma^z \otimes \sigma^z$  interactions; (b) Dynamics of coherence  $\text{Im}\langle 1, 0 | \rho_s | 0, 1 \rangle$  with the initial condition  $|\Psi(0)\rangle = \frac{1}{\sqrt{2}}(|1\rangle \otimes |0\rangle - |0\rangle \otimes |1\rangle)$  and (c) the period (small for frequency) of coherent oscillation as a function of voltage  $V$ . The red and black lines in (a) are for  $\mu_1 = 2.22\text{GHz}$ ,  $\mu_2 = 0.65\text{GHz}$  (far-from-equilibrium) and  $\mu_1 \simeq \mu_2 = 0.65\text{GHz}$  (equilibrium), respectively; The triangle and square markers are for the numerical calculations of oscillation period and frequency, respectively. The smooth curves are obtained from Eq.(4.2.5.5). Other parameters are  $\varepsilon \simeq 1.31\text{GHz}$ ,  $t \simeq 0.26\text{GHz}$ ,  $T \simeq 1\text{mK}$ ,  $J \simeq 0.22\text{GHz}$ ,  $f \simeq 1.76\text{GHz}$  and  $N = 16$ .

generates the transversed long-range interactions between spins,  $\sigma^x \otimes \sigma^x$  and  $\sigma^y \otimes \sigma^y$  depending on the polarization of electric field, while (b) generates the Ising type of interaction,  $\sigma^z \otimes \sigma^z$  [176, 177].

The array of nuclear spins can be implemented by an array of  $N$  trapped ions, showing a dipolar decay of spin-spin interaction  $J_{ij} \sim \frac{1}{|i-j|^3}$ . In order to realize the XY couplings, the spin array is manipulated to interact with detuning laser beams in terms of process (a) above. We now prepare other two ions trapped by linear RF trap, with the same splitting between the sublevels of ground state as that in arrays of nuclear spins. The same technique is employed as before to produce the transversal spin-spin interaction between these two ions. To engineer the interaction between spin arrays and the two ions, the process (b) can be used to generate the individual coupling of ion 1(2) to each ion in the spin array 1(2), by choosing the  $\hat{z}$ -polarization of the electric field in the laser beams, illustrated by Fig.4.6(left). This in other words, indicates that  $2N$  pairs of detuning beams with  $\hat{z}$ -polarization are demanded in total, to simulate the qubit-nuclear interactions.

We use 16 trapped ions to simulate each nuclear spin environment, by taking into account the conditions in recent experiments [168, 174, 175]. The two arrays of ions are prepared initially with different fermi energies and the two ions (qubits) are engineered at singlet state  $|\Psi(0)\rangle = \frac{1}{\sqrt{2}}(|1\rangle \otimes |0\rangle - |0\rangle \otimes |1\rangle)$ . By choosing the parameters  $\varepsilon \simeq 1.31\text{GHz}$ ,  $t \simeq 0.26\text{GHz}$ ,  $T \simeq 1\text{mK}$ ,  $J \simeq 0.22\text{GHz}$ ,  $f \simeq 1.76\text{GHz}$ ,  $\mu_2 \simeq 0.65\text{GHz}$  and  $N = 16$ , Fig.4.6 shows the dynamics of coherence and also the behavior of frequency of coherent oscillation with respect to effective voltage as introduced before. The non-Markovian effect is clearly shown by the revival of the coherence in Fig.4.6(b). Moreover, it also shows the nonequilibrium effect (detailed-balance-breaking) which produces the fast coherent oscillation feature, by comparing the red and black curves. The dependence of oscillation period (frequency) is further illustrated in Fig.4.6(c), which is measurable in the proposed experiment.

### 4.2.7 Conclusion

In summary, we exactly and analytically solved the dynamics of spin qubits surrounded by the charge noise produced by nuclear spins. We found that the detailed-balance-breaking caused the rapid coherent oscillation in spin dynamics, which was lack in the conventional static ensemble of nuclear bath preserving detailed-balance, i.e., Overhauser noise. The analytical relationship between coherent oscillation frequency and effective voltage was

further obtained, which as a quantitative measure of the nonequilibrium effect, would be accessible in experiments. On the other hand, our results have the advantage of previous work in purely numerical manner for describing the non-Markovian process and thus predicting the recovery of coherence and the subsequent quantum-state preservation in a general scenario. These novel and spectacular effects we predict, especially the coherent oscillation arising from detailed-balance-breaking, can be observed in ultracold trapped ions we proposed in details in spirit of quantum simulation in the laboratory.

# Chapter 5

## Summary and conclusion

In this thesis, we first established a theoretical framework in terms of curl flux, to understand the relation between quantum nature, i.e., quantum coherence & entanglement, and nonequilibriumness. It was found that the far-from-equilibrium regime takes the advantage of promoting the steady-state coherence, rather than the near-to-equilibrium regime. For the dynamical relaxations, we demonstrated that the coherence has significant contribution to the typical timescales of both energy transport and dephasing, by examining the applicability of secular approximation. Furthermore we uncovered a general mechanism of how vibrational modes lead to the long-survived coherence, based on the effective field theory. This provides the explanation in the sense of generality to the long-lived electronic coherence recently observed in some molecular aggregates.

Finally we investigated the relaxation of electronic spin arrays coupled to nuclear-spin baths with chemical potential gradient. This is motivated by the recent exploration of decoherence mechanism in the solid-device based quantum computation. The nonequilibrium-induced rapid oscillation of coherence and quantum entanglement was uncovered and the origin of this phenomenon was further analyzed.

# Bibliography

- [1] J. Wang, L. Xu and E. K. Wang. “Potential landscape and flux framework of nonequilibrium networks: Robustness, dissipation, and coherence of biochemical oscillations”. *Proc. Natl. Acad. Sci. U.S.A.*, **105**: 12271, 2008.
- [2] W. M. Gelbart, S. A. Rice and K. F. Freed. “Random matrix theory and the master equation for finite systems”. *J. Chem. Phys.*, **57**: 4699, 1972.
- [3] M. Esposito, U. Harbola and S. Mukamel. “Nonequilibrium fluctuations, fluctuation theorems, and counting statistics in quantum systems”. *Rev. Mod. Phys.*, **81**: 1665, 2009.
- [4] A. M. Kuznetsov and J. Ulstrup. *Electron Transfer in Chemistry and Biology: An Introduction to the Theory*. Chichester-Wiley, United Kingdom, 1999.
- [5] R. S. Shishir, F. Chen, J. Xia, N. J. Tao and D. K. Ferry. “Theory and measurements of room temperature transport in graphene using SiO<sub>2</sub> backgate and electrochemical gate”. *J. Vac. Sci. Technol. B*, **27**: 2003, 2009.
- [6] G. Baym, H. Monien, C. J. Pethick and D. G. Ravenhall. “Transverse interactions and transport in relativistic quark-gluon and electromagnetic plasmas”. *Phys. Rev. Lett.*, **64**: 1867, 1990.
- [7] M. A. Reed, C. Zhou, C. J. Muller, T. P. Burgin and J. M. Tour. “Conductance of a molecular junction”. *Science*, **278**: 252, 1997.
- [8] P. G. Wolynes. “Some quantum weirdness in physiology”. *Proc. Natl. Acad. Sci. U.S.A.*, **106**: 17247, 2009.

- [9] R. van Grondelle and V. I. Novoderezhkin. “Energy transfer in photosynthesis: experimental insights and quantitative models”. *Phys. Chem. Chem. Phys.*, **8**: 793, 2006.
- [10] H. Park, J. Park, A. K. L. Lim, E. H. Anderson, A. P. Alivisatos and P. L. Mceuen. “Nanomechanical oscillations in a single-C<sub>60</sub> transistor”. *Nature*, **407**: 57, 2000.
- [11] W. W. Parson. “Long live electronic coherence!”. *Science*, **316**: 1438, 2007.
- [12] A. Ishizaki and G. R. Fleming. “Quantum coherence in Photosynthetic Light Harvesting”. *Annu. Rev. Condens. Matter Phys.*, **3**: 333, 2012.
- [13] E. Collini, C. Y. Wong, K. E. Wilk, P. M. G. Curmi, P. Brumer and G. D. Scholes. “Coherently wired light-harvesting in photosynthetic marine algae at ambient temperature”. *Nature*, **463**: 644, 2010.
- [14] G. Panitchayangkoon, D. Hayes, K. A. Fransted, J. R. Caram, E. Harel, J. Wen, R. E. Blankenship and G. S. Engel. “Long-lived quantum coherence in photosynthetic complexes at physiological temperature”. *Proc. Natl. Acad. Sci. U.S.A.*, **107**: 12766, 2010.
- [15] S. Mukamel K. E. Dorfman, D. V. Voronine and M. O. Scully. “Photosynthetic reaction center as a quantum heat engine”. *Proc. Natl. Acad. Sci. U.S.A.*, **110**: 2746, 2013.
- [16] D. Nagy and P. Domokos. “Nonequilibrium quantum criticality and non-Markovian environment: Critical exponent of a quantum phase transition”. *Phys. Rev. Lett.*, **115**: 043601, 2015.
- [17] V. M. Bastidas, C. Emary, B. Regler and T. Brandes. “Nonequilibrium quantum phase transitions in the Dicke model”. *Phys. Rev. Lett.*, **108**: 043003, 2012.
- [18] S. Sachdev. *Quantum Phase Transition, 2nd edn.* Cambridge University Press, United Kingdom, 2011.
- [19] S. L. Sondhi, S. M. Girvin, J. P. Carini and D. Shahar. “Continuous quantum phase transitions”. *Rev. Mod. Phys.*, **69**: 315, 1997.

- [20] M. Vojta. “Quantum phase transitions”. *Rep. Prog. Phys.*, **66**: 2069, 2003.
- [21] M. O. Scully and M. S. Zubairy. *Quantum Optics*. Cambridge University Press, Cambridge; United Kingdom, 1997.
- [22] H.-P. Breuer and F. Petruccione. *The Theory of Open Quantum Systems*. Oxford University Press, Oxford; United Kingdom, 2007.
- [23] G. S. Engel, T. R. Calhoun, E. L. Read, T. K. Ahn, T. Mancal, Y.-C. Cheng, R. E. Blankenship and G. R. Fleming. “Evidence for wave-like energy transfer through quantum coherence in photosynthetic systems”. *Nature*, **446**: 782, 2007.
- [24] D. Hayes, J. Wen, G. Panitchayangkoon, R. E. Blankenship and G. S. Engel. “Robustness of electronic coherence in the Fenna-Matthews-Olson complex to vibronic and structural modifications”. *Faraday Discuss.*, **150**: 459, 2011.
- [25] E. Harel and G. S. Engel. “Quantum coherence spectroscopy reveals complex dynamics in bacterial light-harvesting complex 2 (LH2)”. *Proc. Natl. Acad. Sci. U.S.A.*, **109**: 706, 2012.
- [26] A. W. Chin, J. Prior, R. Rosenbach, F. Caycedo-Soler, S. F. Huelga and M. B. Plenio. “The role of non-equilibrium vibrational structures in electronic coherence and recoherence in pigmentprotein complexes”. *Nat. Phys.*, **9**: 113, 2013.
- [27] N. Christensson, H. F. Kauffmann, T. Pullerits and T. Mancal. “Origin of long-lived coherences in light-harvesting complexes”. *J. Phys. Chem. B*, **116**: 7449, 2012.
- [28] E. J. O’Reilly and A. Olaya-Castro. “Non-classicality of the molecular vibrations assisting exciton energy transfer at room temperature”. *Nat. Commun.*, **5**: 3012, 2014.
- [29] V. Tiwari, W. K. Peters and D. M. Jonas. “Electronic resonance with anticorrelated pigment vibrations drives photosynthetic energy transfer outside the adiabatic framework”. *Proc. Natl. Acad. Sci. U.S.A.*, **110**: 1203, 2013.

- [30] J. M. Womick and A. M. Moran. “Vibronic enhancement of exciton sizes and energy transport in photosynthetic complexes”. *J. Phys. Chem. B*, **115**: 1347, 2011.
- [31] Z. D. Zhang and J. Wang. “Curl flux, coherence, and population landscape of molecular systems: Nonequilibrium quantum steady state, energy (charge) transport, and thermodynamics”. *J. Chem. Phys.*, **140**: 245101, 2014.
- [32] Z. D. Zhang and J. Wang. “Landscape, kinetics, paths and statistics of curl flux, coherence, entanglement and energy transfer in nonequilibrium quantum systems”. *New J. Phys.*, **17**: 043053, 2015.
- [33] Z. D. Zhang and J. Wang. “Shape, orientation and magnitude of the curl quantum flux, the coherence and the statistical correlations in energy transport at nonequilibrium steady state”. *New J. Phys.*, **17**: 093021, 2015.
- [34] Z. D. Zhang and J. Wang. “Vibrational and coherence dynamics of molecules”. *Phys. Chem. Chem. Phys.*, **17**: 23754, 2015.
- [35] Z. D. Zhang and J. Wang. “Origin of long-lived quantum coherence and excitation dynamics in pigment-protein complexes”. *Submitted to Sci. Rep.*, 2016.
- [36] A. M. Tyryshkin, S. A. Lyon, A. V. Astashkin and A. M. Raitsirmring. “Electron spin relaxation times of phosphorus donors in silicon”. *Phys. Rev. B*, 68:193207, 2003.
- [37] J. Clarke and F. K. Wilhelm. “Superconducting quantum bits”. *Nature*, 453:1031, 2008.
- [38] D. Press, T. Ladd, B. Zhang and Y. Yamamoto. “Complete quantum control of a single quantum dot spin using ultrafast optical pulses”. *Nature*, **456**: 218, 2008.
- [39] F. H. L. Koppens, J. A. Folk, J. M. Elzerman, R. Hanson, L. H. W. van Beveren, I. T. Vink, H. P. Tranitz, W. Wegscheider, L. P. Kouwenhoven and L. M. K. Vandersypen. “Control and detection of Singlet-Triplet mixing in a random nuclear field”. *Science*, **309**: 1346, 2005.

- [40] S. Foletti, H. Bluhm, D. Mahalu, V. Umansky and A. Yacoby. “Universal quantum control of two-electron spin quantum bits using dynamic nuclear polarization”. *Nat. Phys.*, **5**: 903, 2009.
- [41] C. Barthel, D. J. Reilly, C. M. Marcus, M. P. Hanson and A. C. Gosard. “rapid single-shot measurement of a Singlet-Triplet qubit”. *Phys. Rev. Lett.*, **103**: 160503, 2009.
- [42] H. Risken. *The Fokker-Planck Equation: Methods of Solution and Applications*. Springer, New York, 1989.
- [43] G. Hu, T. Ditzinger, C. Z. Ning and H. Haken. “Stochastic resonance without external periodic force”. *Phys. Rev. Lett.*, **71**: 807, 1993.
- [44] W. J. Rappel and S. H. Strogatz. “Stochastic resonance in an autonomous system with a nonuniform limit cycle”. *Phys. Rev. E*, **50**: 3249, 1994.
- [45] D. Schultz, E. B. Jacob, J. N. Onuchic and P. G. Wolynes. “Molecular level stochastic model for competence cycles in *bacillussubtilis*”. *Proc. Natl. Acad. Sci. U.S.A.*, **104**: 17582, 2007.
- [46] C. H. Li, E. K. Wang and J. Wang. “Potential flux landscapes determine the global stability of a lorenz chaotic attractor under intrinsic fluctuations”. *J. Chem. Phys.*, **136**: 194108, 2012.
- [47] L. D. Landau. *Mechanics, Vol. 1 (Course of Theoretical Physics)*. Butterworth-Heinemann, Oxford, 1987.
- [48] M. Qian and Z. T. Hou. *Reversible Markov Process*. Hunan Scientific Publisher, Changsha, 1979.
- [49] L. D. Landau. *Quantum Mechanics (Non-relativistic Theory)*. Reed Educational and Professional Publishing Ltd., Oxford; United Kingdom, 1977.
- [50] E. M. Lifshitz L. D. Landau and L. P. Pitaevskij. *Statistical Physics (Part 2: Theory of the Condensed State), Vol. 9 (Course of Theoretical Physics)*. Butterworth-Heinemann, Oxford, 1987.

- [51] Z. Zhu and R. A. Marcus. “On collisional energy transfer in recombination and dissociation reactions: A wienerhopf problem and the effect of a near elastic peak”. *J. Chem. Phys.*, **129**: 214106, 2008.
- [52] H. Qian. “Open-system nonequilibrium steady state: Statistical thermodynamics, fluctuations, and chemical oscillations”. *J. Phys. Chem. B*, **110**: 15063, 2006.
- [53] H. Qian. “Entropy demystified the thermodynamics of stochastically fluctuating systems”. *Methods Enzymol.*, **467**: 111, 2009.
- [54] J. Ye, K. Sun, Y. Zhao, Y. Yu, C. K. Lee and J. Cao. “Excitonic energy transfer in light-harvesting complexes in purple bacteria”. *J. Chem. Phys.*, **136**: 245104, 2009.
- [55] J. Wu, F. Liu, J. Ma, R. J. Silbey and J. Cao. “Efficient energy transfer in light-harvesting systems: Quantum-classical comparison, flux network, and robustness analysis”. *J. Chem. Phys.*, **137**: 174111, 2012.
- [56] S. A. Getty, C. Engtrakul, L. Wang, R. Liu, S. H. Ke, H. U. Baranger, W. Yang, M. S. Fuhrer and L. R. Sita. “Near-perfect conduction through a ferrocene-based molecular wire”. *Phys. Rev. B*, **71**: 241401, 2005.
- [57] I. Kassal, J. Y. Zhou and S. R. Keshari. “does coherence enhance transport in photosynthesis ?”. *J. Phys. Chem. Lett.*, **4**: 362, 2013.
- [58] F. Fassioli, R. Dinshaw, P. C. Arpin and G. D. Scholes. “Photosynthetic light harvesting: Excitons and coherence”. *J. R. Soc. Interface*, **11**: 20130901, 2014.
- [59] D. Manzano, M. Tiersch, A. Asadian and H. J. Briegel. “Quantum transport efficiency and Fourier’s law”. *Phys. Rev. E*, **86**: 061118, 2012.
- [60] F. Chen and N. J. Tao. “Electron transport in single molecules: From Benzene to Graphene”. *Acc. Chem. Res.*, **42**: 429, 2009.
- [61] Z. D. Zhang and J. Wang. “Assistance of molecular vibrations on coherent energy transfer in photosynthesis from the view of a quantum heat engine”. *J. Phys. Chem. B*, **119**: 4662, 2015.

- [62] P. W. Anderson. “Absence of diffusion in certain random lattices”. *Phys. Rev.*, **109**: 1492, 1958.
- [63] M. Segev, Y. Silberberg and D. N. Christodoulides. “Anderson localization of light”. *Nat. Photonics*, **7**: 197, 2013.
- [64] B. Kramer and A. MacKinnon. “Localization: theory and experiment”. *Rep. Prog. Phys.*, **56**: 1469, 1993.
- [65] U. Harbola, M. Esposito and S. Mukamel. “Quantum master equation for electron transport through quantum dots and single molecules”. *Phys. Rev. B*, **74**: 235309, 2006.
- [66] R. J. Glauber. “Coherent and incoherent states of the radiation field”. *Phys. Rev.*, **131**: 2766, 1963.
- [67] E. C. G. Sudarshan. “Equivalence of semiclassical and quantum mechanical descriptions of statistical light beams”. *Phys. Rev. Lett.*, **10**: 277, 1963.
- [68] L. Mandel and E. Wolf. *Optical Coherence and Quantum Optics*. Cambridge University Press, United Kingdom, 1995.
- [69] M. Greiner, C. A. Regal, J. T. Stewart and D. S. Jin. “Probing pair-correlated Fermionic atoms through correlations in atom shot noise”. *Phys. Rev. Lett.*, **94**: 110401, 2005.
- [70] S. Manz, R. Bücker, T. Betz, C. Koller, S. Hofferberth, I. E. Mazets, A. Imambekov, E. Demler, A. Perrin, J. Schmiedmayer and T. Schumm. “Two-point density correlations of quasicondensates in free expansion”. *Phys. Rev. A*, **81**: 031610(R), 2010.
- [71] A. Olaya-Castro, C. F. Lee, F. F. Olsen and N. F. Johnson. “Efficiency of energy transfer in a light-harvesting system under quantum coherence”. *Phys. Rev. B*, **78**: 085115, 2008.
- [72] M. Mohseni, P. Rebentrost, S. Lloyd and A. Aspuru-Guzik. “Environment-assisted quantum walks in photosynthetic energy transfer”. *J. Chem. Phys.*, **129**: 174106, 2008.

- [73] P. Reberntrost, M. Mohseni, I. Kassal, S. Lloyd and A. Aspuru-Guzik. “Environment-assisted quantum transport”. *New J. Phys.*, **11**: 033003, 2009.
- [74] J. J. Mendoza-Arenas, T. Grujic, D. Jaksch and S. R. Clark. “Dephasing enhanced transport in nonequilibrium strongly correlated quantum systems”. *Phys. Rev. B*, **87**: 235130, 2013.
- [75] Z. Zhang, L. Piatkowski, H. J. Bakker and M. Bonn. “Ultrafast vibrational energy transfer at the water/air interface revealed by two-dimensional surface vibrational spectroscopy”. *Nat. Chem.*, **3**: 888, 2011.
- [76] F. H. L. Koppens, C. Buizert, K. J. Tielrooij, I. T. Vink, K. C. Nowack, T. Meunier, L. P. Kouwenhoven and L. M. K. Vandersypen. “Driven coherent oscillations of a single electron spin in a quantum dot”. *Nature*, **442**: 766, 2006.
- [77] J. Yoneda, T. Otsuka, T. Nakajima, T. Takakura, T. Obata, M. Pioro-Ladriere, H. Lu, C. J. Palmstrom, A. C. Gossard and S. Tarucha. “Fast electrical control of single electron spins in quantum dots with vanishing influence from nuclear spins”. *Phys. Rev. Lett.*, **113**: 267601, 2014.
- [78] A. J. Nozik. “Spectroscopy and hot electron relaxation dynamics in semiconductor quantum wells and quantum dots”. *Annu. Rev. Phys. Chem.*, **52**: 193, 2001.
- [79] D. P. Simpson, D. M. Gangardt, I. V. Lerner and P. Krüger. “One-dimensional transport of bosons between weakly linked reservoirs”. *Phys. Rev. Lett.*, **112**: 100601, 2014.
- [80] R. Härtle and M. Kulkarni. “Effect of broadening in the weak-coupling limit of vibrationally coupled electron transport through molecular junctions and the analogy to quantum dot circuit QED systems”. *Phys. Rev. B*, **91**: 245429, 2015.
- [81] D. Stadler, S. Krinner, J. Meineke, J. P. Brantut and T. Esslinger. “Observing the drop of resistance in the flow of a superfluid Fermi gas”. *Nature*, **491**: 736, 2012.

- [82] D. J. Papoular, L.P. Pitaevskii and S. Stringari. “Quantized conductance with bosonic atoms”. *arXiv:1510.02618*, 2015.
- [83] T. Förster. “Energiewanderung und fluoreszenz”. *Naturwissenschaften*, **6**: 166, 1946.
- [84] T. Förster. “Zwischenmolekulare energiewanderung und fluoreszenz”. *Ann. Phys.*, **437**: 55, 1948.
- [85] B. Palmieri, D. Abramavicius and S. Mukamel. “Lindblad equations for strongly coupled populations and coherences in photosynthetic complexes”. *J. Chem. Phys.*, **130**: 204512, 2009.
- [86] S. Woutersen and H. J. Bakker. “Resonant intermolecular transfer of vibrational energy in liquid water”. *Nature*, **402**: 507, 1999.
- [87] S. Woutersen, U. Emmerichs and H. J. Bakker. “Femtosecond mid-IR pump-probe spectroscopy of liquid water: Evidence for a two-component structure”. *Science*, **278**: 658, 1997.
- [88] J. A. McGuire and Y. R. Shen. “Ultrafast vibrational dynamics at water interfaces”. *Science*, **313**: 1945, 2006.
- [89] Q. Du, E. Freysz and Y. R. Shen. “Surface vibrational spectroscopic studies of hydrogen bonding and hydrophobicity”. *Science*, **264**: 826, 1994.
- [90] H. J. Carmichael. *Statistical Methods in Quantum Optics 1: Master Equations and Fokker-Planck Equations*. Springer, New York, 1999.
- [91] B. Ruggiero, P. Delsing, C. Granata, Y. A. Pashkin and P. Silvestrini. *Quantum Computing in Solid State Systems*. Springer, New York, 2006.
- [92] R. E. Fenna and B. W. Matthews. “Chlorophyll arrangement in a bacteriochlorophyll protein from *chlorobium limicola*”. *Nature*, **258**: 573, 1975.
- [93] A. Ishizaki, T. R. Calhoun, G. S. Schlau-Cohen and G. R. Fleming. “Quantum coherence and its interplay with protein environments in photosynthetic electronic energy transfer”. *Phys. Chem. Chem. Phys.*, **12**: 7319, 2010.

- [94] H. Lee, Y. C. Cheng and G. R. Fleming. “Coherence dynamics in photosynthesis: Protein protection of excitonic coherence”. *Science*, **316**: 1462, 2007.
- [95] A. Ishizaki and G. R. Fleming. “Theoretical examination of quantum coherence in a photosynthetic system at physiological temperature”. *Proc. Natl. Acad. Sci. U.S.A.*, **106**: 17255, 2009.
- [96] D. E. Logan and P. G. Wolynes. “Quantum localization and energy flow in many-dimensional Fermi resonant systems”. *J. Chem. Phys.*, **93**: 4994, 1990.
- [97] E. U. Condon. “The Frank-Condon principle and related topics”. *Am. J. Phys.*, **15**: 365, 1947.
- [98] B. Hein, C. Kreisbeck, T. Kramer and M. Rodriguez. “Modelling of oscillations in two-dimensional echo-spectra of the Fenna-Matthews-Olson complex”. *New J. Phys.*, **14**: 023018, 2012.
- [99] M. B. Plenio, J. Almeida and S. F. Huelga. “Origin of long-lived oscillations in 2D-spectra of a quantum vibronic model: Electronic vs vibrational coherence”. *J. Chem. Phys.*, **139**: 235102, 2013.
- [100] E. Romero, R. Augulis, V. I. Novoderezhkin, M. Ferretti, J. Thieme, D. Zigmantas and R. van Grondelle. “Quantum coherence in photosynthesis for efficient solar-energy conversion”. *Nat. Phys.*, **10**: 676, 2014.
- [101] K. Huang and A. Rhys. “Theory of light absorption and non-radiative transition in F-centers”. *Proc. Roy. Soc. A*, **204**: 406, 1950.
- [102] Y. Gu, A. Widom and P. M. Champion. “Spectral line shapes of damped quantum oscillators: Applications to biomolecules”. *J. Chem. Phys.*, **100**: 2547, 1994.
- [103] Z. D. Zhang, G. E. Astrakharchik, D. C. Aveline, S. Choi, H. Perrin, T. H. Bergeman and M. Olshanii. “Breakdown of scale invariance in the vicinity of the Tonks-Girardeau limit”. *Phys. Rev. A*, **89**: 063616, 2014.
- [104] Z. D. Zhang, H. C. Fu and J. Wang. “Nonequilibrium-induced enhancement of dynamical quantum coherence of spin arrays in the presence of noisy environments”. *Submitted to Nat. Commun.*, 2016.

- [105] E. H. Lieb. “Exact analysis of an interacting bose gas. II. the excitation spectrum”. *Phys. Rev.*, **130**: 1616, 1963.
- [106] E. H. Lieb and W. Liniger. “Exact analysis of an interacting bose gas. I. the general solution and the ground state”. *Phys. Rev.*, **130**: 1605, 1963.
- [107] Kerson Huang, C. N. Yang and J. M. Luttinger. “Imperfect bose gas with hard-sphere interaction”. *Phys. Rev.*, **105**: 776, 1957.
- [108] T. D. Lee, Kerson Huang and C. N. Yang. “Eigenvalues and eigenfunctions of a bose system of hard spheres and its low-temperature properties”. *Phys. Rev.*, **106**: 1135, 1957.
- [109] Kerson Huang. *Statistical Mechanics*. John Wiley & Sons, Inc., New York, 1987.
- [110] C. J. Pethick and H. Smith. *Bose-Einstein Condensation in Dilute Gases*. Cambridge University Press, Cambridge, UK, 2002.
- [111] M. Olshanii. “Atomic scattering in the presence of an external confinement and a gas of impenetrable bosons”. *Phys. Rev. Lett.*, **81**: 938, 1998.
- [112] T. H. Bergeman, M. G. Moore and M. Olshanii. “Atom-atom scattering under cylindrical harmonic confinement: Numerical and analytic studies of the confinement induced resonance”. *Phys. Rev. Lett.*, **91**: 163201, 2003.
- [113] M. Girardeau. “Relationship between systems of impenetrable bosons and fermions in one dimension”. *J. Math. Phys.*, **1**: 516, 1960.
- [114] T. Kinoshita, T. Wenger and D. S. Weiss. “Observation of a one-dimensional Tonks-Girardeau gas”. *Science*, **305**: 1125, 2004.
- [115] B. Paredes, A. Widera, V. Murg, O. Mandel, S. Fölling, I. Cirac, G. V. Shlyapnikov, T. W. Hänsch and I. Bloch. “Tonks-Girardeau gas of ultracold atoms in an optical lattice”. *Nature*, **429**: 277, 2004.
- [116] K. M. O’Hara, S. L. Hemmer, M. E. Gehm, S. R. Granade and J. E. Thomas. “Observation of a strongly interacting degenerate Fermi gas of atoms”. *Science*, **298**: 2179, 2002.

- [117] M. E. Gehm, S. L. Hemmer, S. R. Granade, K. M. O’Hara and J. E. Thomas. “Mechanical stability of a strongly interacting Fermi gas of atoms”. *Phys. Rev. A*, **68**: 011401(R), 2003.
- [118] T. Bourdel, J. Cubizolles, L. Khaykovich, K. M. F. Magalhaes, S. J. J. M. F. Kokkelmans, G. V. Shlyapnikov and C. Salomon. “Measurement of the interaction energy near a Feshbach resonance in a  $^6\text{Li}$  Fermi gas”. *Phys. Rev. Lett.*, **90**: 020402, 2003.
- [119] S. Gupta, Z. Hadzibabic, M. W. Zwierlein, C. A. Stan, K. Dieckmann, C. H. Schunck, E. G. M. van Kempen, B. J. Verhaar and W. Ketterle. “Radio-frequency spectroscopy of ultracold fermions”. *Science*, **300**: 1723, 2003.
- [120] C. A. Regal and D. S. Jin. “Measurement of positive and negative scattering lengths in a Fermi gas of atoms”. *Phys. Rev. Lett.*, **90**: 230404, 2003.
- [121] C. L. Hung, X. B. Zhang, N. Gemelke and C. Chin. “Observation of scale invariance and universality in two-dimensional Bose gases”. *Nature*, **470**: 236, 2012.
- [122] F. Chevy, V. Bretin, P. Rosenbusch, K. W. Madison and J. Dalibard. “Transverse breathing mode of an elongated Bose-Einstein Condensate”. *Phys. Rev. Lett.*, **88**: 250402, 2002.
- [123] E. Vogt, M. Feld, B. Frohlich, D. Pertot, M. Koschorreck and M. Kohl. “Scale invariance and viscosity of a two-dimensional Fermi gas”. *Phys. Rev. Lett.*, **108**: 070404, 2012.
- [124] L. P. Pitaevskii and A. Rosch. “Breathing modes and hidden symmetry of trapped atoms in two dimensions”. *Phys. Rev. A*, **55**: R853(R), 1997.
- [125] M. Olshanii, H. Perrin and V. Lorent. “Example of a quantum anomaly in the physics of ultracold gases”. *Phys. Rev. Lett.*, **105**: 095302, 2010.
- [126] E. Taylor and M. Randeria. “Apparent low-energy scale invariance in two-dimensional Fermi gases”. *Phys. Rev. Lett.*, **109**: 135301, 2012.
- [127] J. Hofmann. “Quantum anomaly, universal relations, and breathing mode of a two-dimensional Fermi gas”. *Phys. Rev. Lett.*, **108**: 185303, 2012.

- [128] K. Merloti, R. Dubessy, L. Longchambon, M. Olshanii and H. Perrin. “Breakdown of scale invariance in a quasi-two-dimensional Bose gas due to the presence of the third dimension”. *Phys. Rev. A*, **88**: 061603(R), 2013.
- [129] V. Dunjko, V. Lorent and M. Olshanii. “Bosons in cigar-shaped traps: Thomas-Fermi regime, Tonks-Girardeau regime, and in between”. *Phys. Rev. Lett.*, **86**: 5413, 2001.
- [130] C. Menotti and S. Stringari. “Collective oscillations of a one-dimensional trapped Bose-Einstein gas”. *Phys. Rev. A*, **66**: 043610, 2002.
- [131] E. Haller, M. Gustavsson, M. Mark, J. Danzl, R. Hart, G. Pupillo and H.-C. Nägerl. “Realization of an excited, strongly correlated quantum gas phase”. *Science*, **325**: 1224, 2009.
- [132] M. Olshanii. *Back-of-the-Envelope Quantum Mechanics: With Extension to Many-Body Systems and Integral PDEs*. World Scientific, Singapore, 2013.
- [133] F. N. C. Paraan and V. E. Korepin. “Perturbative correction to the ground-state properties of one-dimensional strongly interacting bosons in a harmonic trap”. *Phys. Rev. A*, **82**: 065603, 2010.
- [134] Z. Q. Ma and C. N. Yang. “Spinless bosons in a 1D harmonic trap with repulsive delta function interparticle interaction I: General theory”. *Chin. Phys. Lett.*, **26**: 120506, 2009.
- [135] Z. Q. Ma and C. N. Yang. “Spinless bosons in a 1D harmonic trap with repulsive delta function interparticle interaction II: Numerical solutions”. *Chin. Phys. Lett.*, **27**: 020506, 2010.
- [136] E. B. Kolomeisky, T. J. Newman, J. P. Straley and X. Qi. “Low-dimensional Bose liquids: Beyond the Gross-Pitaevskii approximation”. *Phys. Rev. Lett.*, **85**: 1146, 2000.
- [137] T. Cheon and T. Shigehara. “Fermion-boson duality of one-dimensional quantum particles with generalized contact interactions”. *Phys. Rev. Lett.*, **82**: 2536, 1999.

- [138] V. Yukalov and M. Girardeau. “Fermi-Bose mapping for one-dimensional Bose gas”. *Laser Phys. Lett.*, **2**: 375, 2005.
- [139] M. Girardeau and M. Olshanii. “Theory of spinor Fermi and Bose gases in tight atom waveguides”. *Phys. Rev. A*, **70**: 023608, 2004.
- [140] J. Brand and A. Yu. Cherny. “Dynamic structure factor of the one-dimensional Bose gas near the Tonks-Girardeau limit”. *Phys. Rev. A*, **72**: 033619, 2005.
- [141] A. Yu. Cherny and J. Brand. “Polarizability and dynamic structure factor of the one-dimensional Bose gas near the Tonks-Girardeau limit at finite temperatures”. *Phys. Rev. A*, **73**: 023612, 2006.
- [142] Seba. “Some remarks on the  $\delta'$ -interaction in one dimension”. *Rep. Math. Phys.*, **24**: 111, 1986.
- [143] Kohn. “Cyclotron resonance and de Haas-van Alphen oscillations of an interacting electron gas”. *Phys. Rev.*, **123**: 1242, 1961.
- [144] T. Busch, B. G. Englert, K. Rzazewski and M. Wilkens. “Two cold atoms in a harmonic trap”. *Found. Phys.*, **28**: 549, 1998.
- [145] G. Astrakharchik. “Local density approximation for a perturbative equation of state”. *Phys. Rev. A*, **72**: 063620, 2005.
- [146] L. P. Pitaevskii and S. Stringari. “Elementary excitations in trapped Bose-Einstein condensed gases beyond the mean-field approximation”. *Phys. Rev. Lett.*, **81**: 4541, 1998.
- [147] L. D. Landau and E. Lifshitz. *Fluid Mechanics, Vol. 6 (Course of Theoretical Physics)*. Butterworth-Heinemann, Oxford, 1987.
- [148] K. Gunter, T. Stoferle, H. Moritz, M. Kohl and T. Esslinger. “ $p$ -wave interactions in low-dimensional fermionic gases”. *Phys. Rev. Lett.*, **95**: 230401, 2005.
- [149] B. E. Granger and D. Blume. “Tuning the interactions of spin-polarized fermions using quasi-one-dimensional confinement”. *Phys. Rev. Lett.*, **92**: 133202, 2004.

- [150] C. A. Regal, C. Ticknor, J. L. Bohn and D. S. Jin. “Tuning  $p$ -wave interactions in an ultracold Fermi gas of atoms”. *Phys. Rev. Lett.*, **90**: 053201, 2003.
- [151] J. P. Gaebler, J. T. Stewart, J. L. Bohn and D. S. Jin. “ $p$ -wave Feshbach molecules”. *Phys. Rev. Lett.*, **98**: 200403, 2007.
- [152] P. Maletinsky, S. Hong, M. S. Grinolds, B. Hausmann, M. D. Lukin, R. L. Walsworth, M. Loncar and A. Yacoby. “A robust scanning diamond sensor for nanoscale imaging with single nitrogen-vacancy centres”. *Nanotechnol.*, **7**: 320, 2012.
- [153] J. R. Petta, A. C. Johnson, J. M. Taylor, E. A. Laird, A. Yacoby, M. D. Lukin, C. M. Marcus, M. P. Hanson and A. C. Gossard. “Coherent manipulation of coupled electron spins in semiconductor quantum dots”. *Science*, **309**: 2180, 2005.
- [154] H. Bluhm, S. Foletti, I. Neder, M. Rudner, D. Mahalu, V. Umansky and A. Yacoby. “Dephasing time of GaAs electron-spin qubits coupled to a nuclear bath exceeding  $200\mu\text{s}$ ”. *Nat. Phys.*, **7**: 109, 2011.
- [155] J. Levy. “Universal quantum computation with spin-1/2 pairs and Heisenberg exchange”. *Phys. Rev. Lett.*, **89**: 147902, 2002.
- [156] G. S. Uhrig. “Keeping a quantum bit alive by optimized  $\pi$ -pulse sequences”. *Phys. Rev. Lett.*, **98**: 100504, 2007.
- [157] W. M. Witzel and S. Das Sarma. “Multiple-pulse coherence enhancement of solid state spin qubits”. *Phys. Rev. Lett.*, **98**: 077601, 2007.
- [158] E. Barnes, D. L. Deng, R. E. Throckmorton, Y. L. Wu and S. Das Sarma. “Noise-induced collective quantum state preservation in spin qubit arrays”. *Phys. Rev. B*, **93**: 085420, 2016.
- [159] W. Heisenberg. “Zur Theorie des Ferromagnetismus”. *Z. Phys.*, **49**: 619, 1928.
- [160] H. Bethe. “Zur Theorie der Metalle I. Eigenwerte und Eigenfunktionen Atomkete”. *Z. Phys.*, **71**: 205, 1931.

- [161] M. A. Cazalilla, R. Citro, T. Giamarchi, E. Orignac and M. Rigol. “One dimensional bosons: From condensed matter systems to ultracold gases”. *Rev. Mod. Phys.*, **83**: 1405, 2011.
- [162] T. Lahaye<sup>1</sup>, T. Koch, B. Fröhlich, M. Fattori, J. Metz, A. Griesmaier, S. Giovanazzi and T. Pfau. “Strong dipolar effects in a quantum ferrofluid”. *Nature*, **448**: 672, 2007.
- [163] T. Koch, T. Lahaye, J. Metz, B. Fröhlich, A. Griesmaier and T. Pfau. “Stabilization of a purely dipolar quantum gas against collapse”. *Nat. Phys.*, **4**: 218, 2008.
- [164] I. Bloch, J. Dalibard and W. Zwerger. “Many-body physics with ultracold gases”. *Rev. Mod. Phys.*, **80**: 885, 2008.
- [165] M. Lewenstein, A. Sanpera and V. Ahufinger. *Ultracold Atoms in Optical Lattices: Simulating Many-Body Quantum Systems*. Oxford University Press, Oxford, 2012.
- [166] S. Giorgini, L. P. Pitaevskii and S. Stringari. “Theory of ultracold atomic Fermi gases”. *Rev. Mod. Phys.*, **80**: 1215, 2008.
- [167] M. P. A. Fisher, P. B. Weichman, G. Grinstein and D. S. Fisher. “Boson localization and the superfluid-insulator transition”. *Phys. Rev. B*, **40**: 546, 1989.
- [168] R. Blatt and C. F. Roos. “Quantum simulations with trapped ions”. *Nat. Phys.*, **8**: 277, 2012.
- [169] O. E. Dial, M. D. Shulman, S. P. Harvey, H. Bluhm, V. Umansky and A. Yacoby. “Charge noise spectroscopy using coherent exchange oscillations in a Singlet-Triplet qubit”. *Phys. Rev. Lett.*, **110**: 146804, 2013.
- [170] E. Barnes, L. Cywinski and S. Das Sarma. “Nonperturbative master equation solution of central spin dephasing dynamics”. *Phys. Rev. Lett.*, **109**: 140403, 2012.
- [171] W. M. Witzel, L. Cywinski and S. Das Sarma. “Electron spin dephasing due to hyperfine interactions with a nuclear spin bath”. *Phys. Rev. Lett.*, **102**: 057601, 2009.

- [172] W. M. Witzel, L. Cywinski and S. Das Sarma. “Pure quantum dephasing of a solid-state electron spin qubit in a large nuclear spin bath coupled by long-range hyperfine-mediated interactions”. *Phys. Rev. B*, **79**: 245314, 2009.
- [173] M. Johanning, A. Varon and C. Wunderlich. “Quantum simulations with cold trapped ions”. *J. Phys. B: At. Mol. Opt. Phys.*, **42**: 154009, 2009.
- [174] R. Islam, E. E. Edwards, K. Kim, S. Korenblit, C. Noh, H. Carmichael, G. D. Lin, L. M. Duan, C. C. Joseph Wang, J. K. Freericks and C. Monroe. “Onset of a quantum phase transition with a trapped ion quantum simulator”. *Nat. Commun.*, **2**: 377, 2011.
- [175] K. Kim, S. Korenblit, R. Islam, E. E. Edwards, M. S. Chang, C. Noh, H. Carmichael, G. D. Lin, L. M. Duan, C. C. Joseph Wang, J. K. Freericks and C. Monroe. “Quantum simulation of the transverse Ising model with trapped ions”. *New J. Phys.*, **13**: 105003, 2011.
- [176] D. Porras and J. I. Cirac. “Effective quantum spin systems with trapped ions”. *Phys. Rev. Lett.*, **92**: 207901, 2004.
- [177] C. Schneider, D. Porras and T. Schaetz. “Experimental quantum simulations of many-body physics with trapped ions”. *Rep. Prog. Phys.*, **75**: 024401, 2012.